2015-02-02

Characterizing Turbulence Modification via Red-Blood-Cell Analogs in Free Shear Layers using Particle Tracking Velocimetry

Kaucky, Lucie

UNIVERSITY OF CALGARY

Characterizing Turbulence Modification via Red-Blood-Cell Analogs in Free Shear Layers using Particle Tracking Velocimetry

by

Lucie Kaucky

A THESIS

SUBMITTED TO THE FACULTY OF GRADUATE STUDIES

IN PARTIAL FULFILMENT OF THE REQUIREMENTS FOR THE

DEGREE OF MASTER OF SCIENCE

GRADUATE PROGRAM IN BIOMEDICAL ENGINEERING

CALGARY, ALBERTA

JANUARY, 2015

Abstract

The turbulence modification of red blood cells is evaluated using a basic experimental approximation to blood, which specifically accounts for its particle-laden and dense concentration *in vivo*. The contribution of super absorbent polymer beads to a developing free shear layer is quantified using particle tracking velocimetry. Results showed that the presence of a particle-phase reduced mean velocities, kinetic energy, and the gradient of kinetic energy, implying that the free shear layer was diffused. Furthermore, similar fluid behaviour resulted between the suspension cases when Reynolds number was increased from 1,143 to 10,490. This suggests that red blood cells act to diffuse flow features that can subsequently lead to instabilities from which transitional and eventually turbulent behaviour can develop. These findings indicate that a two-phase model, specifically accounting for the dense particle-phase of blood, may be necessary for arterial blood flow where transition and turbulence can occur.

Acknowledgements

I could also not go without thanking Dr. David Wood, who provided much needed support and direction when most needed, and graciously dedicated his time to me and my work. I have learnt a lot through this degree and the experience I am sure will prove to be invaluable. I am also incredibly grateful to Dr. Andrew Walker for his incessant guidance, patience, help, and passion for this topic throughout. I am incredibly appreciative of all his efforts. Furthermore, I would like to express gratitude to my lab mates for the laughs and support throughout, and in particular, Giuseppe A. Rosi for the long hours he kindly dedicated to my work. Finally, I am incredibly grateful to my family, friends, and especially my mom for her unwavering support, guidance, and encouragement, without which I am certain I could not have completed this project.

Table of Contents

Abstract ii
Acknowledgements iii
Table of Contents iv
List of Tables vi
List of Figures and Illustrations vii
List of Symbols, Abbreviations and Nomenclature xi

CHAPTER ONE: INTRODUCTION 1
1.1 Motivation 1
1.2 Particle-laden Flows and Turbulence 3
1.3 Fluid Viscoelasticity 4
1.4 Blood: A Particle-laden and Viscoelastic Fluid 5
1.5 Turbulence, Diffusion, and Dissipation 8
1.6 Free Shear Layers and Turbulence 10
1.7 Turbulence in the Cardiovascular System 12

CHAPTER TWO: BACKGROUND 17
2.1 Particle-Laden Flow Properties 17
2.2 Turbulence Modification by Suspended Particles 18
2.3 Modes of Turbulence Modification 20
2.4 Exclusions and Assumptions 23

CHAPTER THREE: OBJECTIVE AND HYPOTHESIS 24
3.1 Objective 24
3.2 Effect of Red Blood Cell Presence on Turbulence Modification in Blood 25
3.3 Effect of Increasing Characteristic Length on Turbulence Modification by Red 27

CHAPTER FOUR: METHODOLOGY 29
4.1 Introduction 29
4.2 Experimental Set-Up 31
4.2.1 Free Shear Layer Generation 34
4.2.2 Super Absorbent Polymer Beads as a RBC Analog 36
4.3 Flow Visualization: 2-D PTV 41
4.3.1 PTV System and Data Acquisition 41
4.3.2 Post-processing 43
4.3.3 Data Validation 45

CHAPTER FIVE: RESULTS 47
5.1 Evidence of an Established Free Shear Layer 48
5.1.1 Starting Vortex and Free Shear Layer at Re=10,490 48
5.1.2 Starting Vortex and Free Shear Layer at Re=1,143 50
5.2 Effect of SAP Bead Presence on a Developing Free Shear Layer 51
5.2.1 Velocity Statistics 51
5.2.2 Lagrangian Velocity Plots 52

5.2.3 Kinetic Energy and the Free Shear Layer....54
5.3 Increasing Reynolds Number and Particle Induced Delay of Transitional 59
5.3.1 Vortical Instabilities and Lagrangian Fluid Velocity 60
5.3.2 Kinetic Energy and the Free Shear Layer....61

CHAPTER SIX: DISCUSSION 62
6.1 Viscous Effects 62
6.2 Reduced Velocities 64
6.3 Diffusion of Flow Features and Energy Storage 65
6.4 Implications of Findings to Arterial Blood Flow....66
6.4.1 Delayed Transitional Behaviour by Red Blood Cells in the Vasculature 67
6.4.2 Delayed Transitional Behaviour by Red Blood Cells with Increasing....68
6.5 Limitations and Error....69
6.5.1 RBCs and SAP Beads....69
6.5.2 Vascular Flow Environment....71
6.5.3 Experimental Set-Up Limitations....72
6.5.4 Flow Conditions 73
6.5.5 Error due to 3-D Motion and Laser Refraction 74
6.6 Summary....75

CHAPTER SEVEN: CONCLUSIONS AND RECOMMENDATIONS....77
7.1 Conclusions....77
7.2 Recommendations....79

REFERENCES 81

APPENDIX A: PARTICLE TRACKING INCONSISTENCIES AND 3-D MOTION ...89
A.1. 3-D Out-of-Plane Motion Without Beads....89
A.2. Laser Refraction with SAP Beads....91

APPENDIX B: VELOCITY DATA DISTRIBUTION....95

APPENDIX C: EFFECTIVE VISCOSITY CALCULATIONS 98

List of Tables

Table 1.1: Comparison of select mammal's average hematocrit and mean cell volume (MCV) (Windberger et al., 2003) 2

Table 4.1: 3-by-2 test matrix displaying control and test cases for both turbulent and laminar Reynolds numbers (Re_H) of 1,143 and 10,490, respectively. 31

Table 4.2: Select physical properties of the suspending fluids at a temperature of 22°C (Segur & Oberstar, 1951). 33

Table 4.3: Minimum track length (Min TL) constraints set for post-processing and the resultant number of particles tracked 46

Table 5.1: Velocity statistics of tracked particle data over the FOV obtained from pre-processing in DaVis 8.1.3. These values were obtained using data from all runs performed. 52

List of Figures and Illustrations

Figure 1.1: CT image of a front view of the common illiac arteries (a) and transected views (b) of the right and left branches at the location denoted in a. Plaque build-up (dark arrows) is visible in both the left and right artery branches along with a lesion in the right branch (small white arrow). The specimen is not imaged *in vivo*. Adapted from Medynsky *et al.* (1998). 8

Figure 1.2: A summary of turbulent kinetic energy (TKE) ranges, where production occurs at the largest length scales, of turbulence and dissipation at the smallest, named the Kolmogorov scale. Turbulent energy dissipation occurs only at these small scales, and energy injected must balance the energy dissipated in order to maintain turbulence. In the inertial sub-range, the cascade of turbulent kinetic energy from large to small scales is seen. 10

Figure 1.3: Shear layer separation (A) from a sharp-edged bluff body resulting in a free shear layer and subsequent rollup up into a vortex. The velocity gradient of the free shear layer, as a result of the recirculating flow and the freestream above, is shown. A shear layer is also shown at the solid-fluid interface (B) preceding flow over a perturbation, where a free shear layer forms due to the opposing velocities in the freestream and the recirculating flow behind the obstruction. A free shear layer velocity gradient (C) as a result of two flows, travelling in the same direction, with varied velocities is depicted above. Modified from Kheradvar & Pedrizzetti (2012). 12

Figure 1.4: Vortex formation at the carotid bifurcation of a healthy individual, demonstrating the presence of free shear layers and vortices in the arterial flow environment. These are instabilities that can be a starting point for transitional and therefore turbulent flow. Adapted from Kheradvar & Pedrizzetti (2012)..... 15

Figure 4.1: Representation of the physiological significance of the experimental set-up, where the glass aquarium is representative of an enlarged section of blood (A) flowing within an artery that is subject to the effects of a free shear layer (location denoted by B) as a result of an upstream perturbation. Areas of the arterial vasculature that are prone to atherosclerotic plaque development (C) are highlighted, as seen on the inner wall of the aortic arch (Adapted from Chiu & Chien, 2011). 30

Figure 4.2: Experimental test set-up with dimensions (in red) demonstrating relative positions of equipment for PTV data acquisition and flow directionality (blue). 32

Figure 4.3: Experimental set-up of motor traverse (A), SA 4 camera (B), tank (C), laser (D), camera and tank supports (E). 34

Figure 4.4: FOV location and relative dimensions based on a plate height of 10 cm (H)..... 35

Figure 4.5: Super absorbent polymer beads (SAP) beads upon complete saturation. Here an uncompressed (A) bead relative to a compressed (B) bead is shown, demonstrating the deformability of the SAP beads (B). 36

Figure 4.6: SAP Beads suspended in the Glyc60, where good optical matching can be seen in the upper 3/4 of the tank, but poor matching is evident in the bottom 1/4. 38

Figure 4.7: Images of the target used later for calibration of pixel size to physical length during data processing. The target is placed at the laser plane location, where measurement of the fluid is performed – 0.75H from the front aquarium wall. Shown are test cases of water (A), Glyc30 (B), Glyc60 (C), water with 50% beads (D), Glyc30 with 50% beads (E), and Glyc60 with 50% beads (F). In cases where no beads are present (top row) thorough mixing of the solutions is confirmed by these images from a lack of distortion of the grid points. In cases with beads (bottom row) optical matching between the beads and suspending fluid is demonstrated, also by a lack of distortion of the grid points. 40

Figure 5.1: Raw images of frames 131 to 138 (of 150 total) superimposed from a single run, where plate motion is from left to right. Shown are Reynolds numbers (Re)=1,143, 4,581, and 10,490 for cases *without* beads (top row) and *with* beads (bottom row). The green arrow identifies the free shear layer shortly after being generated at the plate tip, and the blue arrow identifies where the free shear layer and the outer rings of the starting vortex appear to interact. The red arrow shows the location where at Re=10,490 and 4,581, small vortices within the free shear layer are exiting the FOV and the respective location is also shown at Re=1,143, although these instabilities were less apparent; see Video 5.1. The yellow arrow denotes a speculated vortex core in the data *with* beads that is most apparent in the Re=10,490 image. 49

Figure 5.2: Tracked particle pathlines plotted together in a single plot for each case using data obtained from all runs (20 for cases without beads and 100 runs for cases with beads). Each plot is a collection of the pathlines throughout the entire length of the plate tow. Colouring denotes a particle's velocity at each tracked location creating a respective pathline. Cases are shown at Reynolds numbers of 1,143, 4,581, and 10,490 using Glyc60, Glyc30, and water as suspending fluids, respectively. Both cases *without* beads (top row) and *with* beads (bottom row) are presented. The plotted tracks were constrained with minimum track lengths stipulated by Table 4.3. Velocity and dimensions are normalized by the freestream velocity (U_o) and plate height (H), respectively. Plate tow direction is from left to right and the plate tip is at y/H=0 and extends down to the x-axis. 53

Figure 5.3: Kinetic energy (KE) ratio of each particle's energy as a fraction of the freestream. Dashed line indicates the location of the identified free shear layer in (A). Shown is t*=0.93 (frame 116/150), where KE was calculated using velocity data with minimum track length (min TL) constraints outlined in Table 4.3. The location of the plate is shown at the selected t*. Reynolds numbers of 1,143, 4,581, and 10,490 are presented for both "non-beaded" (top row) and "beaded" (bottom row) cases. All lengths are normalized by plate height (H). 56

Figure 5.4: The Re=1,143 case *without* beads is expanded (left) from Figure 5.3 to show the prevailing gradients in kinetic energy (KE). The (**black**) arrows shows the elevated KE region at the free shear layer, the blue arrow denotes the KE gradient from a central region of the vortex to its edge, and the green arrow denotes the gradient from the free shear layer to the quiescent fluid above. Superimposed images are shown (right) at Re=1,143 from Figure 5.1, showing the expected velocity gradient shape between the quiescent fluid above and the starting vortex below the free shear layer. Images near the end of the tow were selected as there is less shadowing from the plate and more of the vortex is visible in the FOV..... 58

Figure 5.5: Kinetic energy (KE) of tracked particles for cases *with* beads, non-dimensionalized by freestream KE, where only particles with a KE *below* 0.75 are shown. Data is shown for Re=1,143, 4,581, and 10,490 at both t*=0.46 (top row) and t*=0.93 (bottom row). These time points were arbitrarily chosen to demonstrate fluid behaviour both part way through and near the completion of the tow. The plate extends from the bottom of the FOV until y/H=0, but is not shown in its entirety. 59

Figure A.1: The number of particles tracked per frame plotted throughout the plate tow in Glyc60, Glyc30, and water *without* beads (top row) representing Reynolds numbers (Re) of 1,143, 4,581, and 10,490, respectively. The same is shown for cases *with* the addition of beads (bottom row). Results presented are using all data collected and constrained with minimum track lengths (min TL) as per Table 4.3. 90

Figure A.2: Density distribution of the total amount of particles tracked over the total length of the plate tow, for all the runs combined (no beads=20; with beads=100) and plotted over the FOV. Blue indicates lower densities and Red indicates the highest. No minimum track length constraint was applied. The approximate location of the plate and tow direction are shown for reference, noting that this plot shows results from the entire recording time, thus from all frames, and not just at the time-point where the plate is shown. 91

Figure A.3: PTV laser (top view) propagating and refracting through the length of the aquarium, filled with 30% by weight aqueous glycerol and containing suspended, near-neutrally buoyant, SAP beads. The approximate location of the measurement location where the camera was focused on the laser plane is denoted by the yellow box..... 92

Figure A.4: Raw images (frame 116/150) for the cases *with* beads. The green arrows denote the locations of higher intensity "streaks" that are most obvious at Re=4,581 and apparent at Re=1,143, where both suspending fluids are solutions of glycerol. Note that this effect is not as prominent at Re=10,490 where the suspending fluid was water. Plate tow direction is from left to right. 94

Figure A.5: Distribution of U and V-component velocities, and total velocity (U_t) for the cases *without* beads using all the data obtained from all 20 runs at each Reynolds number. Of importance is the U and V-component velocities tend to non-normal distributions, whereas U_t are closer in comparison to being normally distributed. 96

Figure A.6: Distribution of U and V-component velocities, and total velocity (U_t) for the cases *with* beads using all the data obtained from all 100 runs at each Reynolds number. Of importance is that V velocities appear to be generally normally distributed, whereas the U and V-component velocities are generally skewed. 97

List of Symbols, Abbreviations and Nomenclature

Symbol	Definition
Ø	Diameter
Φ	Volumetric Concentration
Φ_m	Maximum Volumetric Concentration
TKE	Turbulent Kinetic Energy
SAP	Super Absorbent Polymer
Re	Reynolds Number
Re_p	Particle Reynolds Number
Re_H	Reynolds Number based on Perturbation Height
Re_c	Critical Reynolds Number to Transition
Re_K	Reynolds Number based on Effective Viscosity by Krieger's Formula
d_p	Particle Diameter
U_t	Total Velocity Magnitude
U_o	Freestream Velocity
t^*	Non-Dimensionalized Time
Stk	Stokes Number
Pa_{Re}	Particle Momentum Number
MCV	Mean Cell Volume
RBC	Red Blood Cell
WSS	Wall Shear Stress
RI	Refractive Index
EC	Endothelial Cell
μ	Kinematic Viscosity (Pa s)
ρ	Density (kg/m^3)
ν	Velocity
H	Plate Height/Perturbation Height
Glyc30	30% by weight Aqueous Glycerol
Glyc60	60% by weight Aqueous Glycerol

Chapter One: **INTRODUCTION**

In this chapter the motivation for and an introduction to the topics associated with this study are presented. The topics are organized into six sections as follows: motivation, particle-laden flows and turbulence, fluid viscoelasticity, blood: a particle-laden and viscoelastic fluid, turbulence, diffusion and dissipation, free shear layers and turbulence, and turbulence in the cardiovascular system.

1.1 Motivation

There are innumerable puzzling aspects of blood yet to be explored. Blood is in charge of nutrient storage and transport, waste removal, and maintaining homeostasis of fluid, electrolyte, and gases, among many other roles. Gas transport, specifically O_2 and CO_2, is made possible by the presence of red blood cells (RBC). RBC hematocrit (RBC volume fraction), shape, homogeneity, mean cell volume[1] (MCV), presence of a nucleus, and average lifespan varies amongst species. However, given the variation in organism mass and thus size of the respective vascular systems, RBC variations in MCV are relatively insignificant, as shown in Table 1.1. A horse, for example, has a MCV almost identical to that of a mouse. There does not appear to be a relationship between MCV of RBCs and the animal's relative size (Windberger et al., 2003). RBCs are the predominant particulates, that together with plasma, consitute blood. Consequently, blood flow dynamics are complicated due to cell-cell and cell-fluid interactions. RBC motion and behaviour, such as cell agglomeration and stacking, is influenced by the fluid dyamics, and vice versa (Han et al., 2001; Ku, 1997).

[1] Mean cell volume is used as a measure of erythrocyte size because it can be compared independently of differences in shape to which dimensional properties, such as diameter, are sensitive to.

Table 1.1: Comparison of select mammal's average hematocrit and mean cell volume (MCV) (Windberger et al., 2003)

Organism	MCV (fl)	Hematocrit
Horse	45	35
Human	80-96	45
Mouse	46	40

Hemodynamics, or the dynamics of flowing blood, affect the health and disease of the vasculature. The blood flow environment provides feedback on local conditions within the cardiovascular system itself and also to the body through the endothelial cells (EC) (Evans & Kwak, 2013). As an example, atherosclerosis progression and development is affected by EC response to wall shear stress (WSS), a result of local flow conditions (Chiu & Chien, 2011; Mejia et al., 2011). Furthering our understanding of flow conditions within the vasculature gives insight to the physiology of the cardiovascular system. Understanding the natural flow environment in the heart and vasculature is relevant to the design, development, and improvement of implantable biomedical devices that can alter hemodynamics, such as heart valves, stents, catheters, and artifical hearts. Improving cardiovascular models of the pathological arterial environment is equally important, so as to gain insight on conditions such as atherosclerosis, found typically where flow is altered or diverted (Ku, 1997). Greater turbulent kinetic energy (TKE) tends to accompany constrictions, stenosis, and other pathologies in the vasculature as a result of induced flow perturbations (Stein & Sabbah, 1976). Turbulence is related to shear strain rate and forces within the fluid that play an important role in atherosclerotic plaque build-up and cardiovascular disease development and progression (Boon, 2009; Gülan et al., 2012).

1.2 Particle-laden Flows and Turbulence

Two-phase flows have been often studied in the context of industrial, non-biological fluids. Particle-laden flows outside the biofluid realm have shown that the presence of the particles can both reduce turbulent drag and increase TKE (Sreenivasan & White, 2000; Roy et al., 2006; White & Mungal, 2008; Samanta et al., 2013). In brief, particles in flow act to modify turbulence, either by augmentation or attenuation, depending on the individual and combined properties of the particles and fluid (Tanaka & Eaton, 2008). Dense suspensions, defined as particle volumetric concentrations greater than 0.01%, bear further complexity because of four-way coupling; the presence of fluid-particle, particle-fluid, and two-way particle-particle interactions (Elgobashi, 1994). Particles modifying turbulence intensity is a multidimensional effect, dependent on the combined properties of the fluid and particle. Thus, outcomes of this phenomenon are difficult to generalize (Crowe, 2000; Tanaka & Eaton, 2008).

In flows with added polymers, the onset of turbulence occurs at lower Reynolds number than expected in a flow devoid of particles (Samanta *et al.*, 2013). Reynolds number, a dimensionless parameter relating viscous and inertial effects, is defined by Equation 1.1 as,

$$\mathrm{Re}_H = \frac{\rho \upsilon H}{\mu} \tag{1.1}$$

using fluid density (ρ), dynamic viscosity (μ), and velocity (v) and a characteristics length (H). For this project, Re_H will be defined by a characteristic length equal to the height of the perturbation to flow. Further examples of modified turbulence by particles include drag reduction and reduced vortex formation (Suzuki et al., 2000; Lieu & Jovanovic, 2013). Dubief et al. (1994) attribute the modified turbulent dynamics to the combined effects of polymer behaviour and flow structures. Turbulence modification in polymeric flows is at least partly due to the viscous and elastic

properties of the particles (Samanta et al., 2013). Blood analogs are used in cardiovascular modelling due to their similitude in fluid characteristics and flow behaviour to blood. Furthermore, use of a blood analog avoids many health, ethical, and sourcing issues, and avoids the need for stringent conditions to maintain blood's integrity outside the body (e.g. temperature, anti-coagulants). In contrast to a single-phase analog, a two-phase polymeric blood analog displays prolonged laminar behaviour, speculated to be due to the presence of suspended polymers acting analogous to that of RBCs in plasma (Li et al., 2014).

In all cases, the development, progression, and expression of turbulence are impacted when some form of particles are suspended within a fluid. Additionally, the resultant fluid behaviour is clearly a result of many factors between both the particle and carrier-phases. Given the multi-faceted nature of turbulence modification, accounting for more of these factors together has led to increased success in predicting such fluid behaviour. Tanaka & Eaton (2008) incorporated viscous forces of the fluid on the particle, particle size, inertia, and Stokes numbers (Stk) into their mathematical definition of turbulence modification known as the particle momentum number (Pa_{Re}). However, the mechanisms by which modification occurs are still poorly understood, especially small-scale fluid-particle interactions directly near the particle surface, where TKE reductions seem to be most substantial (Burton & Tanaka, 2005)**.** Furthermore, whether or not RBCs in fact do modify turbulence in blood has yet to be affirmed.

1.3 Fluid Viscoelasticity

The viscoelasticity of a fluid as a result of suspended particles is a point of deliberation in the context of turbulence modification in particle-laden flows (Snabre & Mills, 1999; White & Mungal, 2008; Samanta et al., 2013). The viscoelasticity of a fluid depends on both its viscous and

elastic responses. Elasticity is a characteristic of solid materials demarcated by a linear stress-strain relationship and an ability to store and later release energy, whereas a viscous fluid dissipates energy (Kumaran et al., 2010). A viscoelastic fluid responds with a combination of these characteristics, in that it can both absorb and dissipate energy (Irgens, 2008). By definition, the stresses within a viscoelastic fluid are only partly due to strain and therefore do not display a linear stress-strain relationship (Kumaran et al., 2010). Biofluids are often viscoelastic and such fluids do not necessarily share flow dynamics and turbulence development with homogenous, particle-laden or even other non-Newtonian fluids. By theory, a non-Newtonian and viscoelastic fluid both do not display a linear stress-strain relationship and thus a constant viscosity. However, a non-Newtonian fluid is not necessarily viscoelastic.

1.4 Blood: A Particle-laden and Viscoelastic Fluid

Blood presents with two-phase viscoelastic behaviour due to the presence of suspended RBCs and their deformability (Secomb et al., 2007; Fedosov et al., 2010; Campo-Deaño et al., 2013). At high shear strain rates, blood viscosity approaches approximately 3.5×10^{-3} Pa·s, exemplifying its shear-thinning and thus non-Newtonian behaviour (Katrisis, 2007; Mejia, 2011). A fluid with suspended particles can behave viscoelastically, where its flow dynamics and properties can change in response to a shear strain rate and particle volumetric concentration and size (Tanaka & Eaton, 2008; Gao & Hu, 2009). It has been suggested that the abilty of RBCs to deform in response to flow conditions is responsible for the prolonged laminar flow behaviour measured in blood (Han et al. 2001). Prolonged laminar flow, also described as delayed transition to turbulence, is not typical of homogenous flows. This is similar to the prolonged laminar flow behaviour, or turbulence modification, observed in blood analogs noted earlier.

Red blood cells have been studied primarily as individual cells (Sugii et al., 2005; Mansour et al., 2010; Grover et al., 2011; Angelini et al., 2013; Cordasco and Bagchi, 2013). RBCs have been observed to align in the direction of shear and travel in a variety of forms including rolling, tank treading, and kayaking motions (Cordasco and Bagchi, 2013). Tank treading is a crawling motion that is made possible through the cell's deformation while kayaking is a revolution of the cell in the shape of a figure eight. Shape and membrane properties of RBCs are well documented, as well as the independent motion, deformation, and orientation of single RBCs in response to their flow environment, the shearing rate, fluid viscosity, and flow rate (Cordasco and Bagchi, 2013). However, little is known on the behaviour and resultant dynamics of RBCs acting together as an agglomeration of cells in plasma. Modelling the migration of RBCs has been investigated primarily through analytical and numerical models; however, use of these approaches beyond the dynamics of a single-cell is considerably more challenging (Secomb et al., 2007; Fedosov et al., 2010; Mansour et al., 2010). The numerical modelling of blood, a suspension consisting of millions of colliding particles, is computationally expensive in vessels of the microvasculature, let alone extending such modelling to the largest arteries that are several orders of magnitude larger in diameter (Cristini & Kassab, 2005).

In the microvasculature, or vessels smaller than 1000 μm in diameter, a non-homogenous fluid assumption is typically employed for several reasons (Cristini & Kassab, 2005). The Fåhræus-Lindqvist (F-L) effect, a phenomenon limited to the microvasculature, occurs where bulk blood viscosity is found to be dependent on vessel diameter due to the cell-free layer near the wall of small vessels (Fåhraeus, 1958; Pries et al., 1986). This layer does not grow in proportion to vessel diameter, such that the cell-free layer constitutes a greater proportion of the diameter in smaller vessels of the vasculature, thus affecting viscosity (Baskurt & Meiselman, 2008). This creates a

significant two-phase boundary in the flow through vessels of the microvasculature. Therefore, the two-phase, non-homogenous nature of blood is typically accounted for when modelling such flows (Fedosov et al, 2010). The rouleaux effect is another two-phase flow configuration prominent in the microvasculature, where RBCs aggregate into clusters of stacked cells, typically under pathophysiological conditions (Ku, 1997). The rouleaux effect can occur during flow through the narrowest vessels at very low shear strain rates, flows associated with Reynolds number as low as 10, and in the presence of high plasma protein concentrations (Han et al., 2001; Baskurt & Meiselman, 2008). Additionally, in capillary flow, RBC diameter is near that of the vessel creating a distinct two-phase flow, so that individual cell deformation, orientation, or migration have a significant impact on the fluid (Secomb et al., 2007). Aggregation and distribution of RBCs affects the rheology of blood. Shear strain rate determines the extent and pattern of cell aggregation through its influence on cell shape, orientation, and deformation.

As discussed above, the existence of rouleaux and F-L effects in small vessels precludes the use of a single-phase flow assumption in the microvasculature for the sake of accurate predictions. However, in large arteries with diameters greater than 1000 μm, homogenous flow is typically assumed. If turbulence is to occur in the vasculature, it would be confined to larger vessels, where the use of single-phase, homogeneous fluid may not be a valid assumption given the particle-induced turbulence modification phenomena observed in particle-laden flows (Tanaka & Eaton, 2008; Steinman, 2012). The presence of turbulence and its intensity depend on the flow environment and thus vary through the heart's valves, downstream of a stenosis, or within a healthy vessel, for example. Figure 1.1 exemplifies that an artery is not a smooth and perfectly circular vessel, but rather one that bears non-uniformities including plaque along the endothelial wall that reduces vessel diameter and can be a perturbation to the flow. Finally, to model blood under a

single-phase Newtonian assumption a viscosity is required. The viscosity of blood has been observed to stabilize near 3.5 x 10^{-3} Pa·s with increased shear strain rates (Steinman, 2012). Rising Reynolds number involves higher shear strain rates and flow develops towards turbulence (Mejia et al., 2007). However, the viscosity of blood in turbulent flow is undescribed in the literature.

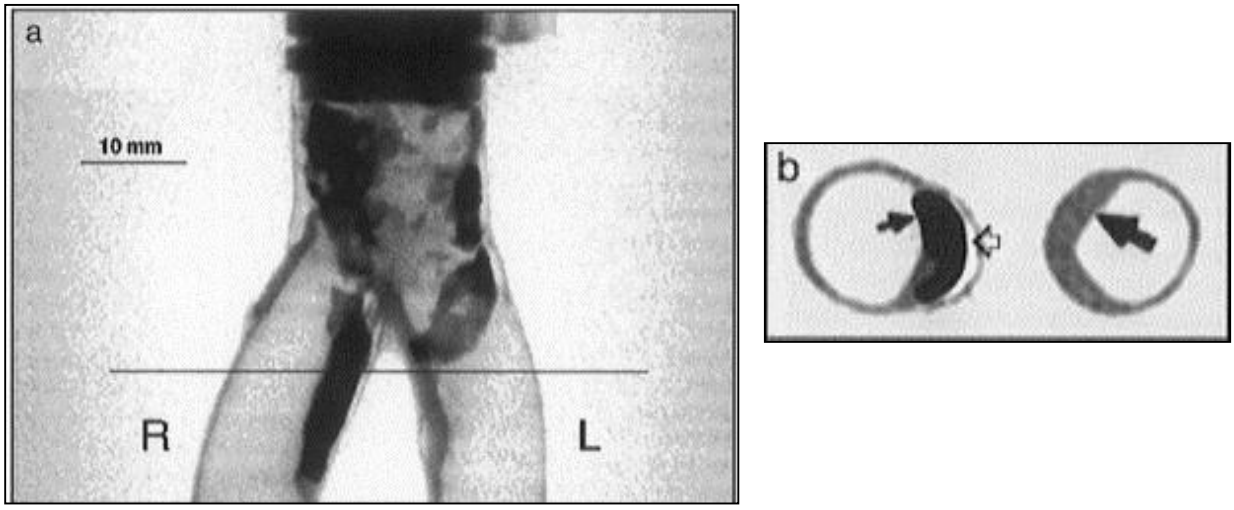

Figure 1.1: CT image of a front view of the common illiac arteries (a) and transected views (b) of the right and left branches at the location denoted in a. Plaque build-up (dark arrows) is visible in both the left and right artery branches along with a lesion in the right branch (small white arrow). The specimen is not imaged *in vivo*. Adapted from Medynsky *et al.* (1998).

1.5 Turbulence, Diffusion, and Dissipation

Turbulence, as described by Roberts et al. (2002), is characterized by stochastic fluid motion essentially involving three-dimensional interaction of the fluctuating vorticity, in contrast to laminar flow with parallel flowing fluid elements. Turbulent kinetic energy is produced at low frequencies, moves through the inertial subrange at intermediate frequencies, and dissipates at high frequencies. The small-scale structures, or high frequency motions of the fluid, become smaller and dissipate faster with increasing Reynolds number (Durbin and Pattersson-Reif, 2010). First, turbulence formation or turbulent energy injection typically occurs at large length scales. The

inertial energy range is the transfer of energy from large to smaller length scales of fluid motion, also referred to as the energy cascade. Finally, turbulent energy dissipation occurs at the smallest length scales of turbulent motion, the Kolmogorov scale, as this is where viscous forces become dominant, promoting energy conversion to heat (dissipation) (Durbin and Pattersson-Reif, 2010). Dissipation occurs at the smallest length scales where the instantaneous velocity gradients are highest, since the same velocity difference occurs over a shorter space (Roberts et al., 2002). However, this requires fully developed turbulence and in order to maintain turbulence, the energy production at large scales must balance the energy dissipation at small scales. As a result, any mechanism that removes kinetic energy (KE) from the fluid system in a turbulent regime and affects energy injection, can affect turbulent fluid motion. Figure 1.2 summarizes the turbulent kinetic energy (TKE) ranges and the respective length scales at which they occur. In laminar or transitional flow, removing kinetic energy from the fluid system can delay the onset of turbulence entirely.

Areas of elevated mean kinetic energy are more likely to present with turbulent fluid behaviour. Reducing the local magnitude of KE by either diffusion or dispersion, can act to locally attenuate or delay turbulent behaviour. The transport or spatial variation of turbulence has an effect on both kinetic energy at large-scales and TKE at small-scales (Roberts et al., 2002).

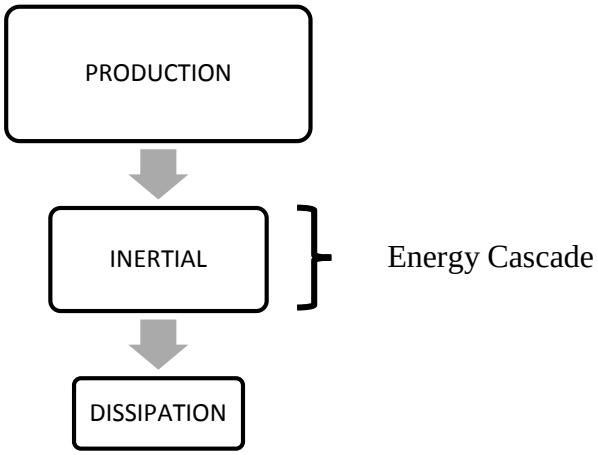

Figure 1.2: A summary of turbulent kinetic energy (TKE) ranges, where production occurs at the largest length scales, of turbulence and dissipation at the smallest, named the Kolmogorov scale. Turbulent energy dissipation occurs only at these small scales, and energy injected must balance the energy dissipated in order to maintain turbulence. In the inertial sub-range, the cascade of turbulent kinetic energy from large to small scales is seen.

1.6 Free Shear Layers and Turbulence

A shear layer is an area of substantial velocity gradient. Shear layers can form at solid-fluid boundary interfaces, such as blood flow at a vessel wall (Kheradvar & Pedrizzetti, 2012). The relative velocity of the mean flow and the fluid at the solid boundary create the velocity gradient, and thus a shear layer. A shear layer can also form at the boundary of two fluid regions of different velocity. For example, the velocity in the wake of an obstruction to the flow relative to the freestream flow creates a free shear layer; see Figure 1.3 (Kheradvar & Pedrizzetti, 2012). A free shear layer is not bound by physical boundaries where transitional flow eventually develops (Durbin and Pattersson-Reif, 2010). A starting flow over a body, such as an airfoil or plate normal to the flow, can generate a starting vortex as described by Lian & Huang (1989). Furthermore, a starting vortex is produced at the point of shearing in a flow, as shown in Figure 1.3, and has an initial growth stage and then is eventually shed from the body. A vortex is a flow feature that can

subsequently lead to instabilities from which transitional and turbulent flow can develop. A starting vortex is initially laminar, but it creates a shear layer with the freestream that is often destabilized, separating into smaller sized vortices and that can eventually lead to turbulent flow (Lian & Huang, 1989). Three regions develop in the free shear layer: an initial region of shearing beginning at the plate tip, followed by a region where small-sized (relative to the starting vortex) equidistant instabilities or vortices form, and finally a region where the small vortices become more disordered as they begin to interact with one another (Lian & Huang, 1989). Therefore, as the vortical instabilities travel in the free shear layer, along the edge of the vortex, they become increasingly more destabilized (Lian & Huang, 1989). Turbulence can begin by the destabilization of such a vortex when these smaller vortices, or successive instabilities, continue to break off in locations of high shear strain rate (Chapman & Tobak, 1985; Kheradvar & Pedrizzetti, 2012). Therefore, a free shear layer is an initial instability, whereby the area is then prone to further destabilization, possibly leading to the development of turbulent flow behaviour (Durbin and Pattersson-Reif, 2010).

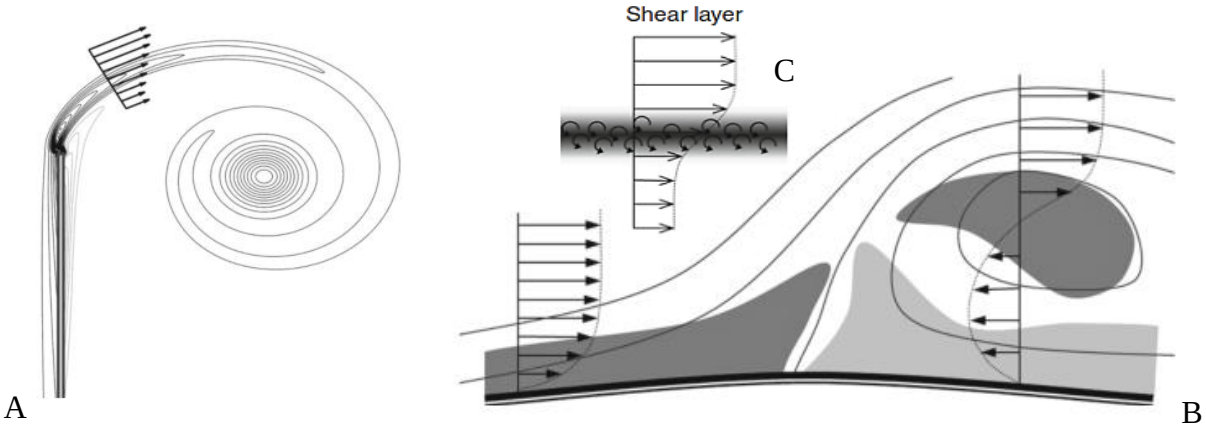

Figure 1.3: Shear layer separation (A) from a sharp-edged bluff body resulting in a free shear layer and subsequent rollup up into a vortex. The velocity gradient of the free shear layer, as a result of the recirculating flow and the freestream above, is shown. A shear layer is also shown at the solid-fluid interface (B) preceding flow over a perturbation, where a free shear layer forms due to the opposing velocities in the freestream and the recirculating flow behind the obstruction. A free shear layer velocity gradient (C) as a result of two flows, travelling in the same direction, with varied velocities is depicted above. Modified from Kheradvar & Pedrizzetti (2012).

1.7 Turbulence in the Cardiovascular System

Localized instabilities, recirculation, and turbulence development can present throughout the human vasculature under healthy and pathological conditions (Stein & Sabbah, 1976; Nerem & Seed, 1972; Ku, 1997; Gülan et al., 2012; Evans & Kwak, 2013). Even in laminar flow, with a Reynolds number as low as 300, turbulence can occur downstream of a stenosis pending the severity of the obstruction (Ku, 1997). Flow destabilization in the vasculature can be identified by vortex shedding at elevated or fluctuating frequencies, or velocity fluctuations at frequencies higher than the heart rate (Peolma & Ooms, 2006; Steinman, 2012). Eddies, where fluid motion opposes that of the overall flow, are characteristic of transitional and turbulent flow and important to maintaining physiological conditions in certain locations of the vasculature. In the heart, vortices and turbulence induce a momentum flux in blood as it passes through the valves and into the chambers. As a result of this transitional and turbulent behaviour in the heart, flow stagnation is

reduced, valve closure is enhanced, and consequently the risk of regurgitation is lessened (Kim et al., 2011; Kheradvar & Pedrizetti, 2012).

However, turbulence is generally not desireable, as it can have severe consequences on cardiovascular health. Artificial, repaired, and diseased heart valves can distort blood flow. Altered flow patterns between the chambers of the heart modify pressure gradients and in so doing reduce flow efficiency (Falahatpisheh & Kheradvar, 2012). Turbulent flow results in energy losses for which the heart must compensate. If the demand on the heart increases, it can eventually lead to heart failure (Kim et al., 2007). Hemolysis (blood cell destruction) can result from turbulence and is a major concern with malfunctioning, diseased, and mechanical heart valves (Antiga & Steinman, 2009). Turbulence and high shear strain rates associated with such valves are the result of leaflet design and the speed at which the valve closes (Herbertson et al, 2011; Li et al., 2011). Elevated turbulence in the vasculature, through changes in pressure and shear strain rate to the vessel walls, can alter EC expression and function, promoting atherosclerotic development as a result (Davies et al., 1986; Barbee, 2002; Chiu & Chien, 2011). Lower and oscillating WSS promotes plaque development and is present in the carotid bifurcation due to the vortices and instabilities induced by the geometry of the area (Kheradvar & Pedrizzetti, 2012).

If present, turbulence would be most prominent in larger arteries and the heart, mainly during fluid deceleration following peak systole; the pumping phase of the cardiac cycle (Kheradvar & Pedrizzetti, 2012). The prevalence of diseased conditions in the heart and larger arteries, such as plaque and calcification of heart valves, is possibly due to the numerous perturbations to flow present in these regions, and their tendancy to generate free shear layers and increase Reynolds number (Kheradvar & Pedrizetti, 2012). An obstruction to flow, such a stenosis,

a heart valve leaflet, or perturbation along a vessel wall will cause blood flow to separate and generate a free shear layer with a high enough Reynolds number.

A vortex itself is not necessarily indicative of, but can give rise to eventual turbulence. At the carotid bifurcation of a healthy individual, a recirculation region which contains at least one vortex, develops through systole in the carotid bulb as shown in Figure 1.4 (Gülan et al., 2012). As noted by Kheradver & Pedrizzetti (2010) and shown in Figure 1.4, the vortex at the carotid bulb forms the boundary of a jet in the main flow and induces separation on the opposite inner carotid branch wall, and therefore, another free shear layer. The shear layers in these recirculation regions are vulnerable to destabilization through a cascade of the initial vortices to numerous smaller ones. The destabilization occurs during the deceleration phase of flow after peak systole (Gülan et al., 2012). Additionally, a free shear layer can entrain fluid, thickening as it travels downstream of the initial generator and resultantly increases the amount of turbulent fluid (Durbin and Pattersson-Reif, 2010). Mitigating this cascade can impede or reduce the initiation of turbulent behaviour at the carotid bifurcation shown above and where similar conditions exist, such as other bifurcations, arches, perturbations along the vessel walls, or stenosis. For example, Gülan et al. (2012) demonstrated through the use of an aortic flow phantom that bi-directional and therefore recirculating flow is present in the aorta, specifically during the diastolic (relaxation) phase of the cardiac cycle. The presence of turbulence is thus dependent not only on the geometry of the vessel, but also on the phase of the cardiac cycle, given the general reduced flow stability throughout the artertial vasculature after peak systole (Kheradver & Pedrizzetti, 2010; Gülan et al., 2012).

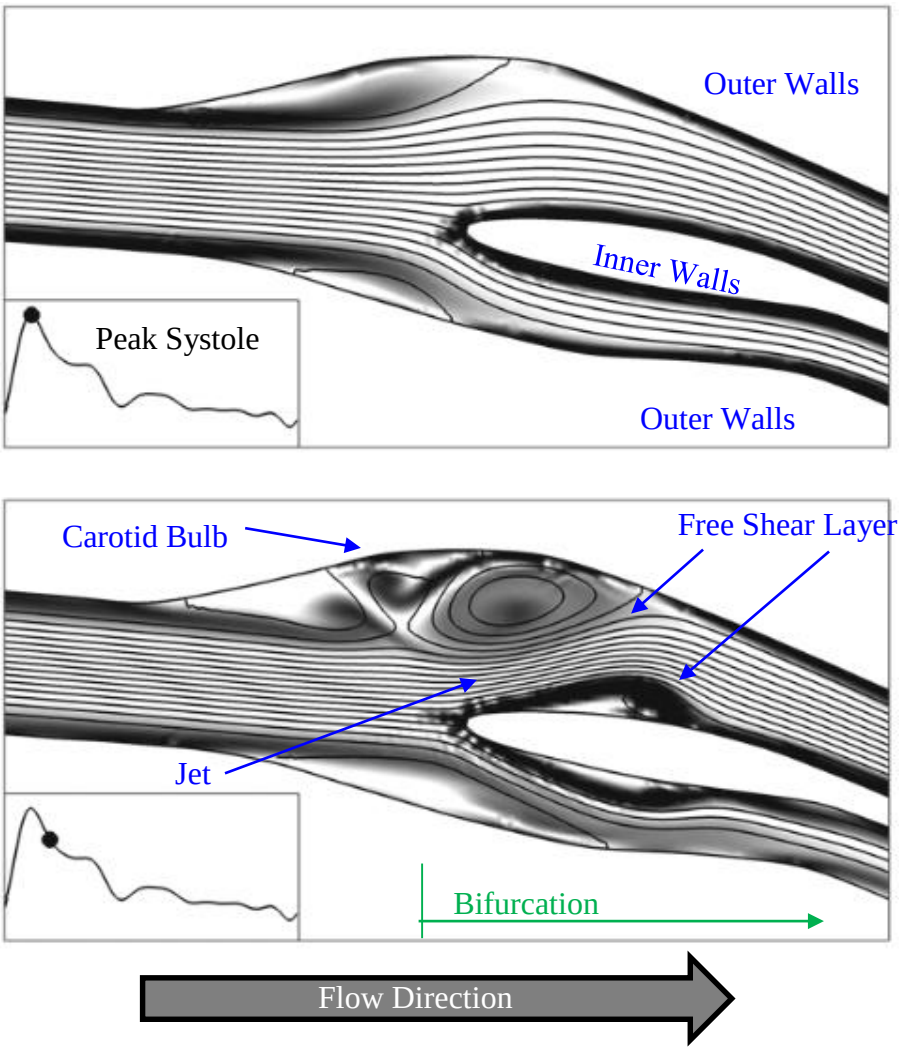

Figure 1.4: Vortex formation at the carotid bifurcation of a healthy individual, demonstrating the presence of free shear layers and vortices in the arterial flow environment. These are instabilities that can be a starting point for transitional and therefore turbulent flow. Adapted from Kheradvar & Pedrizzetti (2012).

Accurate prediction of turbulence development is imperative to models of healthy heart and arterial systems, but especially for conditions imposed by disease or implantable devices. Since prolonged laminar flow behaviour in blood is thought to be due at least in part to the properties of RBCs, the multi-phase characteristic of blood should not be ignored and RBCs should be accounted for in models (Fedosov et al., 2013; Han et al., 2001). Specifically, the packing and proximity of the RBCs as well as their length scale relative to that of turbulent eddies is believed

to affect turbulent flow dynamics (Antiga & Steinman, 2009; Steinman, 2012). No literature to-date has attempted to determine basic knowledge of whether the physical presence of RBCs suspended in plasma causes turbulence modification.

The particle-laden characteristic of blood would suggest that a two-phase model should be utilized when modelling arterial hemodynamics. However, multiphase flow is difficult to model as it is defined by many variables including particle volumetric concentration, size, shape and the physical and mechanical properties of both the particles and suspending fluid (Elgobashi, 1994; Crowe, 2000). It is agreed upon that a two-phase fluid assumption is required in the numerical and experimental modelling of vessels smaller than 1,000 μm (Nag & Jana, 1981; Srivastava & Saxena, 1995; Srivasta & Srivastava, 2009). As previously noted, computational modelling of blood flow in large diameter arteries, with billions of deformable suspended particles colliding, is incredibly multifaceted (Cristini & Kassab, 2005). The development of turbulence only heightens the complexity of this problem and serves to highlight the use of physical experiments in order to explore the bulk effects of RBC presence on turbulence modification in a particle-laden flow.

Chapter Two: **BACKGROUND**

To date, no studies have applied knowledge of turbulence modification in particle-laden flows to blood flow. There has been speculation in the biomedical world that RBCs are the reason for blood's non-Newtonian rheology, where turbulence is involved (Han et al., 2001). However, whether RBC presence does in fact affect turbulence development and the specific mechanisms that may cause this behaviour remain unknown. This chapter highlights the theoretical aspects of particle-laden flows that are important to this study. The four subsections are organized as follows: particle-laden flow properties, turbulence modification by suspended particles, modes of turbulence modification, and exclusions and assumptions.

2.1 Particle-Laden Flow Properties

Particle-laden flows involve added complexity as there are increased elements of the fluid interacting. A viscoelastic fluid balances between purely viscous-fluid flow and perfectly elastic-solid deformation (Kumaran, 2010). The fluid-particle forces produce a nonlinear rheological response in these fluids (Snabre & Mills, 1998). The properties of the particles suspended in a fluid, namely volumetric concentration, size, and material properties can determine the overall bulk properties of the fluid. Similarly, RBC properties such as hematocrit, deformability, extensibility, and aggregation affect whole blood viscosity similar to particle-laden flows (White & Mungal, 2008).

Particle volumetric concentration affects fluid properties until the maximum packing fraction, where the suspension no longer flows and takes on solid-like behaviour, or infinite viscosity. For dense, hard spheres, the maximum packing fraction is approximately 67% (Snabre & Mills, 1998). As concentration of particles increases so does the effective viscosity, which was

first shown by Einstein over 50 years ago for dilute suspension of particles (Stickel & Powell, 2005). Krieger (1972) developed a model to relate the initial fluid viscosity (μ_f) to the effective viscosity (μ_e) for high particle concentrations:

$$\mu_e = \mu_f \eta_r \tag{2.1}$$

where,

$$\eta_r = \left(1 - \frac{\phi}{\phi_m}\right)^{-1.8} \tag{2.2}$$

and ϕ is the particle-phase volumetric concentration and ϕ_m is the maximum packing fraction, which for spherical particles and this work is assumed to be $\phi_m \sim 0.68$ (Matas et al., 2003). However, in dense suspensions with particle concentrations $\phi > 25\%$, the prolonged laminar behaviour, or delayed transition to turbulence, observed in practice is not sufficiently described by the increased effective viscosity alone (Matas et al., 2003). Particle-laden flow rheology is very dynamic and consequently, few dynamics are universal in particle-laden flows.

2.2 Turbulence Modification by Suspended Particles

Low volumetric concentrations (0.01% of polymer additives are common in industrial internal flow applications, as they reduce drag resistance of the fluid by up to 80% (Sreenivasan & White, 2000; Procaccia and L'vov, 2007; White & Mungal, 2008). The polymers dampen near-wall turbulence through reduced friction, altered vortex strength, and changes to the turbulent boundary layer structure (White & Mungal, 2008). Through shape change, the polymers can absorb some energy from the carrier-phase at near-wall vortices that are subsequently suppressed, and hence attenuate wall turbulence (Dubief et al., 2004). Polymers also return some energy to the fluid and in some cases the energy release induces turbulence at lower Reynolds numbers than

with the carrier-phase devoid of particles (Dubief et al., 2013). Particles can also redistribute TKE in a flow (Zhao et al., 2013). These studies considered small volume fractions of particles, between 1 to 10%, which is not directly applicable to blood flow, where RBC volumetric concentration is approximately 45% (Lucci et al., 2010; Bellani et al., 2013). However, it was shown that particles can modify turbulence by storing kinetic energy from the fluid as elastic energy.

Turbulence modulation can be a product of the particle's properties, such as elasticity as described with polymer additives. However, in suspensions of particles with minimal elastic properties, modified turbulence has also been observed (Choi et al., 2011). Rauleder & Leishman (2014) report a more rapid diffusion of vorticity downstream of a helicopter's rotor wash from dispersed, uplifted sediment. Similarly, Parthasarathy and Faeth (1990) used low concentrations of glass particles and still observed turbulence modulation. Note that glass has a Young's Modulus approximately 10^9 times greater than most common plastics (Lubliner and Papadopoulos, 2014). Particle-particle collisions affected turbulence for particles with low Stokes numbers (Stk << 1), defined by Equation 2.6 below, and collisions were most prominent in vortical regions (Choi et al., 2011).

Again, most studies in turbulence modification by particles used dilute phase concentrations (ϕ<0.01%), nowhere near the concentration of RBCs in blood, around 45%. Studies involving dense volumetric concentration particle-laden flows are generally in a laminar regime or the fluid rheology is investigated rather than its flow dynamics (Picano et al., 2014). To address the lack of dense suspension studies in a turbulent regime, Picano et al. (2014) studied ranges up to Φ=20% for spherical, neutrally-buoyant particles in turbulent flow. The added particles attenuated turbulence and particle-induced stresses were shown to increase drag, reduce velocity fluctuations, and a tendency to laminar behaviour was observed through mean velocity profiles.

In short, turbulence modification is a dynamic phenomenon with numerous possible outcomes of which none can be attributed to a single particle or fluid property, but rather a combination thereof. It is, however, well-documented that the presence of particles modifies turbulence in the carrier-phase, regardless of particle size, concentration, deformability, or elastic properties.

2.3 Modes of Turbulence Modification

Particles suspended in fluid flow can augment or attenuate turbulence, but this is reliant on a number of both particle and fluid properties including particle spacing, concentration, size, velocity and density, fluid velocity and density, and the Kolmogorov scale in fully developed turbulence. Particle-induced turbulence modification is a multifaceted phenomenon and consequently, generalizations to determine fluid behaviour are not yet conceivable. Modification is most substantial within one radius-length of the particle surface, suggesting the micro-level fluid-particle interactions are of prime importance (Burton & Eaton, 2005).

Augmentation has been observed with large volumetric concentrations of particles that cause overall TKE augmentation (Bellani et al., 2013). Turbulence augmentation in the fluid as a result of particle presence has been observed to be a mechanism of vortices and wakes shed by particles with larger response times (Poelma & Ooms, 2006; Tanaka & Eaton, 2010). Speculated mechanisms of turbulence augmentation include increased particle induced wakes and spatial velocity fluctuation from the chaotic tumbling patterns that aspherical particles exhibit (Bellani et al., 2013). Gravity or carrier-phase induced acceleration of the particles can lead to a subsequent transfer of this energy to the fluid-phase, which generates velocity fluctuations at small-scales, unsteady wakes, and consequently can augment turbulence (Tanaka & Eaton, 2010).

Attenuation produces an overall energy loss in the fluid system, however, in fully developed turbulent flow this is often associated with an increase of TKE at small, turbulent scales. Increased TKE facilitates viscous dissipation, since flow diverted around particles causes large velocity gradients and therefore large shearing and friction (Tanaka & Eaton, 2010). Overall attenuation of turbulence is a factor of frictional energy losses at the particle surface that are a result of the aforementioned velocity gradients (Schwarzkopf et al., 2009). Increased particle diameter reduces TKE dissipation for the same volume fraction, due to the decrease in particle surface area (Lucci et al., 2010). Furthermore, if particles disrupt vortex stretching, an essential phenomenon in the development of turbulent flow, a decay of existing or delayed onset of turbulence can result (Bellani et al., 2013). Large particles may also reduce turbulence by a force exchange from the fluid to the particle. A sufficiently large particle is unable to respond as quickly as the fluid to small velocity fluctuations. This results in fluid diversion around particles leading to TKE losses (Tanaka & Eaton, 2010).

Tanaka and Eaton (2008) developed the particle moment number (Pa_{Re}), a dimensionless value used to determine the turbulence modification by dispersed particles in a flow as described by Equation 2.3:

$$Pa_{\mathrm{Re}} = \frac{\mathrm{Re}_L^2}{18\,\mathrm{Re}_P}\frac{\rho_p}{\rho_f}\left(\frac{d_P}{L}\right)^3 \tag{2.3}$$

where Re_H is the Reynolds number of the flow, ρ_p and ρ_f are the particle and fluid densities, d_p is the particle diameter, and L is the characteristic length scale. Re_p is the Particle Reynolds (Re_P) defined as:

$$\mathrm{Re}_p = \frac{\rho_f |V - U| d_p}{\mu} = \frac{|V - U| d_p}{\nu} \tag{2.4}$$

where ρ_f is the density of the fluid, $|V - U|$ is the slip velocity such that U is the fluid velocity and V is the particle velocity, d_P is particle diameter, and μ is the fluid viscosity. Settling velocity was used in place of slip velocity in this study. Stokes number describes the response of the particle to the fluid based only on fluid velocity (ν_f) and particle diameter (d_p), as shown below in Equation 2.5, and thus derivations reliant upon Stk were not as accurate at predicting turbulence modification behaviour (Tanaka & Eaton, 2008).

$$Stk = \frac{\tau_p \nu_f}{d_p} \tag{2.5}$$

where τ_p is the response time defined by:

$$\tau_P = \frac{\rho_P d_t^2}{18\mu[1 + 0.15\,\mathrm{Re}_P]^{0.678}} \tag{2.6}$$

The derivation of the Pa_{Re} is based on the carrier-phase form of the Navier-Stokes equation that has been modified to account for the presence of particles. Unlike Stk or Reynolds number, the Pa_{Re} accounts for the behaviour of turbulence as it relates to particle and fluid properties when dealing with particle-laden or two-phase flows. Given the abundance of particle-laden flow properties and resultant dynamics, Pa_{Re} is an improvement over past terms to predict its rheology in turbulence. Unlike previous studies on turbulence modification, the Pa_{Re} is capable of determining the magnitude of the turbulence modification, in addition to whether augmentation or attenuation will result.

2.4 Exclusions and Assumptions

Given the aim to determine the bulk effects of RBCs on turbulent behaviour, many factors of the vascular environment are neglected, such as vessel compliance, the pulsatile nature of the flow environment, wall effects, and other particulates dissolved in the blood stream. Although these factors affect blood flow behaviour, direct interest of this work lies at a much smaller scale, specifically on the local interactions between RBCs and the fluid. The order or scale at which any RBC-fluid interactions occur are substantially smaller than those of pulsatility, vessel compliance, or wall effects whose scale is largely determined by pressure, pressure-time gradient, and vessel diameter (Ye et al., 1993). Furthermore, pulsatility and vessel compliance certainly will affect flow dynamics, but also increase the complexity of an already poorly understood problem. Accordingly, a narrow focus was chosen for this work to first determine general base knowledge of whether turbulent behaviour development is in fact affected by the presence of RBCs. Compliance and pulsatility will undeniably affect turbulent flow development and possibly RBC dynamics. However, determining any resultant combined effects on turbulent flow development is a laborious task without a baseline of RBC-fluid behaviour, which this work aims to establish.

An assumption of widespread free shear layers in arterial blood flow is conceivable given the relentless curves and branches of the arterial vasculature, but also since the endothelial wall is rough and strewn with perturbations as shown in Figures 1.1 and 1.2 (Xiang and Taylor, 2010). Furthermore, ECs can swell, distort, and aggregate creating an uneven topography at the fluid-vessel wall interface (Park et al., 2012). More prominent, but less common disturbances to flow are atherosclerotic plaque and implanted devices. There is much evidence that perturbations to arterial blood flow exist and dependent on size can induce turbulent wakes at low Reynolds number (Ku, 1997).

Chapter Three: **OBJECTIVE AND HYPOTHESIS**

The objective of this work is presented first, followed by the two study aims and each respective hypothesis.

3.1 Objective

The vast majority of studies modelling flow in large arteries model blood as a homogenous fluid of constant viscosity (Newtonian) due to an assumption of high shear strain rates at or above 100 s^{-1}, where blood viscosity approaches a constant value (Steinman, 2012). However, shear strain rates can fluctuate in the presence of developing transitional flow features, such as free shear layers and vortices, not to mention in transitional and turbulent flow regimes. Consequently, viscosity will fluctuate accordingly**.** Flow features, such as free shear layers and vortices, provide an initial point of instability from which subsequent destabilisation can form leading to transitional, and eventually turbulent flow. Free shear layers, recirculation, and weak turbulence can occur in the heart and large arteries, predominantly in areas of complex geometry such as bends, bifurcations, and stenosis (Gülan et al., 2012; Kheradvar & Pedrizzetti, 2012). A homogenous fluid assumption for blood has been shown to predict an earlier onset of transitional flow behaviour than may actually occur *in vivo*, where prolonged laminar flow behaviour speculated to be due to the presence of red blood cells (RBC) was observed (Han et al., 2001; Li et al., 2014; Walker et al., 2014).

Using a basic experimental approximation to blood, the objective of this research was to examine whether the presence of RBCs in arterial flow has a turbulence modifying effect. Particle-laden flows are well known to modify turbulence, but this has not been applied to the arterial environment and RBCs. Currently, computational modelling of the vascular flow environment has

either disregarded or oversimplified the individual presence of RBCs, or relied upon the use of single-cell dynamic modelling. Therefore, the model presented in this study aimed specifically to account for the dense suspension characteristic of blood, given the added complexity of interactions that a large volumetric concentration of suspended particles entrains. This study intends to determine the impact of suspended RBCs on the eventual development of turbulence by experimentally quantifying the contribution of deformable polymer-beads, used here as a RBC analog, to the development of an unsteady free shear layer.

3.2 Effect of Red Blood Cell Presence on Turbulence Modification in Blood

In non-biomedical flow, turbulence modification by particles has been well explored. Polymer suspensions have been studied extensively and are widely used in industrial applications as a result of their ability to modify turbulence, specifically through reduced drag and vortex formation (Sreenivasan & White, 2008; Dubief et al., 2013; Samanta et al., 2013). The polymer solutions are generally at low volumetric concentrations (ϕ<0.01%). Dense suspension rheology has also been studied extensively, however, rarely in a turbulent regime (Picano et al., 2014). Effective viscosity with an added particle-phase increases and expressions have been derived for dilute and dense suspension viscosities (Stickel & Powell, 2005). Picano et al. (2014) studied both a turbulent regime and dense volumetric concentrations of neutrally-buoyant particles (ϕ=20%) and found that the particles attenuated turbulence. Suspensions of particles modify turbulence, but it is obvious from past work that the resultant modification is highly dependent on particle properties and concentration (Tanaka & Eaton, 2008; Dubief et al., 2013). No study has focused specifically on the properties and concentrations of RBCs in the context of turbulence modification. Blood is a particle-laden, two-phase flow containing suspended RBCs. It is

reasonable to assume then that RBCs contribute to turbulence modification in blood flow. However, the presence of RBCs has only been speculated as the cause of prolonged laminar flow behaviour observed in blood (Han et al., 2001; Li et al., 2014). Furthermore, no mechanisms for how RBCs may modify turbulence have been presented (Han et al., 2001). Through experimental studies using two-phase blood analogs, Walker et al. (2014) and Li et al. (2014) found prolonged laminar behaviour similar to blood. However, the volumetric concentration of the suspension-phase was 0.02% by volume, unlike the 40 to 50% concentration of RBCs in blood. Furthermore, the particles were long-chain polymers and grossly differed in shape from that of spherical discoid RBCs.

I hypothesize that a 50% volumetric concentration of suspended super absorbent polymer (SAP) beads, analogous to RBCs in their concentration, act to *delay* the development of transitional behaviour and therefore turbulence. Specifically, the delay will be achieved by *reducing* fluid kinetic energy (KE) and velocity and *delaying* the formation of the free shear layer. To test this hypothesis, a free shear layer was generated by a plate towed in fluid *with* and *without* beads. The experiment will be scaled using Reynolds number to model physiological free shearing conditions imposed by a perturbation one order of magnitude greater in size than RBCs. Fluid velocity data was used to generate KE plots as well as Lagrangian velocity plots detailing tracked fluid direction and velocity. It is expected that these findings will demonstrate the contribution of SAP bead presence to the development of the free shear layer, which can provide insight to the particle-phase effects on turbulence.

3.3 Effect of Increasing Characteristic Length on Turbulence Modification by Red Blood Cells

The arterial system presents environments with a range of Reynolds numbers. At the aortic heart valve, Reynolds number can range between 3,000 and 8,000 (Kheradvar and Pedrizzetti, 2012). In the abdominal aorta, a Reynolds number of 600 is expected, but this can increase with exercise (Kheradvar and Pedrizzetti, 2012). Peak Reynolds number in the left ventricle of the heart can be up to 7,000 during diastole, or when blood is decelerating (Kheradvar and Pedrizzetti, 2012). Furthermore, the cyclic acceleration and deceleration of blood flow results in fluctuating Reynolds numbers from changes in velocity. Additionally, since modelling blood flow is often applied to the development of cardiovascular devices, such as mechanical heart valves, it is applicable to note that these are often associated with high Reynolds numbers anywhere between 600 to 6,000 (Kheradvar and Pedrizzetti, 2012). Finally, under pathological flow conditions, Reynolds numbers in the vasculature can be exceptionally high. A Reynolds number near 10,490 downstream of a diseased aortic valve was reported by Stein & Sabbah (1976). These values vary due to geometric changes of the vasculature, flow velocity, or complex geometries such as the tricuspid heart valves. Reynolds number would increase at and downstream of a stenosis, a topic of interest given that flow instabilities can promote atherosclerosis (Ku, 1997). Outside of a biological context, turbulence modification by particles occurs through a range of Reynolds numbers. Picano et al., (2014) observed turbulence attenuation by particles at Re=5,600, whereas Dubief et al., (2013) studied a Reynolds number range of 1,000<Re<6,000, finding turbulence augmentation. Consequently, without testing a range of Reynolds numbers for a given combination of particle and fluid properties, the turbulence modification dynamics cannot be assumed. Turbulence modification by particles is a multi-dimensional response in that particle and fluid

properties have a substantial effect on its outcome (Tanaka & Eaton, 2008). It is therefore reasonable to assume that increasing Reynolds number, which alters the viscous to inertial forcing and thus properties of a fluid, should affect the resultant turbulence modification by particles. Clearly, blood flowing through the arterial system encounters a large range of Reynolds numbers, and this is exacerbated in pathological conditions such as a stenosed artery. Therefore, it is of interest how turbulence modification by RBCs differs with increasing Reynolds number.

I hypothesize that a *delay* of the developing free shear layer by SAP beads will continue with *increasing* Reynolds number, where the delay will be characterized by a larger reduction in fluid KE and velocities over the 2-D measurement plane. To test this hypothesis, the free shear layer experiment was performed in fluids of decreasing viscosity, and thus increasing Reynolds number, *with* and *without* beads. Reynolds number was used to scale the experiment to physiological conditions. The lowest Reynolds number of 1,143 represents a small perturbation along the arterial wall an order of magnitude greater than RBCs. A Reynolds number of 10,490 models flow conditions at a perturbation on the order of an arterial stenosis in the aorta. It is expected that these findings will provide a first-order approximation to RBC effects on the development of turbulent flow dynamics *in vivo.*

Chapter Four: **METHODOLOGY**

In this chapter, the experimental set-up and procedures of the free shear layer experiment will be described with focus on the method employed to quantify the flow behaviour (particle tracking velocimetry) and subsequent post-processing.

4.1 Introduction

The experimental set-up was designed specifically for this research with the intent of modelling arterial flow subject to the effects of a free shear layer as depicted in Figure 4.1. The aortic arch is an area of three-dimensional, accelerated, and recirculating flow (inlet diameter of the aorta is 21 mm) (Gülan et al., 2012). In this chapter, the setup for testing the turbulence modification properties of RBCs, specifically the effects of RBCs on the development of turbulence regardless of other flow factors, will be described. An experimental approach was followed, employing particle tracking velocimetry (PTV) as a flow visualization technique to obtain fluid flow behaviour data within a generated free shear layer *with* and *without* the presence of added particles. PTV is a flow visualization technique that tracks individual particles through a sequence of images. It provides a Lagrangian perspective of particle displacement and therefore, velocity.

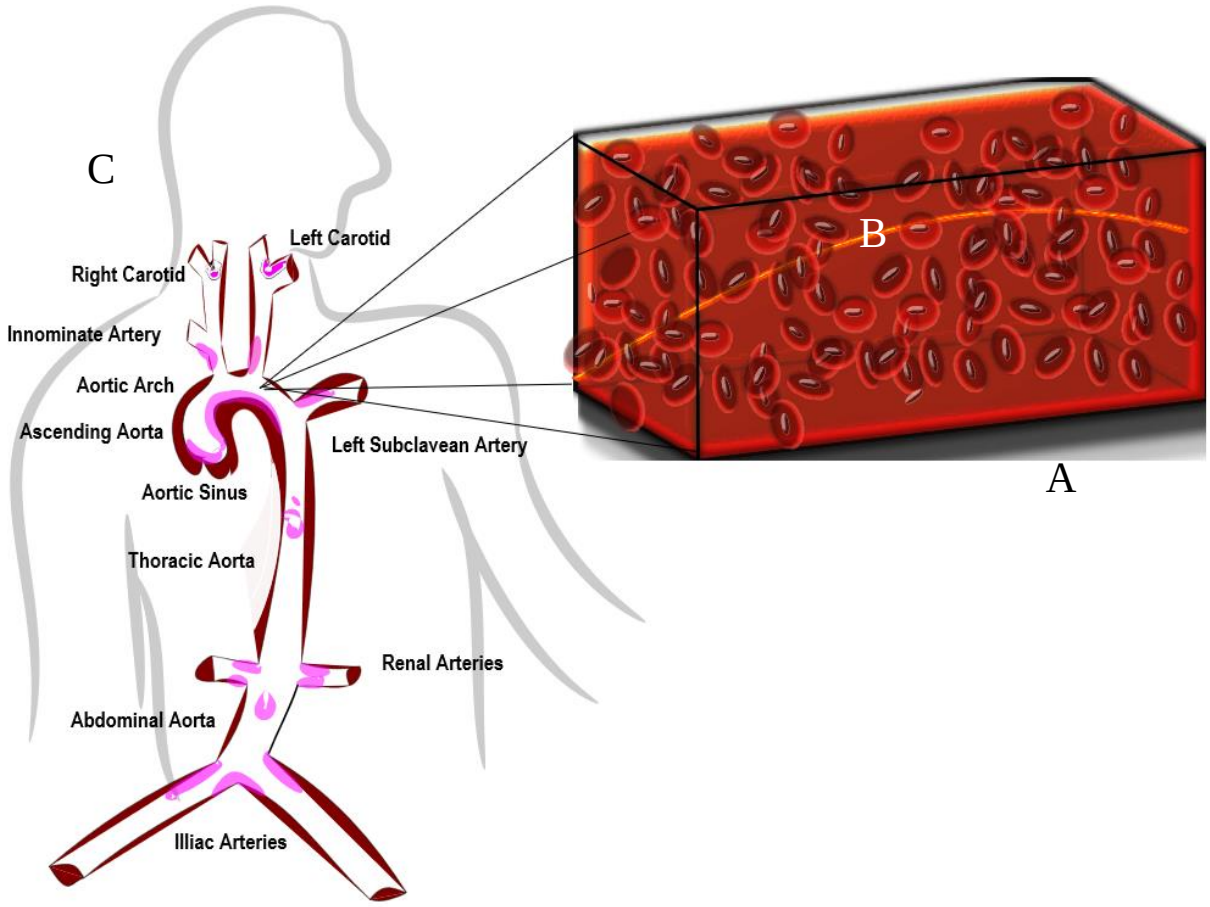

Figure 4.1: Representation of the physiological significance of the experimental set-up, where the glass aquarium is representative of an enlarged section of blood (A) flowing within an artery that is subject to the effects of a free shear layer (location denoted by B) as a result of an upstream perturbation. Areas of the arterial vasculature that are prone to atherosclerotic plaque development (C) are highlighted, as seen on the inner wall of the aortic arch (Adapted from Chiu & Chien, 2011).

A plate with a height of 10 cm (H) and a span of 3H was towed through quiescent fluid in a 110 Litre glass aquarium at a constant speed to generate a starting shear layer as shown in Figures 4.2 and 4.3. The plate height represents the characteristic length scale, or perturbation height, for Re_H calculations. The upper plate edge generates the shear layer and consequently, determines the length scale of the resultant recirculation.

The suspending fluids were tap water, and solutions of 30% (Glyc30) and 60% (Glyc60) by weight mixtures aqueous glycerol (BioShop Canada Inc., Burlington ON, Canada), equating to Re_H of 10,490, 4,581, and 1,143, for each respective solution. A constant towing speed of 0.1 m/s was used for all test cases. Thus, Re_H was controlled strictly by the suspending fluids and their respective differences in density and viscosity. The final parameter space for testing at these three Re_H values is controlled by the three aforementioned fluids, and described by a 3-by-2 test matrix shown in Table 4.1. Particles, specifically SAP beads, composed 50% of the suspension volume to model the dense particle phase characteristic of blood. Red blood cells generally compose 45% of blood's volume *in vivo* but this value can range from 34% to 52%, therefore a 50% concentration was chosen from the range for simplicity (Cokelet & Goldsmith, 1991). Reynolds numbers of 1,143 and 10,490 are associated with flows within the aorta caused by a microscopic perturbation and a significant stenosis, respectively.

Table 4.1: 3-by-2 test matrix displaying control and test cases for both turbulent and laminar Reynolds numbers (Re_H) of 1,143 and 10,490, respectively.

	Re_H = 1,143	**Re_H = 4,581**	**Re_H = 10,490**
	Microscopic Perturbation	→	Large Stenosis
Control	100% Glyc60	100% Glyc30	100% Water
Test Case	50% Glyc60 / 50% Beads	50% Glyc30 /50% Beads	50% Water/50% Beads

Note: Percentages are the volumetric ratios between the fluid and beads

4.2 Experimental Set-Up

A stepper motor with a unipolar, two-phase controller (Velmex Inc., Bloomfield, NY, USA) and traverse enable the plate to be towed through the suspending fluids. As shown in Table 4.2, the densities of the suspending fluids range within 15% of each other. Fluid physical

properties, namely viscosity and density, were determined from published values never invalidated and thus, accepted to be representative of the conditions. Physical measurement of the fluid properties was not performed due to unavailability of necessary equipment. In contrast, the viscosities of water and Glyc60 differ by more than an order of magnitude. The use of Glyc30 was specifically chosen given that its viscosity generated an intermediate Re_H between that of water and Glyc60 (Segur & Oberstar, 1951). It is therefore the viscosity that determines the Re_H values desired for these experiments, as previously described by Equation 1.1. Testing was performed at a room temperature of 22°C.

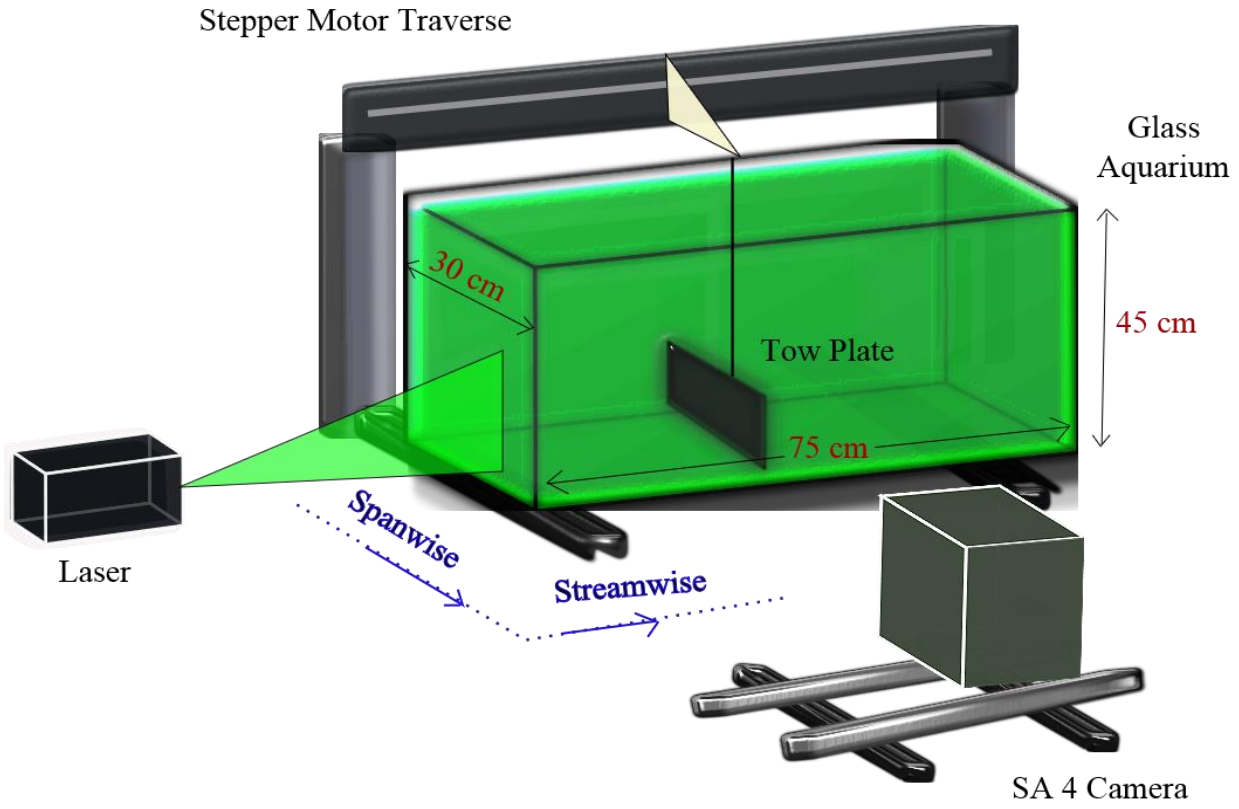

Figure 4.2: Experimental test set-up with dimensions (in red) demonstrating relative positions of equipment for PTV data acquisition and flow directionality (blue).

Table 4.2: Select physical properties of the suspending fluids at a temperature of 22°C (Segur & Oberstar, 1951).

	Density (m^3/kg)	Viscosity ($Pa \cdot s$)
Water (Re =10,490)	1005	0.955×10^{-3}
Glyc30 (Re = 4,581)	1072	2.34×10^{-3}
Glyc60 (Re = 1,143)	1154	10.1×10^{-3}

In the ascending aorta, blood velocity ranges between 0.11 and 0.66 m/s pending the period of the cardiac cycle, and velocities as high as 1.0 m/s can be expected in a healthy patient (Gabe et al., 1969; Ku, 1997). Using Equation 1.1, a small perturbation on the order of 1 mm ($H=1 \times 10^{-3}$ m) results in a Re_H of on the order of 1,000 in the ascending aorta ($Ø_{aorta}$ = 2.0 cm) assuming a high shear strain blood viscosity value of 3.5×10^{-3} Pa·s, a flow velocities up to 1 m/s, and a whole blood density of 1060 kg/m^3 (Mejia et al., 2007). For a large stenosis that causes an aortic radial reduction of 50% (H = 1 cm), a Re_H of approximately 10,000 is calculated when all other parameters are maintained as above. Reynolds numbers up to 10,000 can occur in pathological conditions in the vasculature (Stein & Sabbah, 1976). For this reason, Re of 1,143 and 10,490 were chosen for testing.

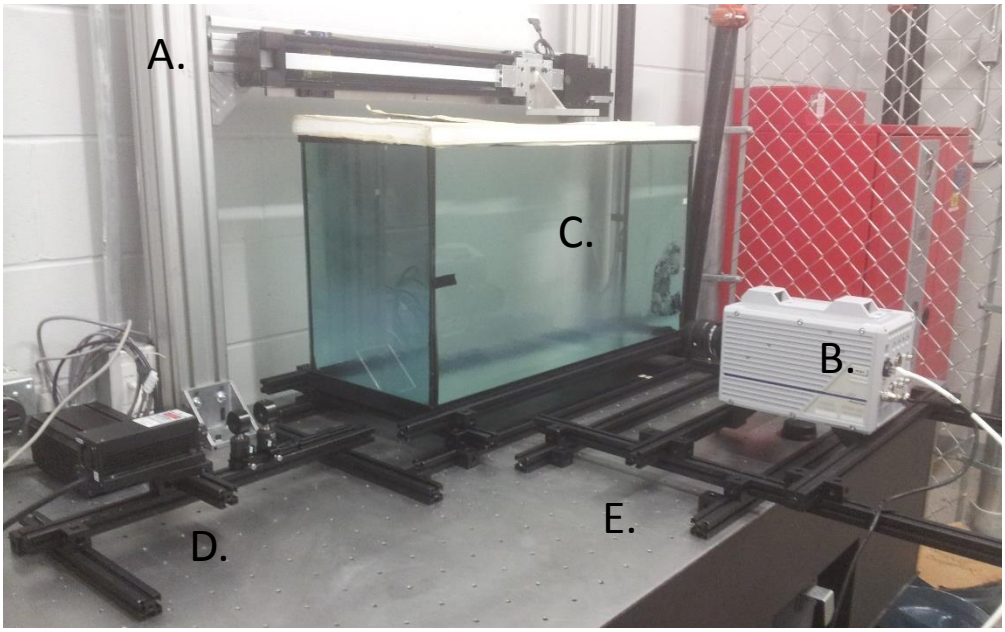

Figure 4.3: Experimental set-up of motor traverse (A), SA 4 camera (B), tank (C), laser (D), camera and tank supports (E).

4.2.1 Free Shear Layer Generation

A plate of height H=0.1 m was towed at constant speed (0.1 m/s) to generate a starting shear layer. The shear layer generated is representative of one conceivable in arterial flow as a result of a bifurcation, directional change, flow diversion, perturbation along the arterial wall, or plaque deposition. Since RBC diameter is approximately 10 μm, the ratio of free shear generator height (H) to particle diameter (d_P) of this experiment is 10, which is proportional in physiological flow to a small-scale disturbance such as an imperfection along the vessel wall. However, by using Reynolds number to scale the experiment, it was also possible to test in a flow environment similar to that generated by a large aortic stenosis (Re = 10,490) for which the H/d_P is on the order of 10,490. Due to size limitations, such a large ratio was infeasible with the current experimental set-up.

The stainless steel sting provided a connection between the stepper motor and the plate and has a diameter of 4% the aquarium width. The plate was positioned within 3 mm of the bottom and sides of the aquarium. Gaps were minimized to prevent flow from these regions from interacting with the desired shear layer developing at the top of the plate. The plate motion was initialized at a distance of 3H in the streamwise direction from the laser wall to avoid any disturbance from reflecting waves. Imaging was conducted within a field of view (FOV) at a distance between 3H and 4.2H (from the laser wall) in the streamwise direction in order to minimize any effects from the laser or far walls; see Figure 4.4.

Testing in Glyc60 was performed to model healthy vascular flow where any free shear layers are induced by irregularities of the vessel wall, curvatures, or bifurcations. Use of Glyc30 and water due to decreased viscosity while holding all other parameters constant, allowed for testing at higher Re_H.

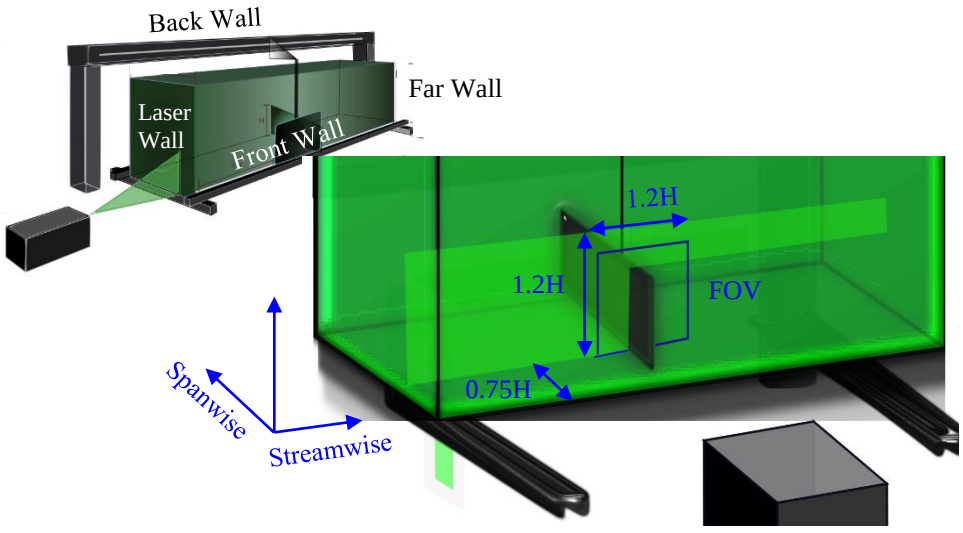

Figure 4.4: FOV location and relative dimensions based on a plate height of 10 cm (H).

4.2.2 Super Absorbent Polymer Beads as a RBC Analog

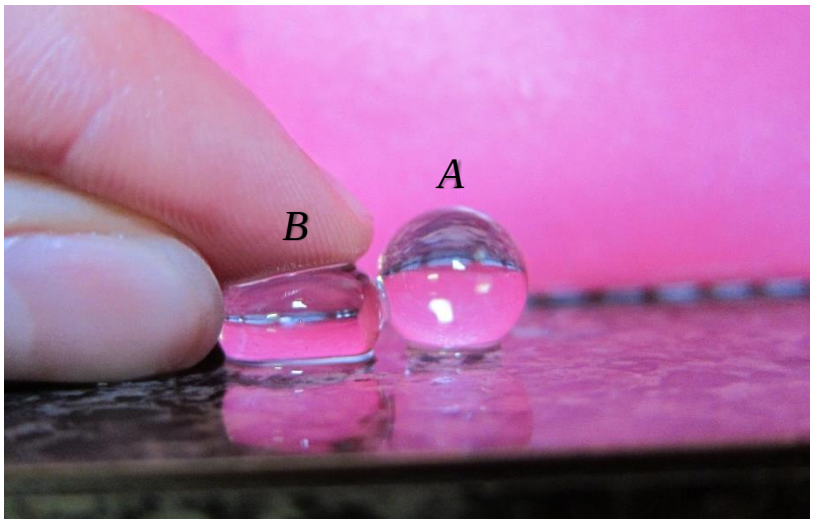

Figure 4.5: Super absorbent polymer beads (SAP) beads upon complete saturation. Here an uncompressed (A) bead relative to a compressed (B) bead is shown, demonstrating the deformability of the SAP beads (B).

Super absorbent polymer (SAP) beads (M² Polymer Technologies, Inc., West Dundee, IL, USA) with a diameter of 0.01 m, upon full saturation, were chosen for use as the particles to model RBCs. The smallest size available was chosen, so as to have the largest difference in shear generator and particle order of magnitude possible with the current experimental set-up. The SAP beads, displayed in Figure 4.5, were chosen for use in this experiment for their sphericity, elasticity, adaptable optical matching, and matching density in all of the specified suspending fluids. Super absorbent polymer beads have a coefficient of restitution (C_R) of approximately 0.7. This value is based on an average rebound height (H_F) of 0.42 m after initially dropping (H_o) 0.89 m, which is proportional to a material's final (U_F) and initial (Uo) velocities after a collision as described by:

$$C_R = \sqrt{\frac{U_F}{U_o}} = \sqrt{\frac{H_F}{H_o}} = \sqrt{\frac{1/2mU_F^2}{1/2mU_o^2}} \tag{4.1}$$

where m is the mass of the material. C_R is representative of energy lost in the collision as it relates KE energy retained, as per Equation 4.1. C_R is thus in part indicative of the elasticity of a material. Although the beads have elastic properties, the C_R of RBCs used in numerical modelling is 0.95 and therefore enforces that RBCs are more elastic than the SAP beads (Gidaspow & Huang, 2010). As a result, this work does not account for a RBC's elastic properties as a mechanism for turbulence modification, but results cannot be attributed to this alone. Furthermore, SAP beads are not nearly as deformable and malleable as RBCs, which have the consistency of a loosely inflated balloon filled with water. Poly-acrylate hydrogels, such as the SAP beads, depending on the concentration of water, have a maximal shear modulus on the order of 10^3 N/m^2 (Jiang et al., 1999; Basu, 2012). Healthy RBCs are poorly resistant to shearing given a shear modulus of 6 x 10^{-6} N/m (Waugh & Evans, 1979; Drochon et al., 1990; Hosseini & Feng, 2012).

Next, the use of SAP beads allowed for optical matching with all suspending fluids that minimized laser beam refraction. This is crucial for use of PTV technology, as a minimally refracted laser beam is necessary to ensure measurement along the 2-D plane generated by the unrefracted laser sheet. Furthermore, poor optical matching would restrict imaging to only directly at the front wall of the aquarium since the nearest beads would refract all the light, and as a result only these beads would be highly focused. In Figure 4.6, optically matched SAP beads in the top two-thirds of the aquarium (difficult to distinguish) are in direct contrast with beads that are clearly visible in the lower third of the aquarium. The distinguishable beads do not yet share the same

refractive index (RI) as the surrounding Glyc60 fluid. Consequently, more time was required for these beads to adjust before testing could occur.

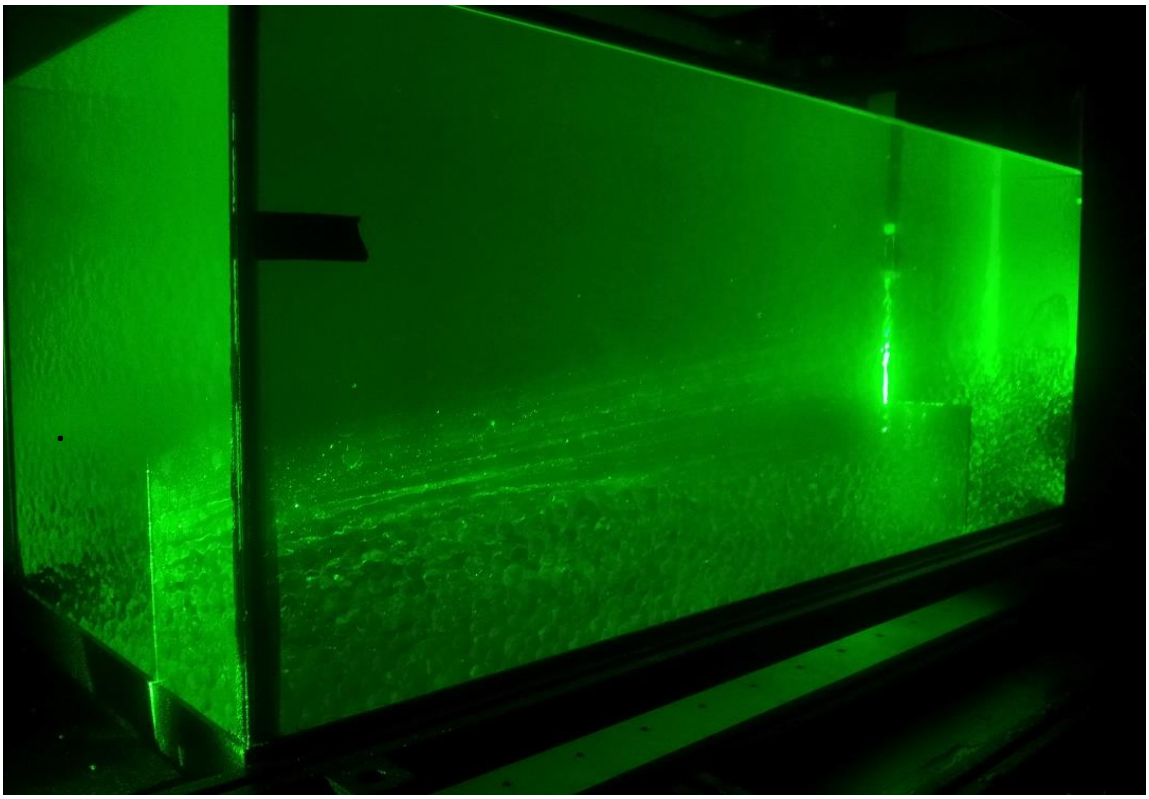

Figure 4.6: SAP Beads suspended in the Glyc60, where good optical matching can be seen in the upper 3/4 of the tank, but poor matching is evident in the bottom 1/4.

Additionally, SAP beads are near neutrally buoyant in water and both aqueous glycerol solutions, given enough time to adjust in each respective fluid. Immersed SAP beads absorb the surrounding fluid and thus become largely comprised of this fluid. The RI and density properties of the beads are comparable to those of the fluid, as demonstrated by their neutral buoyancy and the inability to discern beads from the fluid upon immersion. During testing, beads were fully saturated and no longer expanding. RBCs have a propensity to aggregate and are well-known to have complex settling patterns such that the sedimentation rate is used diagnostically as an

indicator for certain inflammatory disorders (Grzegorzewski et al., 2009). The sedimentation rate of RBCs is measured in millimeters per hour and indicative of just how slowly RBCs settle, further supporting that these cells are near-neutrally buoyant (Preedy & Watson, 2010). Furthermore, RBCs have been shown to have an average peak velocity of 6.9 mm/s that is slightly lower than that of plasma at 7.0 mm/s, suggesting that RBCs do not perfectly follow the flow despite a low (Stk << 1) Stokes number (Sugii *et al.*, 2005; Thiriet, 2007). The SAP beads used in this project to model RBCs are very similar in that they are near-neutrally buoyant, as proven by their observed settlement when left for prolonged periods of time (several hours). To aid buoyancy and optical matching, 1200 mL of sugar (volumetric concentration of approximately 1%) was added to the suspending fluids as a means of increasing the fluid's density. The dissolved sugar was present in both the "non-bead" and "bead" cases.

Super absorbent polymer beads are deformable as they have elastic properties as shown in Figure 4.5. Given enough compression or tension during manipulation, the SAP beads will tear. As mentioned earlier, the aim of this project is to verify whether RBC presence affects turbulent flow development. Past work has shown that particle elasticity contributes to its ability to store and dissipate absorbed energy, which plays a role in turbulence modulation (Zhao et al., 2013). Some deformability of particles is thus desirable in the experimental RBC-model to account for the possibility of RBC's material properties affecting turbulence modification. However, the intent of this research is a first approximation to learning how RBCs modify turbulence and therefore, an exact match in particle-to-RBC material properties is not necessary.

Optical property matching between each of the three solutions and the added beads was validated by the use of a calibration target branded with a 1 x 1 cm grid depicted in Figure 4.7. The calibration target provided a means of confirming RI matching between the beads and

suspending fluid through an absence of grid distortion, indicating both particle and fluid share similar optical properties. Also, with the glycerol solutions, optical clarity confirmed complete mixing throughout the tank. Furthermore, the target was utilized to ensure that the camera was focused on the xy-plane (measurement plane) later illuminated by the laser and to later calibrate pixel size to physical length in the FOV for data processing.

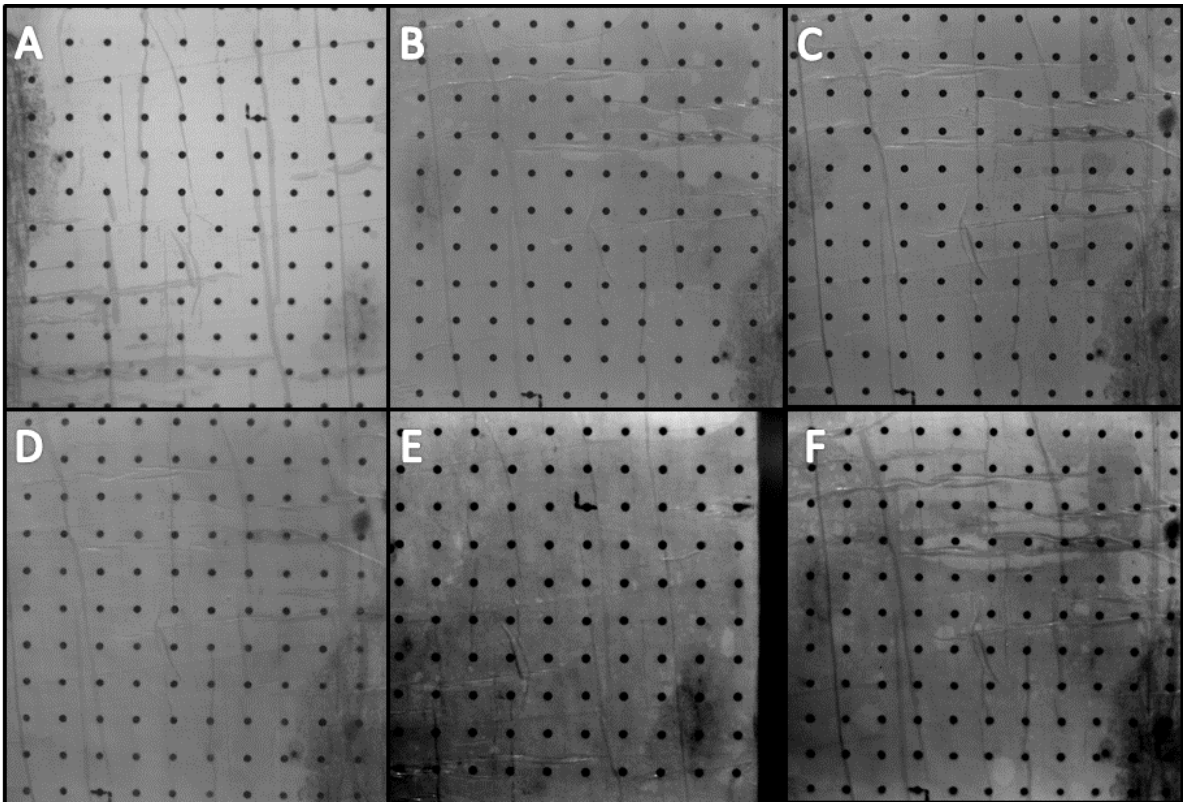

Figure 4.7: Images of the target used later for calibration of pixel size to physical length during data processing. The target is placed at the laser plane location, where measurement of the fluid is performed – 0.75H from the front aquarium wall. Shown are test cases of water (A), Glyc30 (B), Glyc60 (C), water with 50% beads (D), Glyc30 with 50% beads (E), and Glyc60 with 50% beads (F). In cases where no beads are present (top row) thorough mixing of the solutions is confirmed by these images from a lack of distortion of the grid points. In cases with beads (bottom row) optical matching between the beads and suspending fluid is demonstrated, also by a lack of distortion of the grid points.

4.3 Flow Visualization: 2-D PTV

4.3.1 PTV System and Data Acquisition

Data collected in experiments was analyzed using 2D PTV. PTV is useful in applications with low particle seeding density, where it is possible to distinguish and track individual particles. The presence of beads, used in this case to represent RBCs, restricts the region for tracer particles to the spaces between the beads and thus presents an ideal flow environment for the use of PTV. The addition of the SAP beads restricted the presence of tracer particles to the empty void between beads. The fluid was seeded with neutrally buoyant 100 μm hollow glass sphere tracer particles with a manufacturer specified effective density of 210 kg/m^3 (Potters Industries, Carlstadt, NJ, USA). Using Equation 2.5, a Stk of 2.4 x 10^{-3} was calculated, indicating that the tracer particles should faithfully follow the flow (Kaminsky et al., 2008).

The tracer particles were illuminated using a solid-state, 532 nm continuous wave 1 W laser (Dragon Lasers, Changchun, Jilin, China) with a sheet thickness of 1.5 mm. Time-resolved PTV measurements were collected along the measurement plane, as shown in Figure 4.4. Images amenable to 2D-PTV analysis in both "non-bead" homogenous and "added bead" non-homogenous free shear flow were acquired using a Fastcam SA-4 camera (Photron, San Diego, CA, USA) with a 28 mm Nikkor lens at 125 Hz and a resolution of 1024 x 1024 pixels. The laser-produced measurement plane was positioned at a distance of 0.75H, equidistant between the front wall and sting, so as to reduce any potential effects from either. Images of the illuminated tracer particles were acquired within a field of view (FOV) of approximately 1.2H x 1.2H located a distance of 3H downstream from the laser wall to further mitigate any potential wall effects on flow behaviour, also displayed in Figure 4.4.

Each set of data was collected at 3-minute intervals to allow adequate time for the suspending fluid to settle. For each respective fluid, data was first collected for the "non-bead" case. Subsequently, beads were added and given time to adjust to the carrier-phase before any tests were performed. This order was to ensure that the carrier-phase remained at a consistent concentration upon the addition of beads.

Acquired images from 20 runs for the "non-bead" case and 100 runs for the "added bead" case, to achieve an approximate equal number of identified particles per run, were imported to DaVis 8.1.3 (LaVision GmbH, Goettingen, Germany) for PTV analysis. Target images collected (Figure 4.7) were used for calibration in DaVis to ensure appropriate scaling during processing. The raw images were brightened by a fixed factor (100 pixel local average smoothed over) and particles were identified using a particle intensity threshold limit of 100 pixels to achieve a recommended particle image (e.g. added tracer particles) density of approximately 0.005 particles per pixel (ppp) in the "non-bead" case (Cierpka et al. 2013). Equivalent pre-processing of the "added bead" images generated a reduced particle-image density of approximately 0.001 ppp, which was mitigated by increasing the number of acquired runs by a factor of five. The allowed velocity range for particle tracking, used to limit results by known velocities of the flow field, was set to 0±15 pixels. Time series data settings allowed for a vector shift and maximum relative acceleration of 1.3 pixels and 0.5 dV/V between frames, respectively. Finally, no Gaussian smoothing or sharpening was applied.

The main sources of error using PTV relate to the particle tracking, as this method does not impose systematic error (Cierpka et al., 2013). The tracer particle density cannot be too high, however, as this can contribute to variability in the results. Random errors can occur if the algorithm incorrectly identifies a particle's position or tracks a different particle in lieu of the

original in a subsequent frame. As a result the seeding density cannot be too high so as to increase the occurrence of these random errors, however, it needs to be sufficient to describe the fluid motion over the measurement area. A density of 0.005 particles per pixel minimizes tracking errors to less than 5% (Cierpka et al., 2013).

4.3.2 Post-processing

Lagrangian velocity data from the added tracer particles, using a lower limit particle track length of two consecutive images, was exported to MATLAB R 2011a (Mathworks, Natick, MA, USA) for post-processing. Several additional results were derived using the velocity data generated from the initial processing in DaVis 8.1.3 and described below.

First, Lagrangian velocity plots were generated to display the physical trajectories of the tracked particles in combination with the magnitude of their velocities. Tracked particle velocities were normalized by the tow plate velocity of 0.1 m/s, and FOV dimensions were normalized by H, for all cases.

Kinetic energy (KE) plots display normalized KE magnitude (KE_f), calculated based on Equation 4.3, and the location of each particle plotted. The KE_f plots enabled analysis of both the distribution and magnitude of KE in the fluids. This particle KE_f plotted was normalized by the KE of the freestream, derived using freestream velocity (U_o) or plate velocity, and assuming equivalent mass between each particle tracked and the respective freestream element.

$$KE = \frac{1}{2} mv^2 \tag{4.2}$$

$$KE_f = \frac{\frac{1}{2}\sqrt{U^2 + V^2}}{\frac{1}{2}\sqrt{{U_o}^2}} \tag{4.3}$$

Assuming a low error in the plate tow, or freestream, velocity since the velocity increments of the motor powering the tow plate are small in comparison to the tow velocity. The operation of the motor is in steps per second, where 400 steps equate to 0.1 and so a deviation on the order of 1 step per second is negligible. Resultantly, if a maximum error from the PTV derived velocity data is 5%, a half of this would be expected for the error in KE_f based on the derived error in Equation 4.4.

$$\frac{\delta KE_f}{KE_f} = \frac{1}{4}\frac{\delta V + \delta U}{V + U} + \frac{1}{4}\frac{\delta U_o}{U_o} \tag{4.4}$$

Clearly, KE_f is mainly sensitive to error associated with the velocities from the PTV analysis. The error associated with the PTV measurements in the suspension cases would not be reflected by the above analysis because the optimal particles per pixel stated is for a single phase fluid. Correlation between tracked fluid flow patterns and observed fluid behaviour can provide insight as to the PTV tracking effectiveness. Given the qualitative nature of the results, such as observation of flow patterns, a thorough analysis of the propagation of error is not deemed necessary.

Specific time (t^*) points were then chosen for comparison of the data between the six cases. A time corresponding to partway through the tow will be chosen to analyze the development of the free shear layer. A later point near the end will be assessed as well since shading by the plate will be minimized allowing for a better distribution of data through the FOV. Time (t) was non-dimensionalized (t*) by H and plate tow speed (υ) using:

$$t^* = \frac{t}{H/\upsilon} \tag{4.5}$$

4.3.3 Data Validation

Prior to using collected and processed data for the analysis of results, consistency in plotted fluid flow patterns, average velocity, and KE values were compared between initial and final runs collected. This was to test whether any systematic errors had been imposed throughout the data collection. For example, if fluid was not allowed to settle sufficiently between test runs, initial fluid motion could affect a subsequent test run.

Lagrangian plots ensured that consistent particle tracking had occurred in both space (x/H) and time (t*). Lagrangian particle tracks are plotted over the FOV displaying respective velocity magnitude. These plots allow for a visual check to determine whether particles are dispersed throughout the FOV. These plots were also compared to raw video files as a preliminary baseline check between tracked results and real fluid flow patterns.

Given that 2-D PTV analysis is performed on a plane, limitations in particle tracking due to the 3-D motions of particles can arise (Cierpka *et al*., 2013). Through processing in DaVis 8.1.3, data tracked through 3 frames (track length of 2) or less was not included in the data set. Particles tracked over fewer imaged frames, or with shorter track lengths, do not provide as robust of data. A particle that is tracked longer increases the existing information of its motion to better predict and help locate the same particle's future position (Cierpka et al., 2013).

Finally, in an effort to reduce error, a consistent amount of particles tracked was maintained for all test cases. By constraining the minimum track length (min TL), which represents the fewest number of frames through which a particle is tracked in order to be considered in calculations, allowed for the maintenance of approximately 35,000 particles for each test case. Table 4.3 shows the min TL used in each case and the amount of resultant particles identified that were used for the generation of results presented. This is an effort to maintain a comparable amount of tracks and

thus data points for each test case. An uneven spatial distribution of particles tracked, for example, a greater density of particles tracked in an area of fluid with elevated KE, would artificially elevate average KE results at the time of interest. Furthermore, summation of KE to calculate a KE, without a consistent amount of particles, would also result in elevated KE results for a case with more particle data.

Table 4.3: Minimum track length (Min TL) constraints set for post-processing and the resultant number of particles tracked

Case	Min TL	Particles Tracked
Water	11	39,089
Water w/Beads	8	46,740
Glyc30	8	40,835
Glyc30 w/Beads	5	44,881
Glyc60	10	38,741
Glyc60 w/Beads	7	34,665

Chapter Five: **RESULTS**

This chapter begins by discussing high speed imaging acquired during the free shear layer experiments. Then, Lagrangian velocity and kinetic energy (KE) results are presented and each fluid *without* beads is compared to its respective suspension case. This is followed by an analysis of the suspension cases as Reynolds number (Re) is increased. Finally, mechanisms to explain the results are proposed preceding concluding remarks on the relevance of the findings to turbulence modification by red blood cells (RBC) and the arterial flow environment.

Section 5.1 confirms the presence of a free shear layer prior to the addition of super absorbent polymer (SAP) beads by analysis of the high speed imaging acquired during the experiments. Through observations of the flow features developed in the fluids, the presence of the free shear layer and therefore a transitional flow regime are established.

Section 5.2 addresses the first aim, which is to determine whether the presence of RBCs suspended in a fluid affect the development of transitional flow behaviour. To aid in the comparison of flow *with* and *without* beads, plotted particle KE derived from tracked fluid velocities and Lagrangian velocity plots are presented. The plots reveal fluid flow patterns, velocity magnitudes, and the distribution and magnitude of KE. With these results, each of the three homogenous fluid cases is compared to its respective suspension case to assess the contribution of SAP beads to the developing free shear layer.

Section 5.3 examines the second aim of this study. Here it is determined whether increasing Reynolds number alters the resultant contribution of RBCs to a developing transitional flow. Fluid behaviour is analyzed with the previously presented KE and Lagrangian velocity plots, but here the focus is on fluid dynamics with increasing Reynolds numbers from 1,143 to 10,490.

.

5.1 Evidence of an Established Free Shear Layer

As a means of confirming that a free shear layer was generated by the plate prior to the addition of beads, behaviour of the three suspending fluids *without* beads is discussed using the high speed imaging obtained during data collection.

5.1.1 Starting Vortex and Free Shear Layer at Re=10,490

Fluid behaviour at Re=10,490 (water) *without* SAP beads is discussed in reference to Video 5.1, recorded during Run 1 (of 20) in water. Correlation with Figure 5.1 can help with the identification of flow features. Figure 5.1 shows frames 130 to 138 (out of 150) superimposed for fluids *without* beads (top row). These subsequent images were chosen specifically at time points towards the end of the tow in order to have a larger portion of the starting vortex imaged and less area in the FOV shadowed by the plate.

For fluids *without* beads, the most prominent feature in the flow was the development of a starting vortex as a result of the plate motion. The vortex rollup begins at the plate tip, which represents the point of separation (Lian & Huang, 1989). Quiescent fluid is at the upper boundary of the shear layer, where it is originally undisturbed with an initial velocity U_o=0 m/s. The starting vortex creates a strong velocity gradient and thus, a free shear layer, with the quiescent fluid above as denoted in Figure 5.1. From the point of separation at the edge of the plate, the free shear layer travels toward the top left corner of the field of view (FOV); see Figure 5.1.

Focusing on the core region of the starting vortex, the center of recirculation travels in both the x and y-directions, and as a result appears to "bounce" around. This 2-D motion makes the core region appear less stable. The increased instability of this region is more obvious in contrast to the Re=1,143 fluid discussed below.

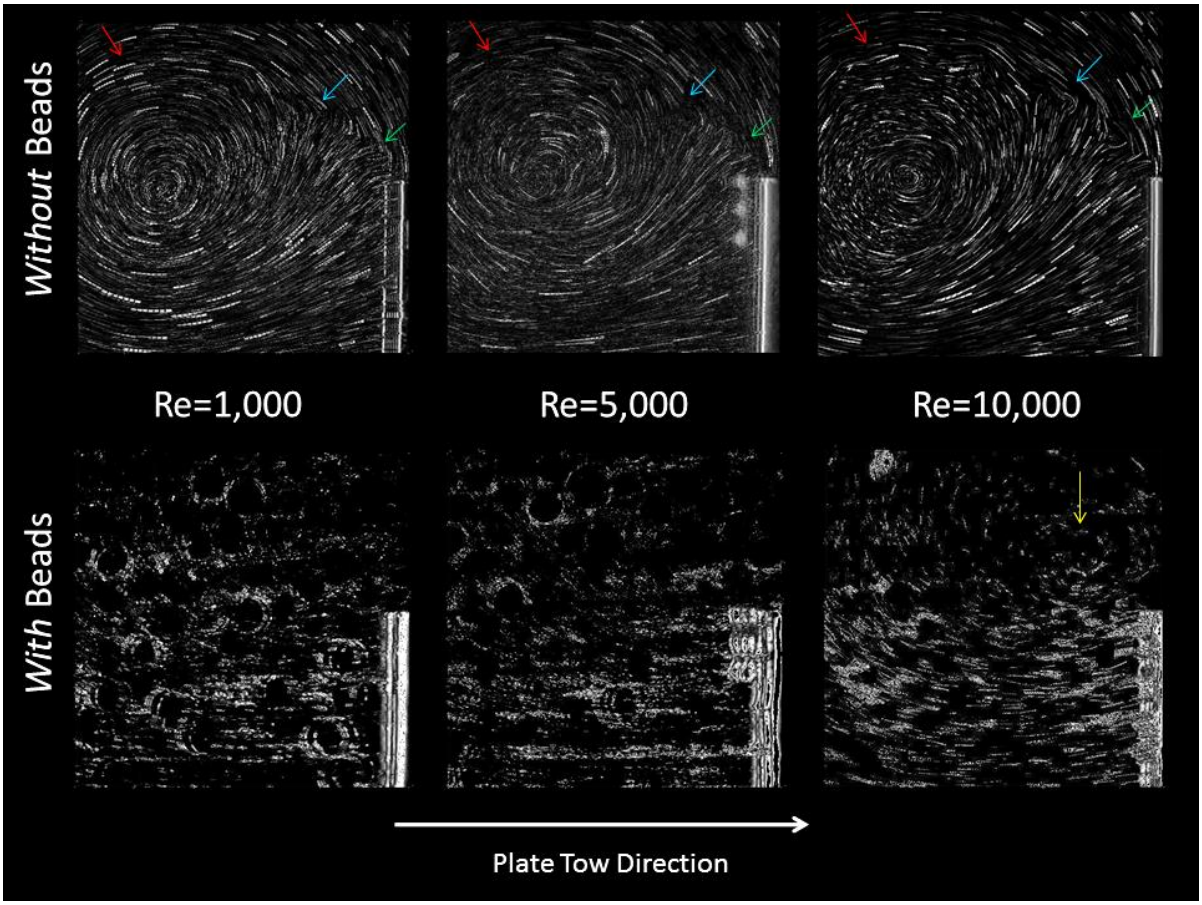

Figure 5.1: Raw images of frames 131 to 138 (of 150 total) superimposed from a single run, where plate motion is from left to right. Shown are Reynolds numbers (Re)=1,143, 4,581, and 10,490 for cases *without* beads (top row) and *with* beads (bottom row). The green arrow identifies the free shear layer shortly after being generated at the plate tip, and the blue arrow identifies where the free shear layer and the outer rings of the starting vortex appear to interact. The red arrow shows the location where at Re=10,490 and 4,581, small vortices within the free shear layer are exiting the FOV and the respective location is also shown at Re=1,143, although these instabilities were less apparent; see Video 5.1. The yellow arrow denotes a speculated vortex core in the data *with* beads that is most apparent in the Re=10,490 image.

In Video 5.1, vortical instabilities are apparent in the free shear layer. These vortices are small relative to the length of the main vortex and are forming at its edge. This is in agreement with starting flow theory described by Lian & Huang (1989), indicating that this is indeed a starting vortex with an associated free shear layer. The vortices in Video 5.1 propagate with the free shear layer, following its trajectory towards the upper left corner of the FOV along the outer boundary

of the starting vortex. The free shear layer instabilities initiated by the plate tip and located at the edge of the starting vortex display a shear layer initially, followed by a region of evenly spaced small vortices, in agreement with Lian & Huang (1989); see Video 5.1. The starting vortex grows as the plate travels right (+x-direction). The vortex would presumably reach a limiting size if the recording were to continue.

5.1.2 Starting Vortex and Free Shear Layer at Re=1,143

Proceeding to the lowest Reynolds number case *without* beads (Re=1,143), a discussion of the observed flow features follows, always in reference to the high speed imaging collected during Run 1 (of 20) through Glyc60; see Video 5.2.

A shear layer propagates from the tip of the plate and toward the top left corner of the FOV, as seen previously at Re=10,490. Similarly, quiescent fluid and the starting vortex create the upper and lower boundaries of the free shear layer, respectively and the starting vortex grows in size, as with the Re=10,490 case.

In contrast to the Re=10,490 case, fewer vortical instabilities are seen in the free shear layer at Re=1,143. Since less vortices are observed over the same length of time, they are shed at a lower frequency. Finally, the starting vortex center travels mainly along a linear path in the x-direction, following the plate. The 1-D motion of the vortex core at Re=1,143 gives an impression of more stable motion relative to Re=10,490.

In summary, for 1,143<Re<10,490 the fluids *without* beads exhibit a free shear layer and as Reynolds number increases vortices are shed at a higher frequency from the plate tip. In addition, the starting vortex translation becomes more 2-D with increased Reynolds number. However, the high speed imaging analyzed in Videos 6.1 and 6.2 are only of a single run, therefore it is recognized that only tentative conclusions can be made from this evidence.

5.2 Effect of SAP Bead Presence on a Developing Free Shear Layer

As a means for determining the contribution of SAP beads to the development of a free shear layer, fluid behaviour *with* and *without* beads is presented. An analysis of tracked fluid velocities precedes a discussion of the Lagrangian velocity plots, which were generated to better visualize the velocity data and thus, the contribution of beads to fluid behaviour.

5.2.1 Velocity Statistics

Table 5.1 presents statistics of the tracked particle velocity results obtained from pre-processing in DaVis 8.1.3. The statistics are using data over the entire FOV. The individual components of velocity (U and V) were normalized by the plate, or freestream velocity (U_0=0.1 m/s). The velocity data was not normally distributed and thus, median values were used for comparison. Using median values reduces the effects of outliers and it is less skewed by a large spread of data. The mean was used to compare the overall magnitudes of velocity $U_T=[U^2+V^2]^{1/2}$, as these values were generally normally distributed; see Appendix B for graphical evidence of data distributions as well as results from statistical hypothesis testing.

Comparing the resultant fluid velocities *with* and *without* beads, the median U-values are increased from approximately $U/U_o=0$ upon the addition of beads; see Table 5.1. In contrast, median V-velocities are decreased to values near $V/U_o=0$ once beads are added. A median $U/U_o=0$ suggests that either the positive and negative x-direction fluid motion was equated over the length of the tow, or that values were generally near zero. Since the median absolute values of both U-component (|U|) and V-component (|V|) velocities are non-zero, the former is true. As a result, it is concluded that adding beads influenced general fluid motion in the direction of the plate (+x-direction). Furthermore, the presence of beads reduced an upward (+y-direction) flow tendency

previously present in the fluids *without* beads. These trends were apparent regardless of Reynolds number.

Table 5.1: Velocity statistics of tracked particle data over the FOV obtained from pre-processing in DaVis 8.1.3. These values were obtained using data from all runs performed.

		Reynolds Number	Median U	Median V	Mean U_T*	Median |U|	Median |V|	Std** Ut
Without Beads	**Water**	10,490	0.000	0.542	1.155	0.737	0.589	0.486
	Glyc30	4,581	0.327	0.521	1.350	0.868	0.754	0.532
	Glyc60	1,143	0.000	0.565	1.255	0.719	0.660	0.534
With Beads	**Water**	10,490	0.556	0.000	0.923	0.587	0.438	0.511
	Glyc30	4,581	0.426	-0.083	1.144	0.789	0.610	0.555
	Glyc60	1,143	0.394	-0.093	1.074	0.742	0.566	0.540

*U_T is the total velocity magnitude, $U_T = (U^2+V^2)^{1/2}$
*Std denotes standard deviation

Each fluid displays a reduced |U| *with* beads compared to *without*. Specifically, at Re=10,490 (water) the presence of beads reduces |U| by 26% compared to 10% and 7% for Re=4,581 and Re=1,143, respectively. Similarly, beads reduced |V| by 34% at Re=10,490 compared to 24% and 17% for Re=4,581 and Re=1,143, respectively. The mean total velocity (U_T) is decreased at all Reynolds numbers when SAP beads were added and again, water sees the greatest velocity reduction. This suggests a stronger modification to the flow when beads were added at Re=10,490.

5.2.2 Lagrangian Velocity Plots

The horizontal component of tracked velocity (U) indicated by colour and the physical trajectories of the tracks are plotted in Figure 5.2. Velocity and FOV coordinates, for both the vertical (y) and horizontal (x) planes, were normalized by the plate velocity (U_o) and height (H),

respectively. The U-component of velocity is shown in Figure 5.2 to better highlight locations of flow opposite to that of the plate motion. A positive U-velocity indicates flow following the plate motion (left to right). Data was constrained by the minimum track lengths (min TL) specified in Table 4.3, to maintain consistency amongst results presented.

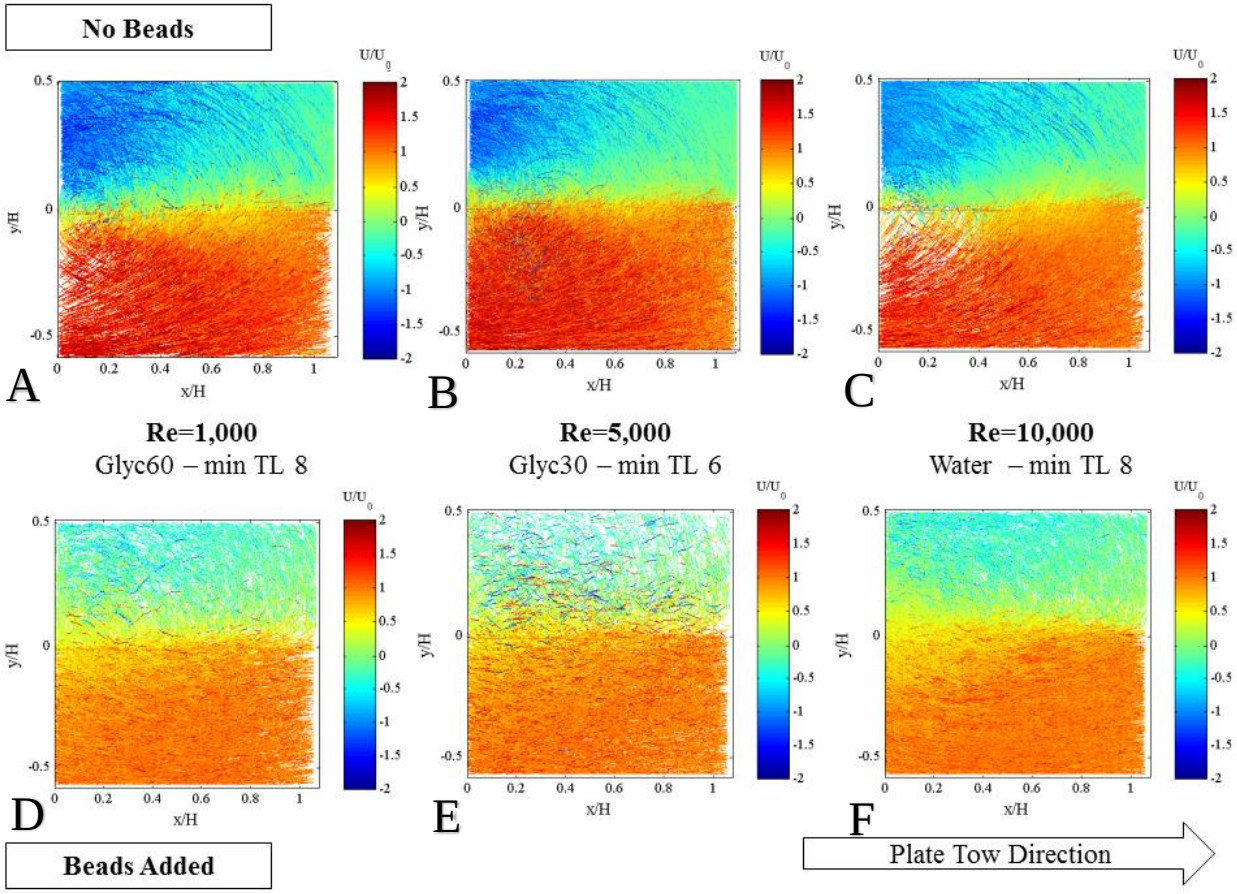

Figure 5.2: Tracked particle pathlines plotted together in a single plot for each case using data obtained from all runs (20 for cases without beads and 100 runs for cases with beads). Each plot is a collection of the pathlines throughout the entire length of the plate tow. Colouring denotes a particle's velocity at each tracked location creating a respective pathline. Cases are shown at Reynolds numbers of 1,143, 4,581, and 10,490 using Glyc60, Glyc30, and water as suspending fluids, respectively. Both cases *without* beads (top row) and *with* beads (bottom row) are presented. The plotted tracks were constrained with minimum track lengths stipulated by Table 4.3. Velocity and dimensions are normalized by the freestream velocity (U_o) and plate height (H), respectively. Plate tow direction is from left to right and the plate tip is at y/H=0 and extends down to the x-axis.

The Lagrangian velocity plots show substantial differences between the fluids *with* beads (top row) and *without* (bottom row). A reduction in maximum U-velocity is apparent. In agreement with the results from Table 5.1, regardless of Reynolds number, *with* beads the highest track velocities U/U_o are less than 1, whereas all three fluid cases *without* (top row) beads have velocities U/U_o up to 2.

At all Reynolds numbers *without* beads, the flows show a circulating flow pattern as demonstrated by the opposing flow directions in the top and bottom halves of the FOV; see Figure 5.2. In the suspension cases there is no definitive starting vortex; see Figure 5.1. Furthermore, tracks display mainly positive U-velocities, supporting results from Table 5.1, where median U-velocities were increased *with* beads. The lack of a visible starting vortex *with* beads in Figure 5.1 is either a suppression of its formation, or a vortex of much larger scale than the FOV is still present.

5.2.3 Kinetic Energy and the Free Shear Layer

A starting vortex and a free shear layer with vortical instabilities were apparent in the fluids *without* beads; see Video 5.1 and Figure 5.1. No free shear layer or vortical instabilities were visible upon the addition of beads, for the range of Reynolds number tested. The Lagrangian velocity plots present qualitative results supporting observations from Video 5.1. However, quantifiable evidence of change is limited only to velocity direction and magnitude. As a result, kinetic energy (KE) was calculated, as per Equation 5.1, to further quantify differences between the 6 test cases. The exact same amount of KE was delivered to the fluid by the plate in all cases, regardless of Reynolds number or the presence of beads. Therefore, any changes to the magnitude or distribution of KE in a fluid, apart from losses due to viscous energy dissipation, describes a response of the fluid.

$$KE = \frac{\frac{1}{2}(U^2 + V^2)}{\frac{1}{2}U_o^2} \tag{5.1}$$

In Figure 5.3, the KE of each particle tracked at two specific time points from the ensemble of runs performed, is plotted. For example, data from frame 116 (t*=0.93) was extracted for each of a 100 runs to generate the respective plots for Re=1,143 *with* beads (D). Constraints on min TL were applied to the data as per Table 4.3. The KE plotted for each particle was normalized by the freestream KE, assuming each tracked particle represents a fluid element of equivalent mass in the freestream. The magnitude of KE is represented by the colour map such that a darker red coloring indicates a higher KE according to the scale below the figure; see Figure 5.3.

A shear layer is a region of strong velocity and therefore KE gradient, given that KE is proportional to U_t^2. As a result, it was concluded that the arc-shaped sharp gradient in KE values originating near the tip of the plate is the free shear layer. Higher KE along the free shear layer is shown relative to the quiescent fluid above and the edges of the vortex below. This is further supported by a comparable location of the free shear layer as observed in Video 5.1 and Video 5.2. The lack of an identifiable free shear layer *with* beads in the KE plots, is also in agreement with observations from the raw images; see Figure 5.1. There is a high region of KE in the starting vortex core, located by association to Figure 5.1. Elevated KE in the core is expected due to increased angular velocity here. A decrease in KE from the vortex core to its extremities is shown in Figure 5.3. The outer edges of the vortex have low relative KE and extend to the free shear layer, where a return to higher KE values, near 1.5 are not surprising given the observed vortical instabilities; see Video 5.1 and Figure 5.1.

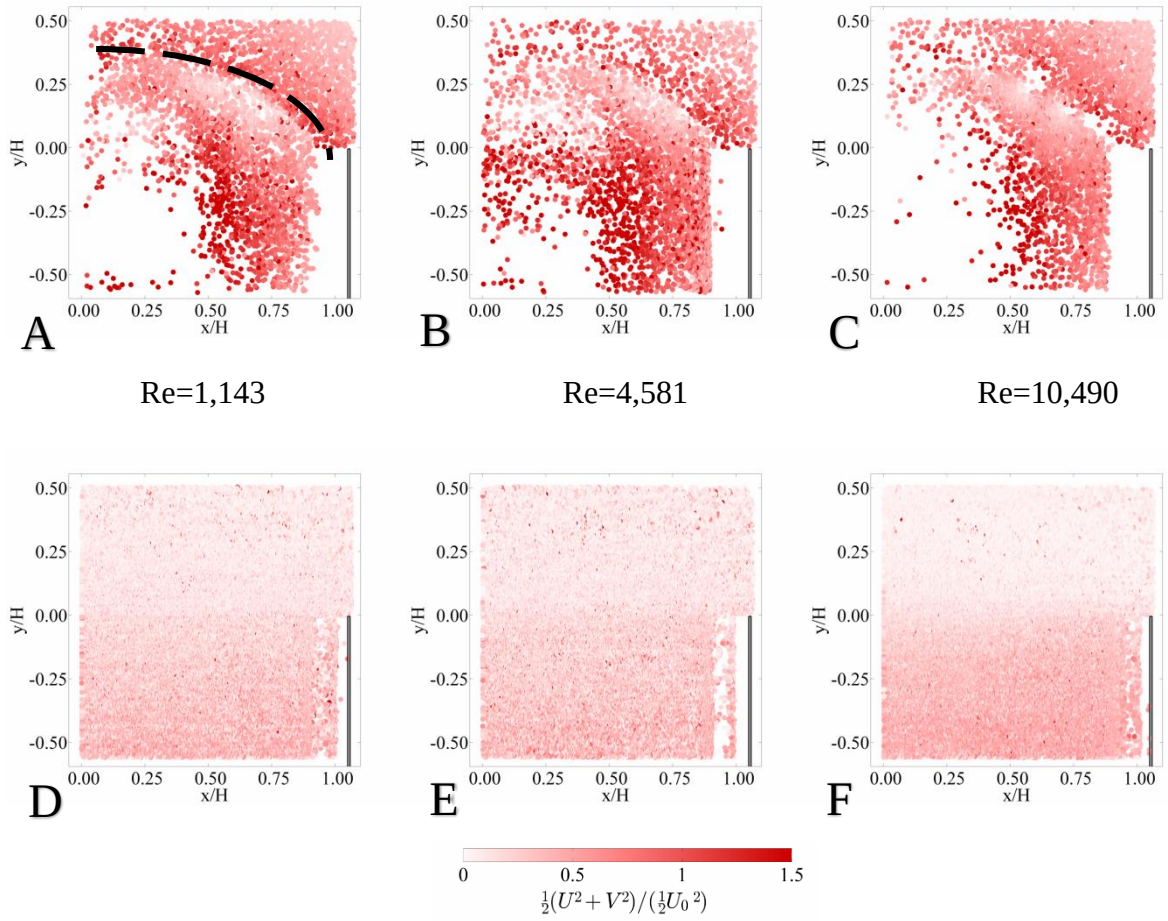

Figure 5.3: Kinetic energy (KE) ratio of each particle's energy as a fraction of the freestream. Dashed line indicates the location of the identified free shear layer in (A). Shown is t*=0.93 (frame 116/150), where KE was calculated using velocity data with minimum track length (min TL) constraints outlined in Table 4.3. The location of the plate is shown at the selected t*. Reynolds numbers of 1,143, 4,581, and 10,490 are presented for both "non-beaded" (top row) and "beaded" (bottom row) cases. All lengths are normalized by plate height (H).

Although the same amount of KE is being delivered to the fluid by the plate for all particle concentrations, the maximum KE observed in the fluid *with* beads is approximately half that of the respective fluid *without* beads; see Figure 5.3. With beads present (bottom row), the highest KE observed in the fluid is approximately KE=0.75.

In the fluids *without* beads, there are three sharp gradients in KE indicative of the free shear layer and the starting vortex; see Figure 5.3. Figure 5.4 shows the Re=1,143 case *without* beads

(A), arbitrarily chosen as an example to highlight these KE gradients that are present at all Reynolds numbers. At x/H=0.5 and between 0<y/H<0.25, from a central region of the starting vortex and toward its edge (just prior to the free shear layer), KE decreases from KE=1.5 to near KE=0.25; see Figures 6.3 and 6.4. At the suspected free shear layer, a sharp increase from approximately KE=0.25 to KE=1.5 occurs relative to the vortex edge below. This is presumably due to the vortical instabilities observed in the free shear layer by high speed imaging in Video 5.1. Finally from this elevated KE in the free shear layer, a decreasing gradient towards the quiescent fluid above is seen in Figures 6.3 and 6.4.

In contrast, the cases *with* beads show a single gradual gradient of KE increase from the bottom half, behind the plate, to the top half of the FOV. This corresponds to results from Table 5.1 and Figure 5.2, where it was found that fluids *with* beads tended to follow the plate motion in the lower half of the FOV. To better differentiate between the lower KE values in the results for fluids *with* beads, Figure 5.5 displays respective KE plots from Figure 5.3 (bottom row), but at a reduced range of KE. Figure 5.5 shows results at t*=0.46 (top row) and at t*=0.93 (bottom row). The two time points are shown to analyze the end of and a mid-point in the tow. The gradual gradient of velocity in the fluids *with* beads, as previously mentioned, is more obvious in Figure 5.5 at both t*=0.46 and t*=0.93. This suggests that a very weak shear layer exists. As a result it is speculated that the free shear layer is more diffuse *with* beads, relative to the distinct free shear layer observed in the fluid cases *without* beads. The free shear layer might become more evident if the FOV was larger.

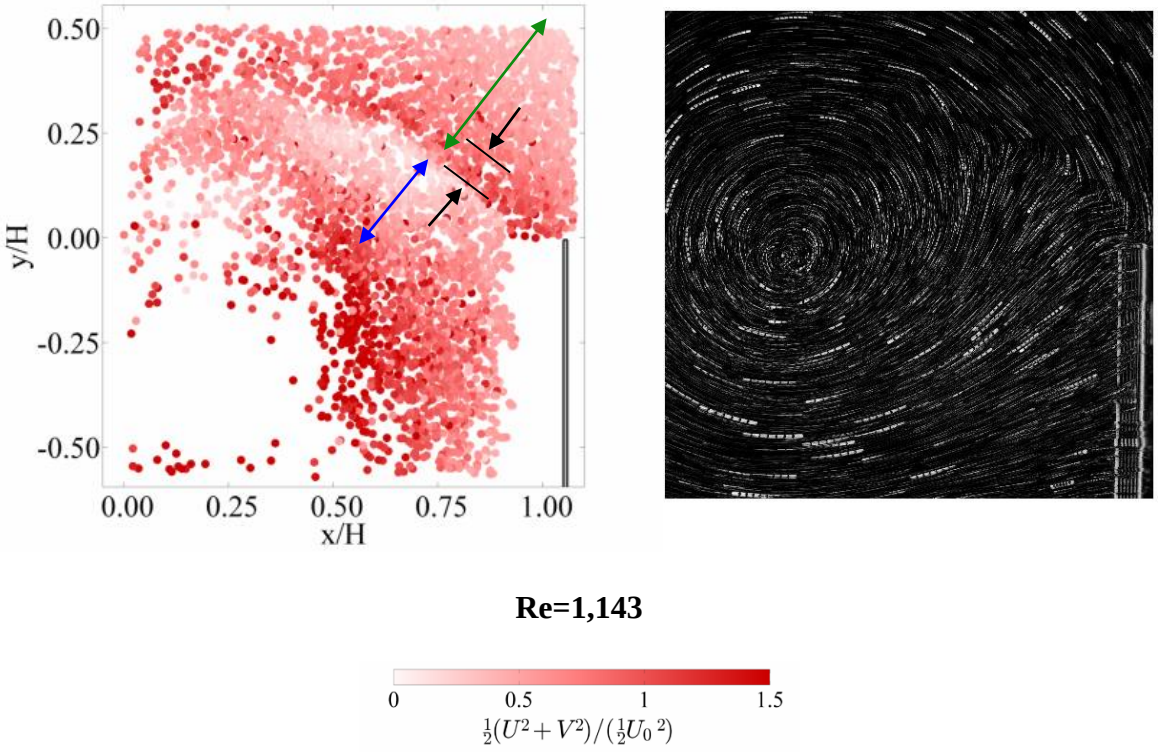

Figure 5.4: The Re=1,143 case *without* beads is expanded (left) from Figure 5.3 to show the prevailing gradients in kinetic energy (KE). The (**black**) arrows shows the elevated KE region at the free shear layer, the blue arrow denotes the KE gradient from a central region of the vortex to its edge, and the green arrow denotes the gradient from the free shear layer to the quiescent fluid above. Superimposed images are shown (right) at Re=1,143 from Figure 5.1, showing the expected velocity gradient shape between the quiescent fluid above and the starting vortex below the free shear layer. Images near the end of the tow were selected as there is less shadowing from the plate and more of the vortex is visible in the FOV.

In summary, the KE plots demonstrate the existence of a free shear layer prior to the addition of beads, as well as evidence of the starting vortex. A reduction in energy of approximately KE=1.5 to KE=0.75 results with the addition of beads, along with a more uniform distribution of KE over the FOV. The sharp gradients in KE as a result of the free shear layer and starting vortex were no longer obvious in the fluids *with* beads. Instead, a single relatively gradual gradient in KE is observed, suggesting a diffused free shear layer is present.

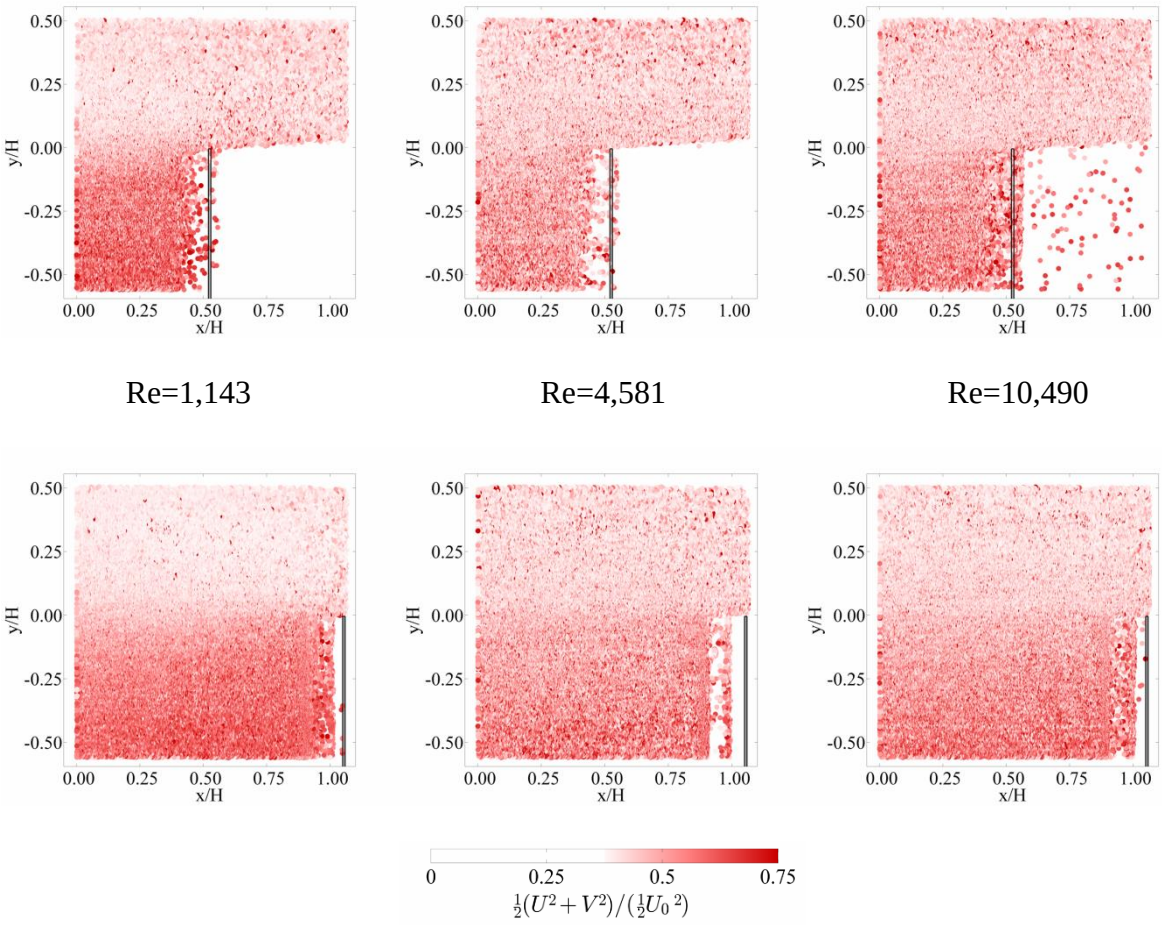

Figure 5.5: Kinetic energy (KE) of tracked particles for cases *with* beads, non-dimensionalized by freestream KE, where only particles with a KE *below* 0.75 are shown. Data is shown for Re=1,143, 4,581, and 10,490 at both t*=0.46 (top row) and t*=0.93 (bottom row). These time points were arbitrarily chosen to demonstrate fluid behaviour both part way through and near the completion of the tow. The plate extends from the bottom of the FOV until y/H=0, but is not shown in its entirety.

5.3 Increasing Reynolds Number and Particle Induced Delay of Transitional Behaviour

The results are further discussed as they pertain to particle induced modification of the developing free shear layer, but specifically as they relate to the differences with increasing Reynolds number.

5.3.1 Vortical Instabilities and Lagrangian Fluid Velocity

From Video 5.1, Re=10,490 had an increased frequency of small vortices in the free shear layer as compared to Re=4,581 and especially Re=1,143. The starting vortex core displacement through the run was 2-D and thus seemingly less stable than at Re=1,143, where motion was mostly 1-D and following the plate motion.

In Figure 5.2, the direction and patterns of the flow in all cases *without* beads appear similar. A recirculation in the fluids *without* beads (top row) following the plate motion is distinguishable by the directionality of pathlines plotted. However, the free shear layer and its associated vortical instabilities are not obvious, nor is the starting vortex in the Lagrangian velocity plots. The differentiating characteristics with increasing Reynolds number in Videos 6.1 and 6.2, were the frequency of vortical instabilities shed from the plate tip and the degree of stability, from observation, in the starting vortex core. Although, the high speed imaging was assessed for only a single run, these are only tentative conclusions. The Lagrangian velocity plots do not display the free shear layer, let alone the small-scale vortical instabilities within it. As a result, no apparent differences are identifiable when Reynolds number is increased in the fluids *without* beads from the Lagrangian plots.

After adding beads, the differences in fluid flow patterns and velocity in the suspensions drawn from the Lagrangian plots between Re=1,143, 4,581, and 10,490 were minimal. This was in part attributable to the increased effective viscosity from the particle-phase, resulting in an approximated maximum Reynolds number of Re_K=934 (Krieger, 1972). However, this was not sufficient to explain the contrast in results of a Reynolds number less than 20% lower with the

Re=1,143 fluid *without* beads (A), and thus it is speculated that the beads are acting to store and diffuse energy. The viscosity discrepancy is further discussed below.

5.3.2 Kinetic Energy and the Free Shear Layer

In Figure 5.3 there is little distinguishable change in KE as Reynolds number increases in the cases *with* beads, and the same is true for Figure 5.2 in terms of velocity and flow patterns, as previously discussed. The differences in findings amongst the cases *with* beads in the KE and Lagrangian plots are a matter of track density. This is likely due to refraction of the laser causing increased 3-D motion to be captured in the aqueous glycerol solutions. The lack of differentiating characteristics from the results is true for the KE results *without* beads as well, and therefore conclusions based on KE differences with increased Reynolds number cannot be drawn from the KE or Lagrangian velocity plots. However, from Video 5.1 an increase in vortical instabilities in the free shear layer and the center of the starting vortex were observable in the cases *without* beads as Reynolds number increased from Re=1,143 to 10,490. It is thus recognized that the KE plots are not able to resolve the small-scale vortical instabilities observed in the videos and consequently, effects due to increasing Reynolds number *with* beads at smaller scales cannot be discounted.

Chapter Six: **DISCUSSION**

The results presented in Chapter 5 will be discussed in reference to previous studies. Mechanisms by which the SAP beads modify the developing free shear layer will then be proposed.

The important results will be discussed in sections 6.1 to 6.3 in the following order: viscous effects, reduced velocities, and diffusion of flow features and energy storage. Section 6.4 then summarizes the experimental results as they relate to the two initial aims of this study. First the implication of the results to the contribution of RBCs on the development of transitional flow in the arterial system will be discussed, followed by how these results differ with increasing Reynolds number from 1,143 to 10,490. Then, the implications of these results on the assumptions made when modelling arterial blood flow in areas where transitional or turbulent flow can occur are outlined. This chapter concludes with Section 6.5, which presents the limitations and errors of this study.

6.1 Viscous Effects

It is well-established that the addition of a solid-phase to a fluid increases its overall viscosity (Stickel and Powell, 2005). However, past a volumetric concentration of ϕ=25%, Matas et al. (2003) found that delayed critical Reynolds number (Re_c) for transitional flow development was not just a factor of increased effective viscosity (Matas *et al.*, 2003). The increased viscosity caused by particles was not sufficient to explain the observed prolonged laminar flow (Matas et al., 2003).

Based on effective viscosity predictions using Krieger's formula, in the present study the Re=10,490, 4,581, and 1,143 cases would be reduced to Re_K=934, 194, and 91, respectively (Krieger, 1972; Matas et al. 2003; Stickel & Powell, 2005). Therefore, if altered fluid behaviour

was only a result of the increase in viscosity due to the suspension phase, water *with* beads (Re=934) should have similar flow behaviour to Glyc60 *without* beads (Re=1,143); see Appendix C for viscosity calculations.

Based on Table 5.1, despite Reynolds numbers within 20%, water *with* beads (Re=10,490 and Re_K=934) has a large discrepancy in the median values of U and V compared to the Re=1,143 case *without* beads (Glyc60). This suggests dissimilar flow patterns. This is supported by Figure 5.2 where an effective viscosity is not sufficient to explain the lack of flow features at Re=10,490 *with* beads (Re_K=934) as compared to Re=1,143 *without* beads, specifically a starting vortex and distinct free shear layer when particles are added. The suspension case (Re=10,490; Re_K=934) also has lower mean velocities than the fluid alone (Re=1,143); see Table 5.1. Lower mean velocities *with* beads, albeit a similar Reynolds number is also seen in the Lagrangian plots, further supporting that the particle-phase induces additional mechanisms apart from an increased effective viscosity; see Figure 5.2 (Matas et al., 2003).

Fluids at Re=1,143 *without* beads and Re=10,490 (Re_K=934) *with* beads show very different results in not only velocity and flow patterns, but in KE magnitude and distribution as well; see Figures 6.3 and 6.4. Kinetic energy plots support the differing flow patterns suspected from Table 5.1 and observed in Figure 5.1 and 6.2, as a free shear layer is present. A single diffuse KE gradient in the suspension case is observed as compared to the fluid alone, where a free shear layer with vortical instabilities and starting vortex were discernible; see Video 5.2. Therefore, the discrepancy in results between a single and two-phase fluid with very close Reynolds numbers (within 20%) supports findings by Matas et al. (2003), in that viscosity is not the sole determinant for prolonged laminar flow in dense suspensions above a 20% volumetric concentration of particles.

Curtis and van Wachem (2004) point out that studies not accounting for frictional stresses at the particle-scale in dense suspensions result in the stresses of the carrier-phase being underestimated in numerical models. Numerical models that underestimated stresses compared to flows in practice had higher fluid velocities and behaviour characteristic of a larger Reynolds number, described by Curtis and van Wachem (2004) as "water-like". This is similar to the present study in that the effective viscosity assumption for a suspension underestimated the resultant reduction in Reynolds number.

6.2 Reduced Velocities

In the present study, a reduction in velocity in the suspension cases relative to the carrier-phase alone was shown through numerical data and Lagrangian velocity plots; see Table 5.1 and Figure 5.2. Reduced mean velocity in the fluids *with* suspended SAP beads agrees with Kaftori et al. (1998), who found reduced mean velocities with suspended 900 μm particles at Re=4,581. However, Kaftori *et al.* (1998) considered a turbulent regime, dilute volumetric concentrations on the order of 0.01%, and used hard dense particles. The present work considers a developing transitional flow with a dense 50% volumetric concentration of elastic particles. Picano *et* al. (2014) attempted to address the deficiency in studies of dense particle-laden flows and found reduced mean and more uniform velocity in suspensions with particle volumetric concentrations of ϕ=20%. Both of these studies assumed a turbulent regime. Consequently, the mechanisms of turbulence modification can be very different to those that induced reduced velocity in the present study. However, together the studies demonstrate that reduced velocity by the addition of a particle-phase is associated with a reduction in turbulence, and therefore turbulence modification. Similarly, the present study shows a reduced velocity *with* added particles that is associated with

a diffusion of flow features, namely the free shear layer and starting vortex, delaying the formation of instabilities that can lead to transition or turbulent flow.

6.3 Diffusion of Flow Features and Energy Storage

Picano et al. (2014) found that streamwise flow structures were elongated in dense suspensions (ϕ=20%) when turbulence was attenuated, relative to single-phase flow. Picano et al. (2014) studied a turbulent regime; however, similar to the present study, a modification of flow structures is associated with modified turbulence. It is suggested from the results of the present study that the free shear layer observed *without* beads is largely diffused in the cases *with* beads, such that it extends out of the FOV. As a result of diffused flow features by the presence of beads, a delay in the development of turbulence is speculated, although not proven due to limitations in the experimental set-up for attaining high enough Reynolds numbers.

Furthermore, a reduction of KE was seen with the addition of beads relative to the fluids alone. As the increase in effective viscosity was not sufficient to explain the resultant behaviour, it is speculated that the additional energy losses are diffused and partly stored by the SAP beads. Dubief et al. (2013) and Zhao et al. (2013) have shown that elastic particles can extract energy from the flow by transforming fluid KE to particle elastic energy. These numerical simulations assumed low volumetric concentrations of long-chain polymers in fully-turbulent flow, in contrast to spherical particles and developing transitional flow of the current study. However, transformation of fluid KE to bead elastic energy cannot be discounted in the present findings, given the elasticity of SAP beads, and the proven ability of elastic particles of some form or another to absorb energy elastically (Zhao et al., 2013; Dubief et al., 2013).

Furthermore, Zhao et al. (2013) found that particles redistributed turbulent kinetic energy spatially, although in a turbulent regime unlike the present study. This supports the redistribution of KE observed with the addition of beads observed here, which resulted in a more uniform distribution of KE over the FOV. Furthermore, the free shear layer and areas of concentrated KE, are speculated to be diffused in the bead cases, due to the resultant gentle gradient of KE. The diffusion of flow features, specifically the free shear layer, delays the development of flow instabilities that can subsequently lead to transitional and turbulent behaviour. As a result, diffusion is a possible mechanism for the delay of developing transitional behaviour, or prolonged laminar flow, and therefore turbulence. The diffusion and elastic storage of fluid energy by particles agrees with past work by Picano et al. (2014), and Dubief et al. (2013) and Zhao et al. (2013), respectively.

In agreement with the velocity results and Lagrangian plots, there were no glaring differences in KE energy magnitudes or distributions between the suspension-cases, as Reynolds number was increased. This suggests that with increasing Reynolds number, the speculated diffusion of flow features and possibly energy storage by the beads is increasing, resulting in a larger discrepancy between fluid-only and suspension results.

6.4 Implications of Findings to Arterial Blood Flow

The results are discussed as they relate to RBC contribution to the development of transitional flow features *in vivo* through healthy and pathological arterial vasculature. The significance of the present study's findings to blood flow modelling is then presented.

6.4.1 Delayed Transitional Behaviour by Red Blood Cells in the Vasculature

Han *et* al.'s (2001) findings of prolonged laminar flow to Re=2,900 in porcine blood and speculations of this behaviour being due to RBC presence is supported by a delay of vortical instabilities with the addition of beads in this study. The addition of beads reduced fluid velocity and KE in half on the particle-scale, produced a more uniform distribution of KE magnitude, and prevented the formation of a free shear layer. Super absorbent polymer beads are analogous to RBCs by their elasticity, sphericity, and because the experimental model was scaled to conditions conceivable in the arterial environment using Reynolds number. Furthermore, this model used a concentration of particles near the healthy volumetric concentration of RBCs in blood. As a result, this study captures the particle-particle dynamics of a bulk suspension of particles, which is too computationally intensive to model numerically. Li *et al*. (2014) expanded on speculations by Walker *et al*. (2014) that polymers (xanthan gum) added to aqueous glycerol were the cause of prolonged laminar flow, by testing the solution in both pulsatile and post-stenotic flow. Pulsatility in the cardiovascular system increases instability due to resultant velocity and turbulent kinetic energy fluctuations, as well as the cyclical development and attenuation of vortices (Gülan *et al*., 2012). Li *et al.* (2014) found that prolonged laminar flow in the two-phase blood analog still occurred in both pulsatile and post-stenotic flow. The present work shows that on the particle-scale, vortical instabilities are delayed *with* particles present in the range of Reynolds number (Re=1,143 to 10,490) tested. Instabilities promote transitional flow development and thus, delaying their formation can act to prolong laminar flow. The present study's findings of diffused flow features and reduced KE at the particle-scale suggests that on a macroscopic scale, given similar conditions, the development of transitional behaviour can be delayed as a result.

6.4.2 Delayed Transitional Behaviour by Red Blood Cells with Increasing Reynolds Number

A broad range of Reynolds numbers occur through the arterial vasculature, from Re=600 in the abdominal aorta to upwards of Re=10,490 under pathological conditions at the heart valves (Stein & Sabbah, 1976; Kheradvar and Pedrizzetti, 2012). This model is undeniably a crude approximation to flow conditions that would arise at the heart valves since scaling is solely based on Reynolds number, which only describes the viscous-to-inertial forcing of the fluid. Consequently, relative length scales of the resultant flow are not proportional, namely the large-scale flow features that would be a result of the shear generator height (H). However, diffused flow features and the resultant delay of instabilities observed over a range of Reynolds numbers in the present study, suggests that RBCs have a continued and possibly increasing turbulence attenuating effect with increasing Reynolds numbers.

Blood flow through certain areas of the vasculature is known to recirculate and develop free shear layers, such as at heart valves, the carotid bifurcation, and the aortic arch (Kim *et al.*, 2011; Kheradvar & Pedrizzetti, 2012). The findings of the present study suggesting that RBCs delay the formation of transitional behaviour stresses the importance of a two-phase model for blood in areas of the vasculature where transitional and turbulent flow may exist. Not coincidentally, these are areas prone to atherosclerotic plaque formation (Ku, 1997; Mejia *et al.*, 2011; Kheradvar & Pedrizzetti, 2012). Walker *et al.* (2014) and Li *et al.* (2014) show that a Newtonian analog can over-predict, or predict earlier transition to turbulence than would be expected *in vivo* with blood. This work suggests that RBCs can delay transitional flow behaviour by diffusing flow features from which subsequent instabilities could otherwise form, eventually leading to transitional or even turbulent behaviour. Consequently, it is suggested that specifically the two-phase characteristic of blood, if not accounted for in transitional or turbulent regimes, can

result in an over-prediction of turbulence. This could lead to a false prediction of pathological conditions such as atherosclerosis, since transitional and turbulent flow behaviour are associated with its development. Or the rejection of a heart valve design could result from inaccurately modelled flow conditions indicating turbulent conditions where they might not exist *in vivo*. Turbulence increases energy losses and therefore work input required by the heart. As a result, if turbulence is over predicted, so can be the risk of cardiovascular diseases.

Furthermore, accurate modelling of blood flow is critical to designing and improving cardiac devices such as replacement heart valves, stents, pacemakers, and artificial hearts, especially where these devices may have an effect on flow behaviour, or promote flow instability. Mechanical heart valves tend to enhance turbulent behaviour and associated shear strain rates (Li *et al.*, 2011; Kheradvar & Pedrizzetti, 2012). Consequently, a large area of cardiovascular research aims to reduce RBC damage often associated with these replacement heart valves (Kheradvar & Pedrizzetti, 2012).

6.5 Limitations and Error

This study provides a rudimentary study of RBCs in blood. Many characteristics of the vascular system have been disregarded in an attempt to concentrate on the RBC-plasma interaction and provide a foundation for future work on the turbulence modification of RBCs. Here the limitations of the model and its results are presented.

6.5.1 RBCs and SAP Beads

RBCs are near-neutrally buoyant discoid particles that are highly deformable. SAP beads are near-neutrally buoyant, spherical, and some-what elastic, similar to RBCs. In order to use PTV

for flow visualization, the RBC model chosen in the experiments had to be optically matched to the surrounding fluid. Considering these constraints, SAP beads were a suitable model of RBCs.

RBC shape was also simplified and it is understood that the drag and Re_p would differ with an aspherical particle (Stone et al., 2002). This is in addition to differences in the packing fraction of, and stresses on the RBCs due to a discoid rather than spherical shape. The shape of RBCs and how this affects the delay of instability development requires furthers investigation. Furthermore, the high deformability of RBCs allows for more complex motion such as kayaking, tank treading and forming aggregations (rouleaux), which SAP beads cannot model. However, rouleaux and tank treading require low shear strain rates (Cordasco and Bagchi, 2013). Focusing specifically on arterial large vessel blood flow where high shear strain rates are dominant, aggregation would be limited to regions or parts of the cardiac cycle (likely deceleration) allowing for low enough shear strain rates.

Finally, by using elastic RBC analogs (although to a lesser degree than RBCs), the elastic properties of RBCs cannot be discounted nor confirmed as a mechanism of turbulence modification, since delay in the development of transitional flow behaviour was found. If SAP beads showed no modification in the present study, it could be shown that neither presence nor elastic properties cause turbulence modulation. However, the aim of this work was to first determine whether RBCs by their bulk presence delay developing transitional behaviour and to simply suggest a mechanism by which this is accomplished. The RBC analog in the present work provides a basic initial approximation to RBC properties. Red blood cell deformability is an important property of RBCs and requires further investigation in the context of turbulence modification.

6.5.2 Vascular Flow Environment

Several aspects of the arterial environment have been disregarded in an attempt to simplify the complex dynamics of particle-induced turbulence modification. Vessel compliance, a pressurized pipe flow environment, and the pulsatility of blood flow were disregarded in an attempt to focus on the issue of whether RBC presence alone has an effect on developing transitional flow behaviour. Steps were taken regardless in an attempt to mitigate the effects of these neglected characteristics in the model.

In the model, the measurement plane was centered in the spanwise direction to maximize distance from and minimize effects of the sidewalls. The FOV was also centered in the streamwise direction, to reduce effects from the laser-side and back walls. A pipe flow environment was not modelled. However, the perspective of this model is a very small region of blood flow, on the order of RBCs (6 μm), away from the effects of the vascular wall. In a large artery (Aorta Ø=2 cm), a region this small is assumed to have equal and opposite pressure from all but the flow direction. The aquarium is an open-channel environment, but the surface of the fluid was maintained as full as possible to mitigate surface effects and unequal pressure in the vertical plane at the FOV depth.

Finally, pulsatility and vessel compliance were neglected. Neglecting pulsatility disregards the acceleration and deceleration of the flow, which can affect the flow features and instabilities that form, as well as the shear strain rates and stresses. However, as turbulence modification by particles is in itself already an intensive and multifaceted problem, these aspects were not incorporated for simplification purposes.

6.5.3 Experimental Set-Up Limitations

Some limitations have already been described in the short-comings of the model as they pertain to blood flow. The following relates specifically to the experimental set-up and process.

First, it was necessary to prevent separation of the aqueous glycerol solutions as this tendency arose upon the addition of beads to the solution when left to adjust optically. Repeated mixing and testing for optical distortion using the calibration plate at the measurement plane was employed to mitigate poorly mixed solutions. The calibration plate was positioned once all equipment was fixed in place to ensure the camera was focused on the laser plane. The camera, aquarium, laser, and motor traverse were all mounted to a fixed rail system (Bosch-Rexroth, USA, Charlotte, NC). Fluid evaporation was an issue, possibly affecting the volumetric and glycerol solution concentrations and consistency of each fluid case over time. To prevent this, the aquarium was always covered when not in use and all runs were performed on the same day, one after another, for each test case. To prevent inconsistency in suspending fluids between cases *with* and *without* beads, bead tests were always performed using the same fluid, and subsequent to "no bead" cases. Half the volume of fluid was removed, and SAP beads were added to refill the remaining half.

There was inconsistency in bead expansion between the water and aqueous glycerol. SAP beads required expansion in water prior to immersion in the glycerol solutions, otherwise they did not attain the same shape, size, and consistency. The beads appeared optically matched, confirmed by a lack of distortion of the calibration plate image. Therefore, it is speculated that only the outer region of the bead absorbed aqueous glycerol, but the core regions contained a higher water-to-glycerol ratio than the surrounding aqueous glycerol. The refraction affected the results, as previously mentioned. However, given time and cost constraints and the difficulty of finding

optically matched particles, the SAP beads were employed. Finally to ensure that the fluids were seeded with appropriate amounts of tracer particles, an initial test was performed prior to data collection and loaded in DaVis to verify that the ratio of particles per pixel (ppp) was approximately 0.005 as per Cierpka et al. (2012).

Glyc30 (Re=4,581) data had the least number of tracked particles, and as a result was the limiting data set for maximizing the number of particles tracked. The maximum number of tracks possible, without reducing min TL below 6 in Glyc30 was 55,812 and 57,332, with and without beads, respectively. Therefore, the number of particles tracked for Glyc60 (Re=1,143) and water (Re=10,490) were adjusted accordingly by varying min TLs. As discussed in Chapter 4, a more stringent min TL is desired to increase particle tracking confidence.

6.5.4 Flow Conditions

As the title of this work suggests, the focus of this study was the turbulence modification properties of RBCs. However, this experiment was not performed at turbulent flow conditions and only transitional flow. It was established that a free shear layer and resultant vortical instabilities were present in the test cases *without* beads, and therefore a developing transitional regime can be claimed. Given the change in flow features once beads were added to each fluid-case, testing should have continued to find the higher Reynolds number at which these appeared in the suspension-cases. However, with the current experimental set-up there were limitations inhibiting an increase in the Reynolds number. Specifically, the plate could not be enlarged in order to prevent effects from the free surface, SAP beads do not come in a smaller diameter, and the speed of the plate could not be increased due to impeded function at higher velocities. Therefore, the range of the experiments was constrained to a maximum of Re=10,490. As a result, only speculations can made as to how RBCs might prevent the development of turbulence. Nonetheless,

transition precedes turbulence and a delay in the latter should delay the former as well. Furthermore, developing transitional flow is more applicable to blood flow as it is present in the vasculature and through the heart (Stein & Sabbah, 1976; Gülan et al., 2012; Falahatpisheh & Kheradvar, 2012; Kheradvar & Pedrizzetti, 2012; Li et al., 2012; Charonko et al., 2013). Turbulence in the cardiovascular system is minimal, more likely present under pathological conditions, and weak if present (Kheradvar & Pedrizzetti, 2012).

6.5.5 Error due to 3-D Motion and Laser Refraction

At Re=4,581 *with* beads, a greater number of short, high-velocity tracks appear in the upper half of the FOV in the Lagrangian plots, relative to both Re=1,143 and Re=10,490; see Figure 5.2. This is speculated to be due to greater refraction of the laser sheet and thus, thicker measurement plane causing 3-D motion of fluid to be tracked in both glycerol solutions. Upon the addition of beads, "streaks" of higher and lower intensity light were obvious at Re=1,143 (Glyc60) and 4,581 (Glyc30); see Appendix A. The irregular distribution of light intensity over the FOV indicates laser refraction, and suggests imperfect RI matching between the particle and fluid phases. Note that the laser is refracted most in the cases containing glycerol. Further evidence and analysis of the elevated laser refraction in aqueous glycerol, as well as the spurious tracks at Re=4,581 *with* beads is provided in Appendix A.

In Figures 6.2 and 6.3, the lower left corner at Re=10,490 *without* beads, presents sparser track coverage. It is speculated that this is due to a thinner laser sheet through water (Re=10,490) from less refraction of the laser sheet, relative to both aqueous glycerol solutions (Re=1,143 and 4,581). Consequently, in areas of increased fluctuating fluid motion, it is expected that flow patterns would be more 3-D and thus out-of-plane. In the same region there were scarcer tracks in Figure 5.2 at Re=10,490 and in Video 5.1, a less steady motion of the starting vortex core was

observed. A vortex or developing instability is likely to entrain more 3-D motion (Gui et al., 2010; Durbin & Pattersson-Reif, 2010; Zhang et al., 2013). The location of scarce data in the KE and Lagrangian plots for Re=10,490 *without* beads, correlates to the general area of the vortex center that at Re=10,490 appeared more chaotic than at lower Reynolds number; see Video 5.1. It is speculated that the increased instability in the vortex displacement is associated with instability in the spanwise fluid motion. Spanwise fluid motion would produce short track lengths, as it is normal to the streamwise motion, which is the orientation of the measurement plane. At Re=10,490 increased 3-D motion is expected since higher Reynolds number indicates a relative increase in the inertial to viscous forces, suggesting less stability in the flow. Further analysis of sparse tracking at Re=10,490 is provided in Appendix A.

Re=4,581 *without* beads, the velocity magnitudes are higher than the other Reynolds number cases, as seen by mean U_T and the medians of |U| and |V| in Table 5.1. This is speculated to be due to 3-D motion captured in this data set. The standard deviation (Std) of U_T for Re=4,581 data is within 5% of the other cases, therefore, a greater number of high velocity tracks relative to the other cases is not likely.

6.6 Summary

An experimental model was developed to provide a first order approximation of blood flow, which accounts for the two-phase nature of blood by modelling the suspension-phase. Many factors of the vascular flow environment have been neglected and thus the model provides a rudimentary, but appropriately scaled estimation by Reynolds number of the ensemble RBC-plasma interaction in developing transitional flow. As Antiga & Steinman (2009) point out, the assumptions made here are no more of a limitation than a Newtonian homogenous flow

assumption, which has been ubiquitously applied in blood flow modelling. Newtonian flows do not experience modified turbulence nor prolonged laminar flow behaviour, which has been observed in blood (Han et al., 2001). The use of a homogenous flow assumption for areas of the vasculature where transitional or turbulent is possible, can over-predict instability of the flow and the transition to turbulence. The findings of this study suggest that RBCs specifically act to delay the development of transitional flow behaviour. Consequently, an over-prediction of turbulent behaviour by a Newtonian assumption for blood is speculated to be specifically due to the neglected particle-phase. As a result, not accounting for RBCs in blood as a dense particle-phase in modelling can predict pathological flow conditions at lower Reynolds numbers than might be true physiologically. With the present computing power, modelling the complex dynamics of a mass of billions of RBCs is not possible, without even considering the added intricacies of a transitional or turbulent flow. The present model, albeit with some generous assumptions, is no more presumptuous than past work with the glaring omission of inter-particular and particle-plasma dynamics that are present in a dense, 45% volumetric concentration of suspended deformable, elastic particles.

Chapter Seven: **CONCLUSIONS AND RECOMMENDATIONS**

This chapter highlights significant conclusions that emerge from the experimental results previously presented. This is followed by future research recommendations.

7.1 Conclusions

This study used an approximation to blood, in an attempt to quantify the contribution of red blood cells (RBC) to developing transitional behaviour in arterial flow. This work is unique in its inclusion of both blood's particle-laden characteristic and dense *in vivo* volumetric concentration of RBCs. The effects of a dense suspension of near-neutrally buoyant elastic super absorbent polymer (SAP) beads, analogous to RBCs, on a developing free shear layer were quantified with an experimental model. The experiment was scaled by Reynolds number to represent a shearing environment in arterial flow. Specifically, a perturbation an order of magnitude greater than RBC size (6 microns) was modelled. The general finding with the suspension cases relative to fluids alone was a delayed development of vortical instabilities, due to a diffusion of flow features when the SAP beads were present. The specific conclusions drawn from the experimental results are:

1. In a free shear layer model, scaled by Reynolds number to represent the shearing environment in arterial flow, a 50% concentration by-volume suspension of near-neutrally buoyant elastic spherical particles (SAP beads) produced the following results relative to the fluids alone:
    i. Reduced average fluid velocity;
    ii. No distinguishable flow features, specifically no starting vortex or free shear layer;
    iii. Reduced maximum kinetic energy (KE);

iv. Modified distribution of KE, specifically reduced gradients of KE.

Together these findings suggest that SAP beads cause a diffusion of flow features that are on the order of ten times the particle diameter. These flow features may lead to subsequent instabilities which can develop into transitional or turbulent flow. Therefore, transition is delayed by the presence of SAP beads. This experiment is a simplistic model of blood. However, it encompasses the essential features of high volumetric concentration of RBCs, their elasticity and shape to a degree, and a conceivable arterial flow condition based on Reynolds number. As a result, it is speculated that RBCs suspended in flow act to diffuse flow features at the RBC-scale, that subsequently delay the formation of flow instabilities from which transitional or turbulent behaviour can develop. This agrees with previous speculations of RBCs contributing to the prolonged laminar flow behaviour observed in blood (Han et al., 2001; Li et al., 2014; Walker et al., 2014).

2. Increasing Reynolds number from 1,143 to 10,490 (obtained using fluid density) in a 50% by-volume suspension of near-neutrally buoyant elastic spherical particles (SAP beads) produced no significant differences in tracked fluid flow patterns, velocity magnitude, or KE magnitude and distribution. As a result, it is suggested that the presence of SAP beads delayed development of transitional behaviour by diffusion of its preceding flow features between Re=1,143 to 10,490. However, due to limitations of the experimental model, the critical Reynolds number for the onset of transition in the suspension cases could not be determined. This finding can be extended to the arterial flow environment by Reynolds number scaling to suggest that instability development is also delayed in higher Reynolds number areas of the arterial vasculature, such as at heart valves or obstructions to flow. This agrees with delayed transition with a two-phase blood analog in both stenosed and non-stenosed flow models by Li et al. (2014). However, the physical scaling of the

experiment is limited to modeling a shear generator one order of magnitude larger than the particle-phase. Since scaling by Reynolds number only accounts for the inertial to viscous forcing in the fluid, this model is only a basic approximation of the flow conditions imposed at higher Reynolds numbers in arterial blood flow. This is since the length scales of resultant flow features are dependent on the geometry of the flow environment.

3. In a dense suspension (ϕ=50%) of elastic particles an increased effective viscosity due to the particle-phase, based on particle concentration and the maximum packing factor, is not sufficient to describe the apparent reduction in Reynolds number. The suspension case in water with Re=934 based on effective viscosity, had flow velocities and KE approximately half that of the Re=1,143 fluid *without* beads (Krieger, 1972; Matas et al, 2003). Furthermore, the suspension at Re=934 had a reduced KE gradient where the fluid alone (Re=1,143) produced a free shear layer and starting vortex. As a result, it is speculated that additional mechanisms, as a result of the particle phase, are contributing to the delayed development of vortical instabilities. Dubief et al. (2013) and Zhao et al. (2013) found that particles suspended in flow absorbed fluid energy as elastic energy. Therefore, it is speculated that a mechanism for delayed transition by the particle-phase is elastic storage of fluid energy, in addition to the diffusion of kinetic energy previously speculated.

7.2 Recommendations

This study serves as a basis for understanding the effects of RBC presence to the generation of instabilities and developing transitional behaviour in arterial blood flow. Delayed transitional behaviour was observed and therefore turbulence is delayed as well. A study of turbulence modification seems to imply that the implications of RBCs in fully developed turbulent flow, rather than a transitional regime, are being studied. However, turbulent behaviour is modified when it is delayed. This is more applicable to blood flow, given the limited presence of turbulent flow relative

to transitional behaviour (Kheradvar & Pedrizzetti, 2012). It would be useful to learn the effects of a dense suspension of RBC analogs in a turbulent flow regime. This could prove useful to applications requiring models of blood flow through known areas of turbulence in the vasculature, such as in the design of mechanical heart valves.

Additionally, it would be beneficial to learn the extent to which particles delay turbulence by increasing Reynolds number in a suspension until development of transitional behaviour occurred. Learning the critical Reynolds number to transition in the suspension phase could help quantify the additional mechanisms acting to delay transition in the flow. Furthermore, to enable quantification of the delay and to better understand the conditions for mitigating transition, it would be useful to explore the mechanisms proposed in this study, by which the dense particle phase diffused developing flow features. Quantification of interstitial fluid shearing and stresses could help in determining whether there is increased friction at the bead surface. Also, separately tracking the particle and fluid phases to discern any relative motion or particle collisions, could help to determine whether these dynamics bear any associated energy losses.

Finally, it is recognized that the RBC analog properties, namely their elasticity, in this study are only an approximation to the high deformability of RBCs. It would be useful to discern the effects of the particle-phase elastic properties, if any, on the delay in instability development from the present study. A comparison of results between hard and elastic particles could shed light specifically on the contribution of RBC material properties to prolonged laminar flow in blood.

References

Angelini, T. E., Dunn, A. C., Urueña, J. M., Dickrell, D. J., Burris, D. L., & Sawyer, W. G. (2012). Cell friction. *Faraday Discussions*, *156*(0), 31–39.

Antiga, L., & Steinman, D. A. (2009). Rethinking turbulence in blood. *Biorheology*, *46*(2), 77–81.

Barbee, K. A. (2002). Role of Subcellular Shear–Stress Distributions in Endothelial Cell Mechanotransduction. *Annals of Biomedical Engineering*, *30*(4), 472–482.

Baskurt, O. K., & Meiselman, H. J. (2008). RBC Aggregation: More Important than RBC Adhesion to Endothelial Cells as a Determinant of In Vivo Blood Flow in Health and Disease. *Microcirculation*, *15*(7), 585–590.

Basu, A. (2012). *Shear deformation in polymer gels and dense colloidal suspensions* (Ph.D.). University of Pennsylvania, United States -- Pennsylvania.

Bellani, G., Nole, M. A., & Variano, E. A. (2013). Turbulence modulation by large ellipsoidal particles: concentration effects. *Acta Mechanica*, *224*(10), 2291–2299.

Boon, B. (2009). Leonardo da Vinci on atherosclerosis and the function of the sinuses of Valsalva. *Netherlands Heart Journal*, *17*(12), 496–499.

Burton, T. M., & Eaton, J. K. (2005). Fully resolved simulations of particle-turbulence interaction. *Journal of Fluid Mechanics*, *545*, 67–111.

Campo-Deaño, L., Dullens, R. P. A., Aarts, D. G. A. L., Pinho, F. T., & Oliveira, M. S. N. (2013). Viscoelasticity of blood and viscoelastic blood analogues for use in polydymethylsiloxane in vitro models of the circulatory system. *Biomicrofluidics*, *7*(3), 034102.

Chapman, G. T., & Tobak, M. (1985). Observations, Theoretical Ideas, and Modeling of Turbulent Flows - Past, Present and Future. In *Theoretical Approaches to Turbulence* (pp. 19–49). New York: Springer-Verlag.

Charonko, J. J., Kumar, R., Stewart, K., Little, W. C., & Vlachos, P. P. (2013). Vortices Formed on the Mitral Valve Tips Aid Normal Left Ventricular Filling. *Annals of Biomedical Engineering*, *41*(5), 1049–1061.

Choi, J., Kwon, O., & Lee, C. (2011). Inter-particle collision in particle-laden isotropic turbulence. *Journal of Physics: Conference Series*, *318*(5), 052012.

Cierpka, C., Lütke, B., & Kähler, C. J. (2013). Higher order multi-frame particle tracking velocimetry. *Experiments in Fluids*, *54*(5), 1–12.

Cokelet, G. R., & Goldsmith, H. L. (1991). Decreased hydrodynamic resistance in the two-phase flow of blood through small vertical tubes at low flow rates. *Circulation Research*, *68*(1), 1–17.

Cordasco, D., & Bagchi, P. (2013). Orbital drift of capsules and red blood cells in shear flow. *Physics of Fluids (1994-Present)*, *25*(9), 091902.

Cristini, V., & Kassab, G. S. (2005). Computer Modeling of Red Blood Cell Rheology in the Microcirculation: A Brief Overview. *Annals of Biomedical Engineering*, *33*(12), 1724–1727.

Crowe, C. T. (2000). On models for turbulence modulation in fluid–particle flows. *International Journal of Multiphase Flow*, *26*(5), 719–727.

Curtis, J. S., & van Wachem, B. (2004). Modeling particle-laden flows: A research outlook. *AIChE Journal*, *50*(11), 2638–2645.

Davies, P. F., Remuzzi, A., Gordon, E. J., Dewey, C. F., & Gimbrone, M. A. (1986). Turbulent fluid shear stress induces vascular endothelial cell turnover in vitro. *Proceedings of the National Academy of Sciences*, *83*(7), 2114–2117.

Drochon, A., Barthes-Biesel, D., Lacombe, C., & Lelievre, J. C. (1990). Determination of the red blood cell apparent membrane elastic modulus from viscometric measurements. *Journal of Biomechanical Engineering*, *112*(3), 241–249.

Dubief, Y., Terrapon, V. E., & Soria, J. (2013). On the mechanism of elasto-inertial turbulence. *arXiv:1301.3952 [physics]*.

Dubief, Y., White, C. M., Terrapon, V. E., Shaqfeh, E. S. G., Moin, P., & Lele, S. K. (2004). On the coherent drag-reducing and turbulence-enhancing behaviour of polymers in wall flows. *Journal of Fluid Mechanics*, *514*, 271–280.

Durbin, Paul, & Pattersson-Reif, B. A. (2010). *Statistical Theory and Modeling for Turbulent Flow (2nd Edition)* (2nd ed.). John Wiley & Sons, Inc.

Elgobashi, S. (1994). On Predicting Particle-Laden Turbulent Flows. *Applied Scientific Research*, *52*(4), 309–329.

Evans, P. C., & Kwak, B. R. (2013). Biomechanical factors in cardiovascular disease. *Cardiovascular Research*, *99*(2), 229–231.

Falahatpisheh, A., & Kheradvar, A. (2012). High-speed particle image velocimetry to assess cardiac fluid dynamics in vitro: From performance to validation. *European Journal of Mechanics - B/Fluids*, *35*, 2–8.

Fedosov, D. A., Caswell, B., Popel, A. S., & Karniadakis, G. E. (2010). Blood Flow and Cell-Free Layer in Microvessels. *Microcirculation*, *17*(8), 615–628.

Gao, T., & Hu, H. H. (2009). Deformation of elastic particles in viscous shear flow. *Journal of Computational Physics*, *228*(6), 2132–2151.

Gidaspow, D., & Huang, J. (2009). Kinetic Theory Based Model for Blood Flow and its Viscosity. *Annals of Biomedical Engineering*, *37*(8), 1534–1545

Grover, W. H., Bryan, A. K., Diez-Silva, M., Suresh, S., Higgins, J. M., & Manalis, S. R. (2011). Measuring single-cell density. *Proceedings of the National Academy of Sciences*, *108*(27), 10992–10996.

Grzegorzewski, B., Kempczyński, A., & Bosek, M. (2009). Particle image velocimetry in the study of red blood cell sedimentation (Vol. 7388, pp. 738817–738817–6).

Gui, N., Fan, J., & Chen, S. (2010). Numerical study of particle-vortex interaction and turbulence modulation in swirling jets. *Physical Review E*, *82*(5), 056323.

Gülan, U., Lüthi, B., Holzner, M., Liberzon, A., Tsinober, A., & Kinzelbach, W. (2012). Experimental study of aortic flow in the ascending aorta via Particle Tracking Velocimetry. *Experiments in Fluids*, *53*(5), 1469–1485.

Han, S.-I., Marseille, O., Gehlen, C., & Blümich, B. (2001). Rheology of Blood by NMR. *Journal of Magnetic Resonance*, *152*(1), 87–94.

Herbertson, L. H., Deutsch, S., & Manning, K. B. (2011). Near Valve Flows and Potential Blood Damage During Closure of a Bileaflet Mechanical Heart Valve. *Journal of Biomechanical Engineering*, *133*(9), 094507–094507.

Hosseini, S. M., & Feng, J. J. (2012). How Malaria Parasites Reduce the Deformability of Infected Red Blood Cells. *Biophysical Journal*, *103*(1), 1–10. doi:10.1016/j.bpj.2012.05.026

Irgens, F. (2008). Viscoelasticity. In *Continuum Mechanics* (pp. 361–432). Springer Berlin Heidelberg.

Kaftori, D., Hetsroni, G., & Banerjee, S. (1998). The effect of particles on wall turbulence. *International Journal of Multiphase Flow*, *24*(3), 359–386.

Kaminsky, R., Kallweit, S., Rossi, M., Morbiducci, U., Scalise, L., Verdonck, P., & Tomasini, E. P. (2008). PIV Measurements of Flows in Artificial Heart Valves. In *Particle Image Velocimetry* (pp. 55–72). Springer Berlin Heidelberg.

Katritsis, D., Kaiktsis, L., Chaniotis, A., Pantos, J., Efstathopoulos, E. P., & Marmarelis, V. (2007). Wall Shear Stress: Theoretical Considerations and Methods of Measurement. *Progress in Cardiovascular Diseases*, *49*(5), 307–329.

Kheradvar, A., & Pedrizzetti, G. (2012). *Vortex Formation in the Cardiovascular System*. Springer.

Kim, H., Lu, J., & Chandran, K. B. (2011). Native Human and Bioprosthetic Heart Valve Dynamics. In K. B. Chandran, H. S. Udaykumar, & J. M. Reinhardt (Eds.), *Image-Based Computational Modeling of the Human Circulatory and Pulmonary Systems* (pp. 403–435). Springer US.

Krieger, I. M. (1972). Rheology of monodisperse latices. *Advances in Colloid and Interface Science*, *3*(2), 111–136.

Kumaran, V. (2010). Fundamentals of Rheology. In J. M. Krishnan, A. P. Deshpande, & P. B. S. Kumar (Eds.), *Rheology of Complex Fluids* (pp. 35–65). Springer New York.

Lian, Q.-X., & Huang, Z. (1989). Starting flow and structures of the starting vortex behind bluff bodies with sharp edges. *Experiments in Fluids*, *8*(1-2), 95–103.

Li, C.-P., Chen, S.-F., Lo, C.-W., & Lu, P.-C. (2011). Turbulence Characteristics Downstream of a New Trileaflet Mechanical Heart Valve. [Miscellaneous Article]. *Journal May*, *57*(3), 188–196.

Lubliner, J., & Papadopoulos, P. (2014). Elasticity. In *Introduction to Solid Mechanics* (pp. 241–311). Springer New York.

Lucci, F., Ferrante, A., & Elghobashi, S. (2010). Modulation of isotropic turbulence by particles of Taylor length-scale size. *Journal of Fluid Mechanics*, *650*, 5–55.

Mansour, M. H., Bressloff, N. W., & Shearman, C. P. (2010). Red blood cell migration in microvessels. *Biorheology*, *47*(1), 73–93.

Matas, J.-P., Morris, J. F., & Guazzelli, E. (2003). Transition to turbulence in particulate pipe flow. *Physical Review Letters*, *90*(1).

McDonough, J.M. (2007). *Introductory Lectures on Turbulence: Physics, Mathematics and Modeling* (2nd ed.). Departments of Mechanical and Mathematical Engineering: University of Kentucky.

Nag, S. K., & Jana, R. N. (1981). Oscillating two-phase flow in an elastic tube. *Acta Mechanica*, *41*(1-2), 121–128.

Nerem, R. M., & Seed, W. A. (1972). An in vivo study of aortic flow disturbances. *Cardiovascular Research*, *6*(1), 1–14.

Parthasarathy, R. N., & Faeth, G. M. (1990). Turbulence modulation in homogeneous dilute particle-laden flows. *Journal of Fluid Mechanics*, *220*, 485–514.

Poelma, C., & Ooms, G. (2006). Particle-Turbulence Interaction in a Homogeneous, Isotropic Turbulent Suspension. *Applied Mechanics Reviews*, *59*(2), 78–90.

Preedy, V. R., & Watson, R. R. (Eds.). (2010). Erythrocyte Sedimentation Rate. In *Handbook of Disease Burdens and Quality of Life Measures* (pp. 4204–4204). Springer New York.

Pries, A. R., Ley, K., & Gaehtgens, P. (1986). Generalization of the Fahraeus principle for microvessel networks. *American Journal of Physiology - Heart and Circulatory Physiology*, *251*(6), H1324–H1332.

Procaccia, I., L'Vov, V. S., & Benzi, R. (2008). Colloquium: Theory of drag reduction by polymers in wall-bounded turbulence. *Reviews of Modern Physics*, *80*, 225–247.

Rauleder, J., & Leishman, J. G. (2014). Particle–fluid interactions in rotor-generated vortex flows. *Experiments in Fluids*, *55*(3), 1–15.

Roberts, Philip J. W., & Webster, Donald R. (2002). Turbulent Diffusion. In Shen, Hayley H. (Ed.), *Environmental fluid mechanics : theories and applications* (p. 467). American Society of Civil Engineers.

Roy, A., Morozov, A., van Saarloos, W., & Larson, R. G. (2006). Mechanism of polymer drag reduction using a low-dimensional model. *Physical Review Letters*, *97*(23), 234501.

Samanta, D., Dubief, Y., Holzner, M., Schäfer, C., Morozov, A. N., Wagner, C., & Hof, B. (2013). Elasto-inertial turbulence. *Proceedings of the National Academy of Sciences*, *110*(26), 10557–10562.

Schwarzkopf, J. D., Crowe, C. T., & Dutta, P. (2009). A turbulence dissipation model for particle laden flow. *AIChE Journal*, *55*(6), 1416–1425.

Secomb, T. W., Styp-Rekowska, B., & Pries, A. R. (2007). Two-Dimensional Simulation of Red Blood Cell Deformation and Lateral Migration in Microvessels. *Annals of Biomedical Engineering*, *35*(5), 755–765.

Segur, J. B., & Oberstar, H. E. (1951). Viscosity of Glycerol and Its Aqueous Solutions. *Industrial & Engineering Chemistry*, *43*(9), 2117–2120.

Snabre, P., & Mills, P. (1999). Rheology of concentrated suspensions of viscoelastic particles. *Colloids and Surfaces A: Physicochemical and Engineering Aspects*, *152*(1–2), 79–88.

Sreenivasan, K. R., & White, C. M. (2000). The onset of drag reduction by dilute polymer additives, and the maximum drag reduction asymptote. *Journal of Fluid Mechanics*, *409*, 149–164.

Srivastava, P. D. V. P., & Saxena, M. (1995). A two-fluid model of non-Newtonian blood flow induced by peristaltic waves. *Rheologica Acta*, *34*(4), 406–414.

Srivastava, V. P., & Srivastava, R. (2009). Particulate suspension blood flow through a narrow catheterized artery. *Computers & Mathematics with Applications*, *58*(2), 227–238.

Steinman, D. A. (2012). Assumptions in modelling of large artery hemodynamics. In D. Ambrosi, A. Quarteroni, & G. Rozza (Eds.), *Modeling of Physiological Flows* (pp. 1–18). Springer Milan.

Stein, P. D., & Sabbah, H. N. (1976). Turbulent blood flow in the ascending aorta of humans with normal and diseased aortic valves. *Circulation Research*, *39*(1), 58–65.

Stickel, J. J., & Powell, R. L. (2005). Fluid Mechanics and Rheology of Dense Suspensions. *Annual Review of Fluid Mechanics*, *37*(1), 129–149.

Sugii, Y., Okuda, R., Okamoto, K., & Madarame, H. (2005). Velocity measurement of both red blood cells and plasma of in vitro blood flow using high-speed micro PIV technique. *Measurement Science and Technology*, *16*(5), 1126.

Tanaka, T., & Eaton, J. K. (2008). Classification of Turbulence Modification by Dispersed Spheres Using a Novel Dimensionless Number. *Physical Review Letters*, *101*(11), 114502.

Thiriet, M. (2007). Biochemical and Biomechanical Aspects of Blood Flow. In F. Mollica, L. Preziosi, & K. R. Rajagopal (Eds.), *Modeling of Biological Materials* (pp. 33–100). Birkhäuser Boston.

Walker, A. M., Johnston, C. R., & Rival, D. E. (2014). On the Characterization of a Non-Newtonian Blood Analog and Its Response to Pulsatile Flow Downstream of a Simplified Stenosis. *Annals of Biomedical Engineering*, *42*(1), 97–109.

White, C. M., & Mungal, M. G. (2008). Mechanics and Prediction of Turbulent Drag Reduction with Polymer Additives. *Annual Review of Fluid Mechanics*, *40*(1), 235–256.

Windberger, U., Bartholovitsch, A., Plasenzotti, R., Korak, K. J., & Heinze, G. (2003). Whole blood viscosity, plasma viscosity and erythrocyte aggregation in nine mammalian species: reference values and comparison of data. *Experimental Physiology*, *88*(3), 431–440.

APPENDIX A: PARTICLE TRACKING INCONSISTENCIES AND 3-D MOTION

Further evidence of and a discussion of the error associated with inconsistent particle tracking that was presented in Chapter 5 is provided in this section. First, the evidence for the speculated 3-D motion *not* captured in the results and therefore causing less tracks plotted for Re=10,490 *without* beads are discussed. This is followed by support for the speculation of laser refraction increasing when beads are added to aqueous glycerol as compared to water, resulting in *more* out-of-plane motion being captured in the data.

A.1. 3-D Out-of-Plane Motion Without Beads

Compared to both Re 1,143 and 4,581 *without* beads, Re 10,490 has the least track coverage in the lower left corner of the FOV ($x/H < 0.4$; $y/H < 0$); see Figure 5.2. Re=1,143 as compared to Re=4,581, also has sparser tracks in this region. Note that this is an area of higher velocity and consequently, reduced tracks here could skew the resultant average tracked velocity and TKE to appear artificially lower. A less stringent min TL for the water case improves this but increases the number of particle tracks, which must remain consistent between cases.

To verify that the time-distribution of tracked particles was consistent, the number of particles tracked per frame from all runs (no beads = 20; with beads = 100) are shown in Figure A.1. Approximately 4,581 more particles were tracked at Re 10,490 early in the tow (frames 10 to 20), compared to both aqueous glycerol cases *without* beads; see Figure A.1. Otherwise, between all cases *with* beads a similar trend consisting of a peak number of particles tracked earlier on and followed by a decrease to a steady value of approximately 4,000 particles near the end of the tow.

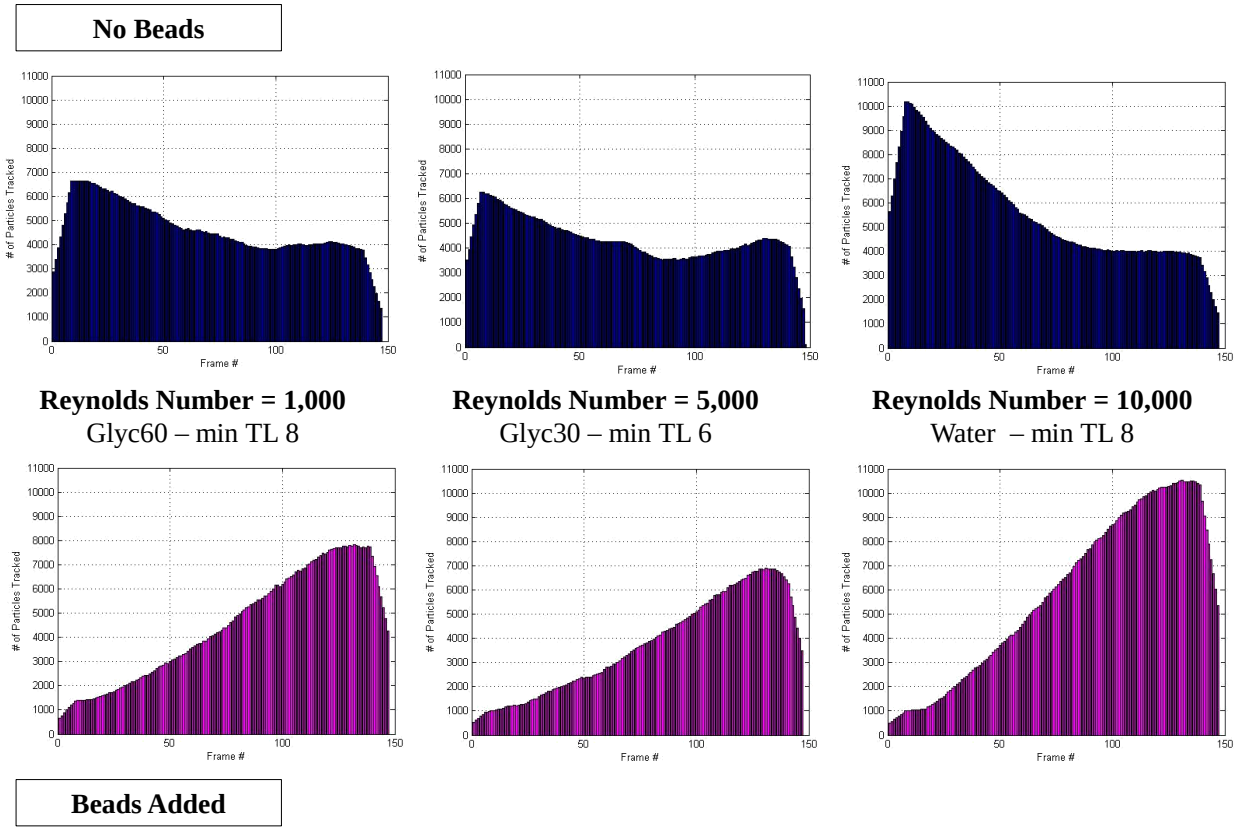

Figure A.1: The number of particles tracked per frame plotted throughout the plate tow in Glyc60, Glyc30, and water *without* beads (top row) representing Reynolds numbers (Re) of 1,143, 4,581, and 10,490, respectively. The same is shown for cases *with* the addition of beads (bottom row). Results presented are using all data collected and constrained with minimum track lengths (min TL) as per Table 4.3.

Figure A.2 reflects the density of particles tracked through the whole time-length of a tow, but with respect to the FOV area. Of note is that between the three cases *without* beads (top row), the distribution of the number of particles tracked is not vastly different. In particular, in the lower left corner of Re=10,490, where less tracks were plotted in Figure 5.2, there is an elevated density of particles tracked. However, Figure 5.2 was constrained with min TLs whereas Figure A.2 is not. It is speculated that increased 3-D motion at Re=10,490 *without* beads, which resulted in more out-

of-plane motion and shorter track lengths, is the reason for less tracks plotted for this case in Figure 5.2. Furthermore, reducing the min TL constraint in Lagrangian plots improved the amount of tracks in Figure 5.2 in the lower left corner.

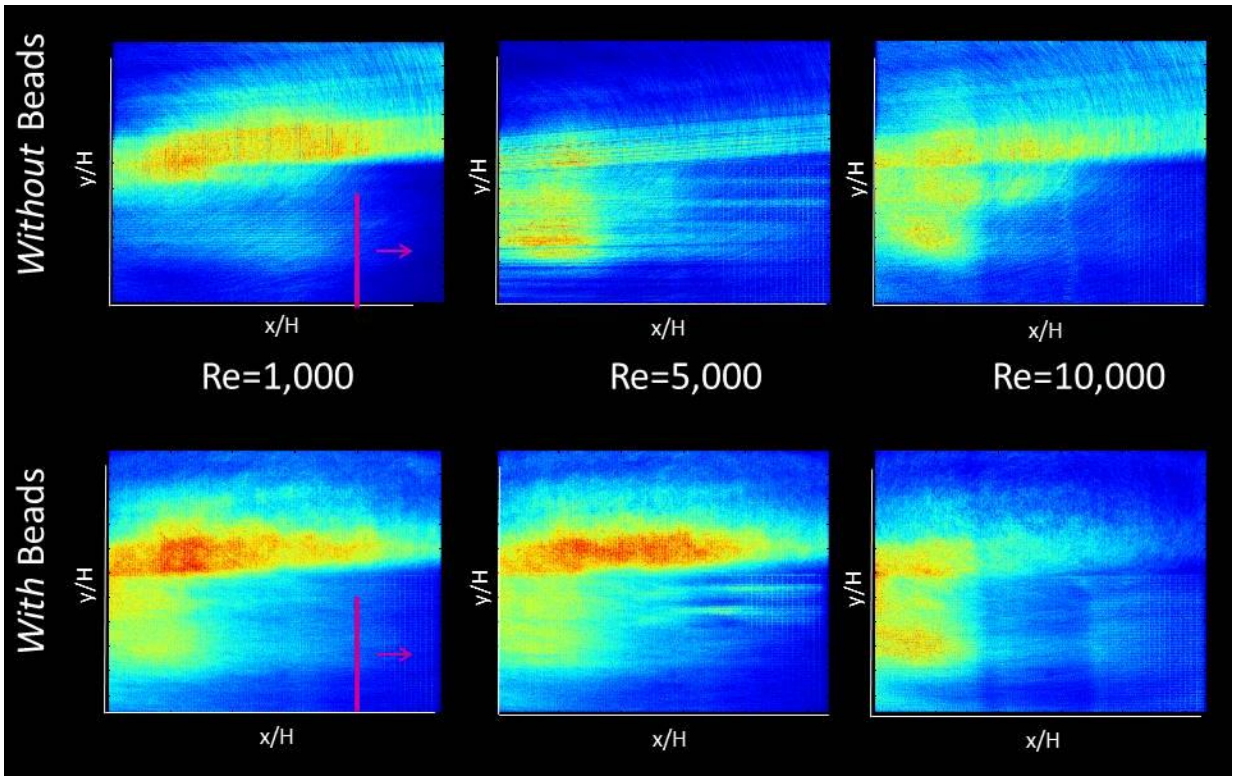

Figure A.2: Density distribution of the total amount of particles tracked over the total length of the plate tow, for all the runs combined (no beads=20; with beads=100) and plotted over the FOV. Blue indicates lower densities and Red indicates the highest. No minimum track length constraint was applied. The approximate location of the plate and tow direction are shown for reference, noting that this plot shows results from the entire recording time, thus from all frames, and not just at the time-point where the plate is shown.

A.2. Laser Refraction with SAP Beads

Out-of-plane motion is suspected to be a factor for the reduced tracking in this lower left corner of the FOV as seen in Figure 5.2 at Re=10,490 *without* beads. Fluids *with* beads refracted the laser sheet, as shown in Figure A.2 for the 30% by weight aqueous glycerol case (Re=4,581). However, refraction in water was the least prominent and thus the laser sheet thickness at the FOV

was closest to the specified 1.5 mm. Out-of-plane motion, or particles travelling normal to the measurement plane, would not be captured as readily with a thin as compared to a thick laser sheet. Figure A.3 shows the laser refraction and associated increasing measurement plane thickness through the length of the aquarium.

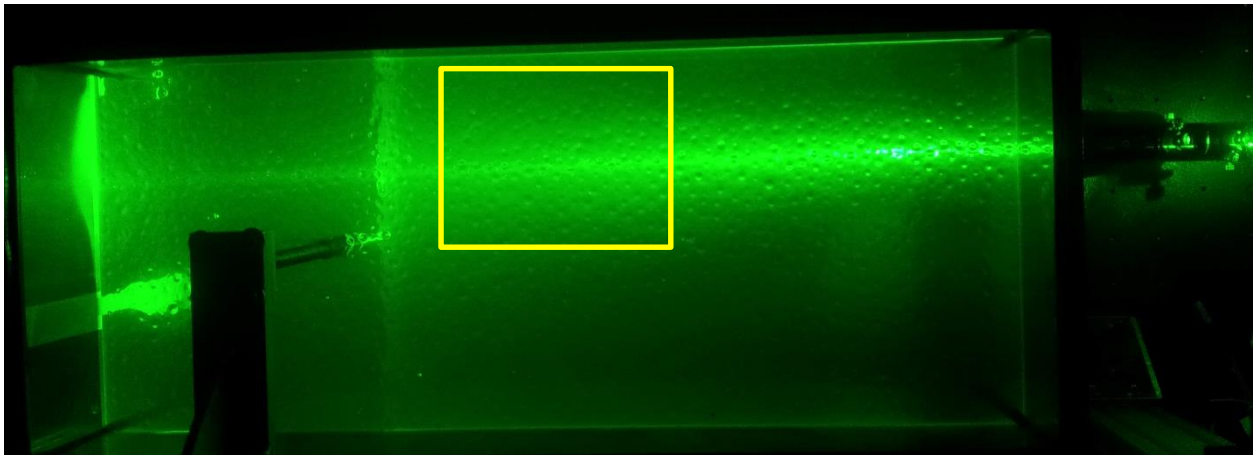

Figure A.3: PTV laser (top view) propagating and refracting through the length of the aquarium, filled with 30% by weight aqueous glycerol and containing suspended, near-neutrally buoyant, SAP beads. The approximate location of the measurement location where the camera was focused on the laser plane is denoted by the yellow box.

At Re 4,581, shorter length tracks of high velocity are apparent in Figure 5.2, but few exist at Re=10,490. A more stringent constraint on minimum track length (min TL) of 10 reduced these high velocity tracks, indicating that they are shorter.

Furthermore, both glycerol solutions *with* beads display unevenly distributed intensity of light over the FOV that manifests as "streaks" of more and less concentrated light; see Figure A.4. The streaks appear to be due to refraction of the laser by the beads, more evident in the glycerol solutions, since this effect is not as prominent in the case with water as a suspending fluid. The refraction reduces the two-dimensionality of the measurement, because the laser sheet is thicker; see Figure A.2. The streaks were visible at the time of testing and they became less prominent

with time, but were never completely reduced; see Figure 5.2. Consequently, testing was performed regardless of the streak presence. From Figure A.4, the streaking is more prominent at Re=4,581, where in Figure 5.2 the greatest amount of short high velocity tracks are obvious relative to the cases *with* beads. Therefore, the short high velocity tracks that present at Re=4,581 and 1,143 are suspected to be a result of 3-D motion captured in the raw images. The refraction seen in Figure 5.2 and the resultant thickened laser sheet shown in Figure A.2, along with the increased prominence of short high velocity tracks in Glyc30 together support that 3-D motion was captured in the results.

The outlines of the beads are more visible in aqueous glycerol than in water because the brightness was increased in order to capture the tracer particles present in the streaks of lower light intensity; see Figure A.4. The increased refraction upon adding SAP beads in aqueous glycerol signals a difference in refractive properties between the beads and surrounding fluid, since no streaks are evident in Figure 5.1 in the glycerol solutions (top row) prior to the addition of beads. A closer refractive index (RI) match between the fluid and beads produces less refraction of the laser. The RI matching between the SAP beads and aqueous glycerol is therefore not as close as the SAP beads and water. The SAP beads necessitated expansion in water first, and then immersion in each glycerol solution, otherwise they did not expand to a spherical shape and only to about half the diameter (0.5 cm). As a result, the composition of the beads suspended in the glycerol solutions is likely not as close of a match to the fluid-phase when it is Glyc30 or Glyc60, as compared to water. Refractive index discrepancy is believed to be the cause of increased refraction of the laser in cases *with* beads when beads are immersed in solutions of glycerol (Re 1,143 and 4,581).

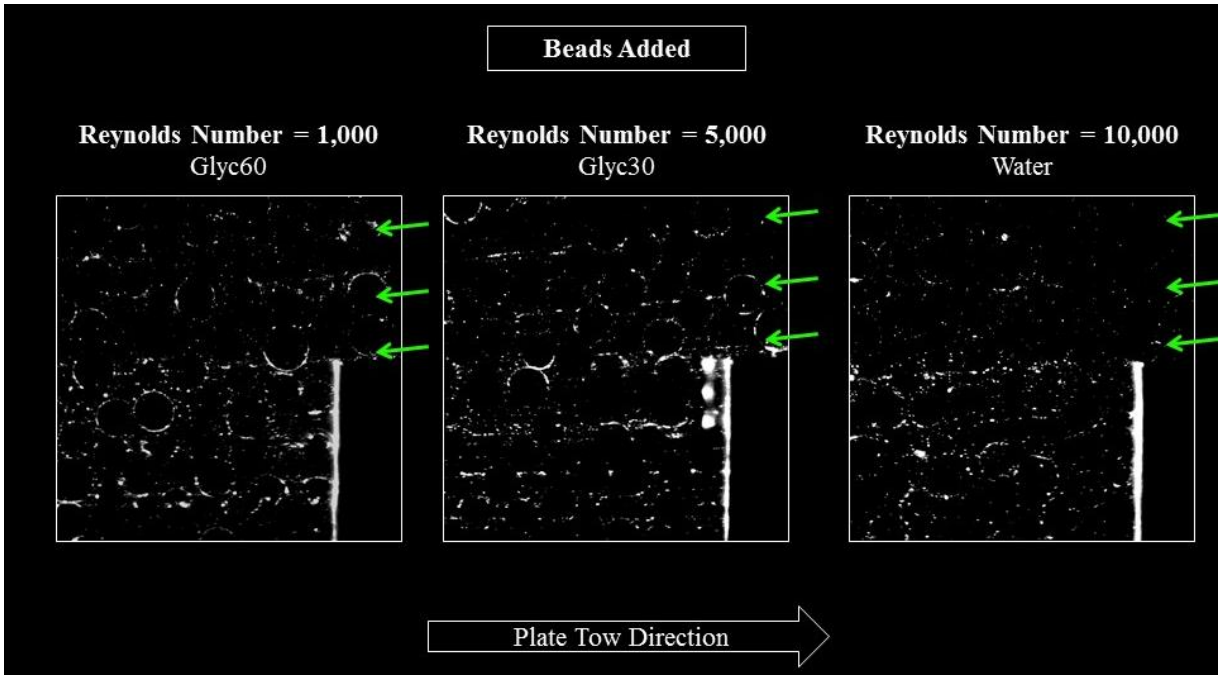

Figure A.4: Raw images (frame 116/150) for the cases *with* beads. The green arrows denote the locations of higher intensity "streaks" that are most obvious at Re=4,581 and apparent at Re=1,143, where both suspending fluids are solutions of glycerol. Note that this effect is not as prominent at Re=10,490 where the suspending fluid was water. Plate tow direction is from left to right.

APPENDIX B: VELOCITY DATA DISTRIBUTION

This section has histograms displaying the distributions of U-component, V-component, and total (U_t) velocities. These distributions were used as a basis for calculating either the mean or median values to compare velocity data in Table 5.1. Also, the results of a two-sample t-test performed between data sets are shown in Table A.1.

From Table A.1 it is shown that at a 0.95 confidence interval, the data sets came from distributions with inequivalent sample means. This indicates that there was a significant difference in both U and V-velocities upon the addition of beads to each respective sample (Water, Glyc30, and Glyc60).

Table A.1: Two-sample T-test results performed between unfiltered data sets for each case using all runs performed. Results were obtained using MATLAB R 2011a[1] at a confidence interval of 0.95, with a null hypothesis of the two independent samples coming from distributions with equivalent means and variance. T-test results are shown for both the U-velocities (top table) and V-velocities (bottom table). Coloring indicates rejection of the null hypothesis (red) or not (green).

U	**Water**	**Glyc30**	**Glyc60**	**WaterB**	**Glyc30B**	**Glyc60B**
Water		0	0	0	0	0
Glyc30	0		0	0	0	0
Glyc60	0	0		0	0	0
WaterB	0	0	0		0	0
Glyc30B	0	0	0	0		0.7046
Glyc60B	0	0	0	0	0.7046	

Legend
H=1
H=0

V	**Water**	**Glyc30**	**Glyc60**	**WaterB**	**Glyc30B**	**Glyc60B**
Water		0	0	0	0	0
Glyc30	0		0	0	0	0
Glyc60	0	0		0	0	0
WaterB	0	0	0		0	0
Glyc30B	0	0	0	0		0
Glyc60B	0	0	0	0	0	

[1]Mathworks, Natick, MA, USA

Also, each Reynolds number case was independent apart from the increase from Re=4,581 to Re=10,490. This indicates that at a confidence interval of 0.95, as Reynolds number was increased a significant change occurred in the U and V-velocities for both cases *without* beads. Increasing Reynolds number from Re=1,143 to Re=4,581 in the cases *with* beads produced a significant change (confidence interval=0.95). The high p-value (0.7046) for the t-test between Re=4,581 and Re=10,490 indicates a high level of similarity between the two data sets. This supports the findings in Chapter 5, where no change with increased Reynolds number was distinguishable in the cases *with* beads.

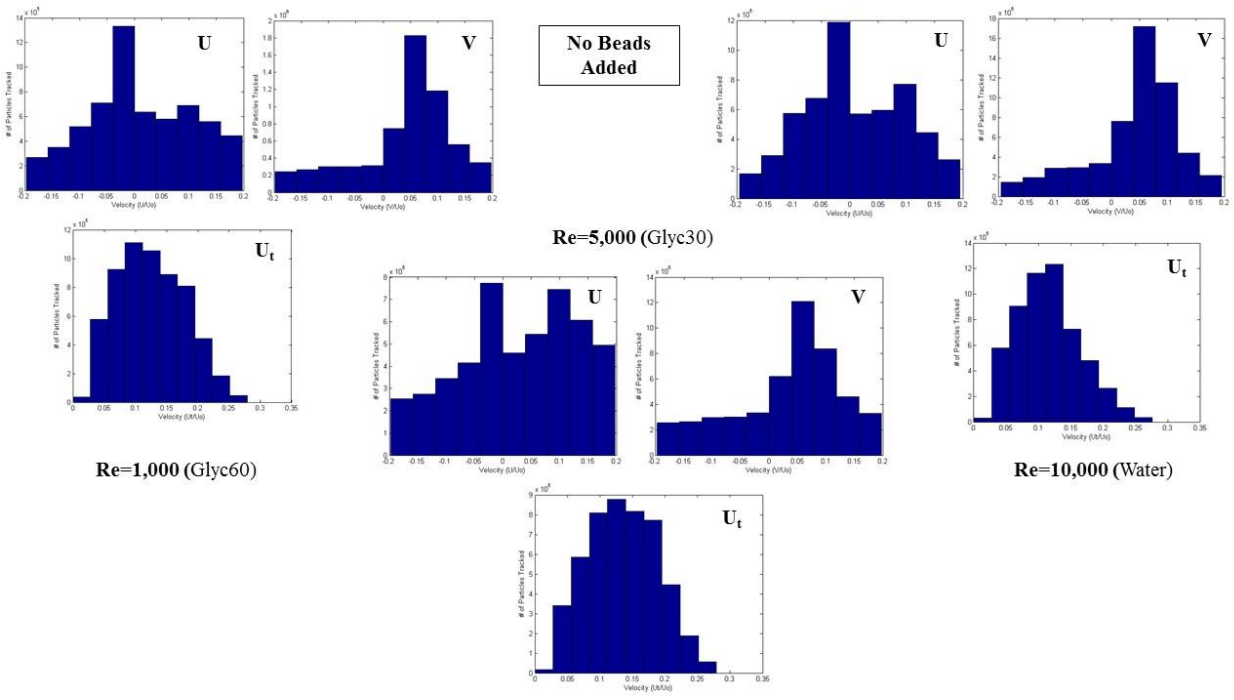

Figure A.5: Distribution of U and V-component velocities, and total velocity (U_t) for the cases *without* beads using all the data obtained from all 20 runs at each Reynolds number. Of importance is the U and V-component velocities tend to non-normal distributions, whereas U_t are closer in comparison to being normally distributed.

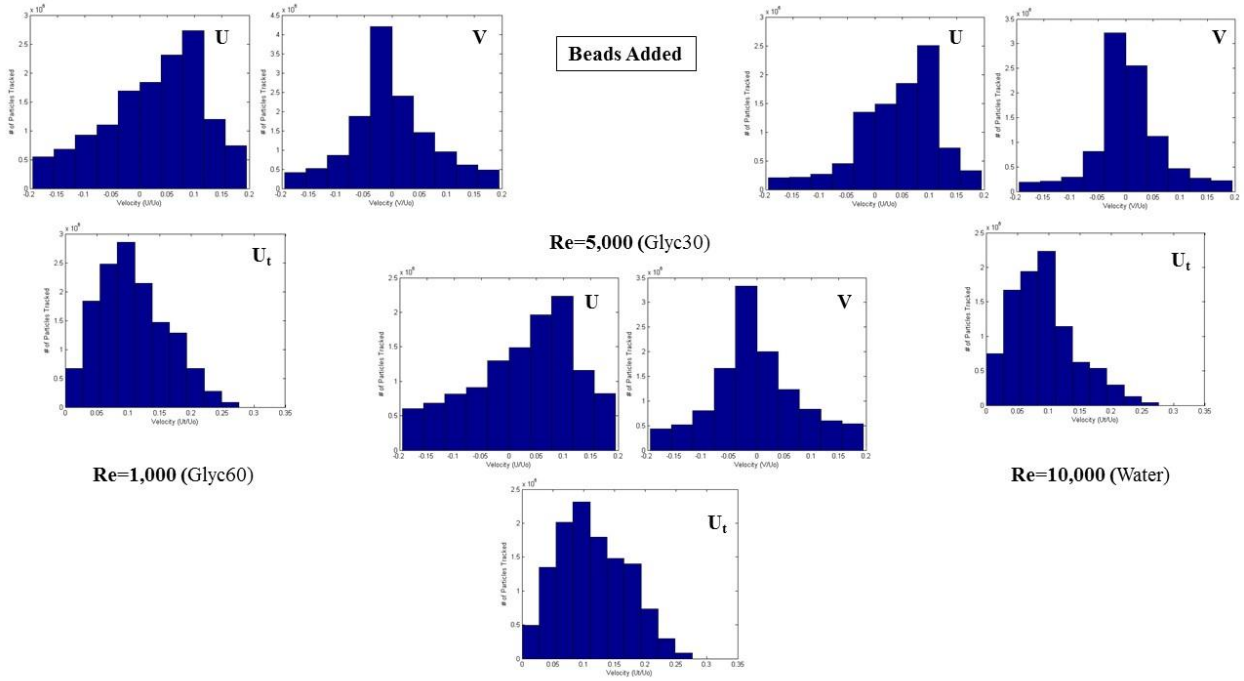

Figure A.6: Distribution of U and V-component velocities, and total velocity (U_t) for the cases *with* beads using all the data obtained from all 100 runs at each Reynolds number. Of importance is that V velocities appear to be generally normally distributed, whereas the U and V-component velocities are generally skewed.

APPENDIX C: EFFECTIVE VISCOSITY CALCULATIONS

Effective Viscosity Calculations

*Density and Viscosity @ 22 Celsius

Volumetric Concentrations

$\phi := 0.5$ $\phi_m := 0.68$

Suspending Fluid Viscosities

$\mu_{Glyc60} = 0.01 \frac{kg}{m \cdot s}$ $\mu_{Glyc30} = 0.002 \frac{kg}{m \cdot s}$

$\mu_{water} = \left(9.5 \cdot 10^{-4}\right) \frac{kg}{m \cdot s}$

Fluid Velocity

$U_f = 0.1 \frac{m}{s}$

Shear Generator Height

$H := 0.1\ m$

Krieger's Effective Velocity of a Suspension

$$\eta_r := \left(1 - \frac{\phi}{\phi_m}\right)^{-1.82} = 11.235$$

Effective Viscosities

$$\mu_{e60} := \mu_{Glyc60} \cdot \eta_r = 0.113 \frac{kg}{m \cdot s}$$

$$\mu_{e30} := \mu_{Glyc30} \cdot \eta_r = 0.026 \frac{kg}{m \cdot s}$$

$$\mu_{eW} := \mu_{water} \cdot \eta_r = 0.011 \frac{kg}{m \cdot s}$$

Reynold Number based on Effective Viscosity

$$Re_{KG60} := \frac{\rho_{Glyc60} \cdot U_f \cdot H}{\mu_{e60}} = 101.698$$

$$Re_{KG60} := \frac{\rho_{Glyc30} \cdot U_f \cdot H}{\mu_{e30}} = 407.764$$

$$Re_{KG60} := \frac{\rho_{water} \cdot U_f \cdot H}{\mu_{eW}} = 934.117$$